Damage Detection of Submerged Structures Using Linear and Nonlinear Guided Waves

Xianwen Hu

School of Civil, Environmental and Mining Engineering

The University of Adelaide

A thesis by publication submitted in fulfillment for the degree of

Doctor of Philosophy

March 2022

Abstract

Metallic plates are one of the major components of liquid containment structures and are widely used in petrochemical and civil engineering. In many cases, the metallic plates have one side exposed to liquid and are subjected to different types of loads with varying amplitudes. Corrosion damage and material degradations are the two major concerns. Damage detection of the submerged plate structures plays an important role in maintaining the structural integrity and safety of high-valued infrastructures (e.g. liquid storage tanks and pipes). Guided wave testing is one of the most promising damage detection approaches. Although guided wave based techniques have been extensively studied on different structures in gaseous environments, the design and implementation for the structures immersed in liquid have not been well investigated.

This research aims at enhancing the understanding of guided wave propagation and interaction with damage in submerged structures. The focus of this research is on metallic plates that have one side in contact with liquid and the other side exposed to air. The specific objectives of this thesis include the investigation on the propagation characteristics of guided waves in metallic plates with one side exposed to liquid, the development of numerical models to investigate the scattering characteristics of guided waves at corrosion pit damage, the analyses of the influence of the surrounding liquid medium on the linear and nonlinear guided waves features, and the evaluation of the sensitivity of linear and nonlinear guided waves features to different types of damage in the one-side immersed metallic plate.

The main body of the thesis consists of four journal articles (Chapters 2-5). Chapter 2 discusses the propagation characteristics and sensitivity to damage of linear guided waves in a metallic plate loaded with water on one side. The targeted damage is local thickness thinning (e.g. corrosion pits) with a size of around a few millimeters. Chapter 3 further investigates and compares the guided wavefields between a plate surrounded by air and the same plate with one side partly exposed to water. The influence of the surrounding liquid medium on the guided wave propagation is demonstrated experimentally and numerically. Chapters 4 and 5 study two different nonlinear guided wave features, which are second harmonic

generation and combination harmonic generation, respectively. The nonlinear guided wave features have better sensitivity to microstructural defects that precede the damage in the macroscale. The targeted damage in Chapters 4 and 5 is fatigue degradation in the early stage, where fatigue appears as multiple micro cracks and is distributed in the structural materials. The microstructural defects are too small to be detected by the linear guided wave feature. However, these small defects can distort the guided waves passing through the material, producing new wave components at frequencies other than the excitation frequency of the incident waves. This provides a way for the nonlinear guided wave technique to evaluate the early-stage damage in submerged structures.

Declaration

I, Xianwen Hu, hereby declare that this work contains no material which has been accepted for the award of any other degree or diploma in my name, in any university or other tertiary institution and, to the best of my knowledge and belief, contains no material previously published or written by another person, except where due reference has been made in the text. In addition, I certify that no part of this work will, in the future, be used in a submission in my name, for any other degree or diploma in any university or other tertiary institution without the prior approval of the University of Adelaide and where applicable, any partner institution responsible for the joint-award of this degree.

I acknowledge that the copyright of published works contained within this thesis resides with the copyright holder(s) of those works. I also give permission for the digital version of my thesis to be made available on the web, via the University's digital research repository, the Library Search, and also through web search engines, unless permission has been granted by the University to restrict access for a period of time.

I acknowledge the support I have received for my research through the provision of Adelaide Graduate Research Scholarship by The University of Adelaide.

Signature: _ Date: 07/03/2022

Acknowledgment

First of all, my sincere thanks go to my principal supervisor, Professor Ching-Tai (Alex) Ng, for his invaluable supervision and continuous support during my Ph.D. study. His rich knowledge and enthusiasm encouraged me to explore new research areas in the field of structural health monitoring. I would like to thank my co-supervisor, Professor Andrei Kotousov, for his treasured mentorships and contributions. I would also like to thank Professor Francis Rose for his technical advice.

I would like to extend my thanks to my fellow colleagues, Dr. Carman Yeung, Mr. Juan Allen, Dr. James Hughes, Mr. James Vidler, Dr. Munawwar Mohabuth, Ms. Tingyuan Yin, Mr. Ahmed Aseem, Mr. Jinhang Wu, Mr. Min Gao, Mr. Chang Jiang, Mr. Yuqiao Cao, Mr. Hankai Zhu, and Mr. Zijie Zeng. Thank them for spending cherished time with me in the laboratory and office. Their assistance and encouragement have been a strong source of inspiration to me. Also, thanks to my beloved technicians Mr. Brenton Howie, Mr. Jon Ayoub, Mr. Gary Bowman, and Mr. Ian Ogier. Their plentiful experience and treasured support played an important role in shaping my experimental methods. Without their technical assistance, this work would hardly be completed.

I would like to acknowledge the University of Adelaide for the financial support through the provision of Adelaide Graduate Research Scholarship. Due to the COVID-19 pandemic, my life and work have been severely affected since 2020. Thanks to the Adelaide Graduate Centre for extending the length of my candidature and scholarship, and providing me with financial support to complete this project. Thanks to the Faculty of Engineering, Computer, and Mathematical Science and the School of Civil, Environmental, and Mining Engineering for the additional financial subsidies to support me in presenting my research at international conferences.

Last but not least, I would like to thank my family. Special thanks to my father who told me that studying can change a person’s life. Special thanks to my mother who inspired me to be patient and grateful. Their love is beyond words. I am proud of myself for undertaking the Ph.D. program. It is a tough yet rewarding journey.

List of publications

This thesis by publications consists of a collection of published and accepted (for publication) journal articles in accordance with the requirements outlined in "the academic program rules" and "specifications for thesis" of The University of Adelaide. A complete list of the articles included in this thesis is presented here.

(1). **X. Hu**, C.T. Ng, A. Kotousov (2021), Scattering characteristics of quasi-Scholte waves at blind holes in metallic plates with one side exposed to water, *NDT & E International*, 117, 102379.

(2). **X. Hu**, C.T. Ng, A. Kotousov (2022), Numerical and experimental investigations on mode conversion of guided waves in partially immersed plates, *Measurement*, 190, 110750.

(3). **X. Hu**, C.T. Ng, A. Kotousov (2022), Early damage detection of metallic plates with one side exposed to water using the second harmonic generation of ultrasonic guided waves, *Thin-Walled Structures*, 176, 109284.

(4). **X. Hu**, C.T. Ng, A. Kotousov (2022), Structural health monitoring of partially immersed plates using nonlinear guided wave mixing, *Construction and Building Materials* (in-print).

The following book chapters and refereed conference papers are also derived from the research by the candidate within the candidature:

Book chapters:

(5). **X. Hu**, C.T. Ng, A. Kotousov (2021), Chapter 4: Damage detection of partially immersed plates using guided waves. In Recent Advances in Structural Health Monitoring Research in Australia: Nova Science Publishers Inc (In-print).

Conference papers:

(6). **X. Hu**, C.T. Ng, A. Kotousov (2021), Experimental investigations on second harmonics generated by leaky guided waves in immersed plates,

Proceedings of the 10th Australian Congress on Applied Mechanics (ACAM10), 1–3 December 2021, Adelaide, Australia

(7). **X. Hu**, C.T. Ng, A. Kotousov (2021), Nonlinear guided waves generated by leaky S_0 waves on submerged plates, Proceedings of the 10th International Conference on Structural Health Monitoring of Intelligent Infrastructure (SHMII10), 30 June–2 July 2021, Porto, Portugal

(8). **X. Hu**, C.T. Ng, A. Kotousov (2019), Ultrasonic guided wave-field modeling in a one-side water-immersed steel plate, In: *Vol. 101. Lecture Notes in Civil Engineering* (pp. 1131-1140)

Table of content

Chapter 1. Research overview

1.1 Background

Metallic plates are the main components in liquid containment structures, such as liquid storage tanks and pipelines. They are widely used in petrochemical and civil engineering. When the devices are in service as shown in Figure 1.1, the metallic plates have one side exposed to liquid and are subjected to different types of loads with varying amplitudes. Over time, the structural materials are degrading, and corrosion can grow extensively in localized regions on the submerged sides of these structures. Failure to control the structural defects leads to leakage, catastrophic structural failures, and huge costs of downtime, fatalities, and environmental damage. For instance, it is estimated that the global cost of corrosion contributes to 3.4% of the global gross domestic product (GDP), which is around US$ 2.5 trillion per year [1]. Up to 30% of these costs can be saved through proper damage control practices including periodic inspections and repair.

Figure 1.1 Example of tanks and pipes filled with liquid

In the past few decades, many non-destructive testing (NDT) methods have been proposed to minimize the impacts of in-service failure of high-valued infrastructures. These NDT techniques include visual inspection by divers and robots [2], hydro test [3], ultrasonic testing [4], acoustic emission [5, 6], magnetic flux leakage test [7], and eddy current test [8]. These NDT approaches are not economic and inconvenient because they require periodic shutdown of the facilities to implement inspection. Recent research has put forward the concept of structural health monitoring (SHM), which is to permanently install lightweight and durable sensors on the structure and continuously evaluate the structural integrity. SHM has the potential to reduce costs by scheduling the maintenance only as needed [9]. Both the NDT and SHM communities have conducted extensive research to detect defects at an earlier stage and track the damage evolution. Earlier detection of damage allows more time to plan actions that would ultimately enhance safety.

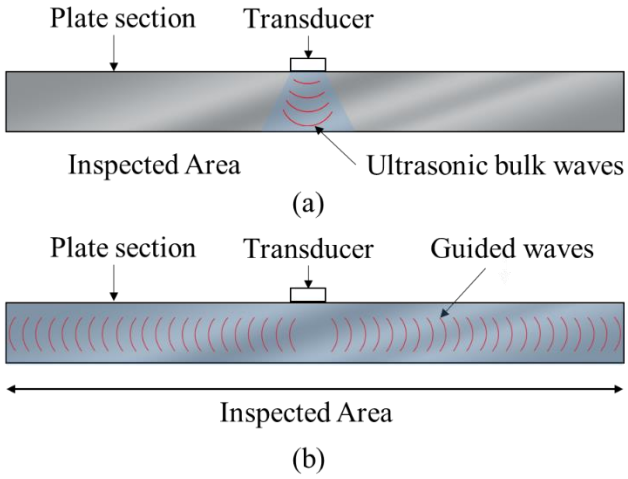

Figure 1.2 Comparison of inspection area between (a) conventional ultrasonic testing using bulk waves and (b) guided wave testing

Guided wave testing is one of the most promising SHM approaches, which can achieve much larger inspection ranges than the conventional NDT approaches, by using a small number of sensors permanently attached to the structures. Guided waves are defined as elastic waves propagating along a boundary or between parallel boundaries of a structure. Figure 1.2 compares the inspections of a plate

structure using conventional ultrasonic testing and guided wave testing, respectively. Conventional ultrasonic testing inspects the structure using bulk waves (e.g. longitudinal wave and shear wave). The inspection area is the local region below the transducer. The transducer must be moved along the surface to collect data. In contrast, guided waves cover the total thickness of the structures over a fairly long distance. The inspected area using guided waves is much larger, compared to the conventional ultrasonic testing.

Previous studies have demonstrated that guided waves have high sensitivity to various structural defects and can inspect inaccessible locations [10]. The majority of the work on the applications of guided waves has been conducted on the structures in gaseous environments. In the literature, there were limited studies that employed guided waves to detect damage in structures immersed in liquid. The interaction between guided waves and defects in submerged structures has not been fully understood. To provide support for the further development of the structural health monitoring techniques for submerged structures, this thesis investigates the feasibility of using both the linear and nonlinear guided waves to detect and characterize damage in plate structures with one side exposed to liquid. The following section provides a brief review of research progress in the field of damage detection using linear and nonlinear guided waves.

1.2 Literature review

1.2.1. Linear guided wave testing

Linear guided waves are sensitive to defects with a size comparable to the wavelength of the selected guided wave modes. Generally, they are around a few millimeters. Typical examples of these defects include small corrosion pits, dents, cuts, and notches. The interaction between guided waves and these defects can generate scattered waves at the same frequency components as the incident waves. The scattered waves can alter the transmitted guided wave signals, such as wave amplitude changes, arrival time delays, phase shifts, and mode conversions.

There are various types of guided wave modes depending on the structural boundaries. For example, Rayleigh waves propagate on the surface of a semi-

infinite solid [11, 12]. Edge waves travel along the structural edges [13, 14]. Lamb waves refer to guided waves in thin-walled structures such as plates and pipes [15, 16]. In this study, we focus on the thin-walled plate structure with one side immersed in liquid. Guided waves in the immersed plate structures have leaky Lamb modes and the quasi-Scholte mode. Leaky Lamb waves are composed of multiple leaky symmetric and antisymmetric wave modes. They also are called leaky guided waves because the wave energy can transmit into the surrounding liquid medium through the solid-liquid interface.

The application of leaky guided waves for submerged thin-walled structures is limited to several guided wave modes at their corresponding low attenuation frequency region because most of the leaky guided waves decay quickly due to high attenuation. The fundamental leaky symmetric Lamb wave mode (leaky S_0) is one of the most popular wave modes and has been employed to estimate circular holes, notches, and corrosion in metal plates immersed in water [17-21]. When the excitation frequency is below the cut-off frequency of the higher-order wave modes, leaky S_0 wave has very low attenuation and is well separated from the other wave modes due to the fastest propagation speed. The structural defects can be evaluated by leaky S_0 wave with relatively simple signal processing techniques. However, it is not sensitive to small and shallow defects on the structural surfaces. To overcome this limitation, researchers also investigated the first-order leaky symmetric Lamb wave mode (leaky S_1) [20, 22] and the first-order leaky anti-symmetric Lamb wave mode (leaky A_1) [19] to evaluate different defects in immersed plate structures. Generally, the higher-order guided wave modes (leaky S_1 and leaky A_1) have high sensitivity to the shallow defects at the plate surface. However, the experimentally measured signals are much more complicated due to the presence of multiple wave modes.

The quasi-Scholte wave was also studied to detect notch damage in immersed metal plates [23]. The quasi-Scholte wave can be generated at low excitation frequencies and has very low attenuation. It should be noted that the quasi-Scholte wave has a much lower phase velocity compared to leaky S_0 wave at a given frequency. A lower phase velocity indicates a shorter wavelength and higher sensitivity to small and shallow defects at the structural surface [24]. This is due to

the fact that the size of the defects should be larger than half the wave wavelength of the passing guided waves to ensure the scattered waves by the defects can be measurable [25].

1.2.2. Nonlinear guided wave testing

Generally speaking, it is better to identify defects sooner than later. Earlier detection of damage allows more time to plan maintenance action and substantially improves safety. In the early damage stage, all material has the inherent material nonlinearity that is attributed to microstructural defects such as micro cracks, persistent slip bands, and dislocation [9, 26, 27]. As the loads increase, these microstructural defects accumulate and evolve into macro cracks. The evolution from microstructural defects to macro cracks takes up a major part of the total service life [9]. After that, the macro cracks grow quickly to critical points, leading to catastrophic failure.

The microstructural defects are too small to be detected by linear guided wave testing as mentioned above. However, they can distort the passing guided waves and generate new wave components at frequencies other than the incident waves. The new wave components are called the nonlinear guided wave features and have been shown to change significantly during the early damage stage in air-coupled structures [11, 28-36]. This phenomenon enables researchers to identify smaller defects and track material degradation in the early stage. However, nonlinear guided waves have not yet been well studied for damage detection for structures immersed in liquid. The influence of the liquid coupling on the generation of the nonlinear guided waves is unknown.

1.3 Research aims and objectives

This research aims at enhancing the understanding of guided wave propagation and interaction with damage in submerged structures. The focus of the current research is on metallic plates that have one side in contact with liquid and the other side exposed to air. The intended application includes damage detection for liquid

containment structures such as water towers, storage tanks, and ship hulls. The project comprises the following objectives:

Objective 1: To investigate the propagation characteristics of leaky guided waves in a metallic plate with one side exposed to liquid

An analytical analysis is conducted to derive the dispersion curves and mode shapes of the leaky guided waves in a metal plate with one side exposed to liquid. According to the theoretical results, the low attenuation frequency range of the fundamental leaky guided wave modes (leaky S_0, leaky A_0, and quasi-Scholte waves) are identified. After that, the propagation characteristics of the selected wave modes are investigated through experimental measurements. Finally, the influence of the surrounding liquid is demonstrated by comparing the signals experimentally measured from a metal plate with and without liquid.

Objective 2: To develop a 3D FE model to investigate the scattering characteristics of leaky guided waves at corrosion pit damage

A 3D FE model is developed to simulate the interaction between leaky guided waves and corrosion pits. The numerical simulation can provide a visualization of the guided wave fields and help interpret the experimental data. The scattering characteristics of leaky guided waves are analyzed by means of scattering directive pattern (SDP), which provides the scattering amplitudes in all directions around the damage.

Objective 3: To analyze the effect of the surrounding liquid medium on the linear and nonlinear guided wave features

The influence of the surrounding liquid on the linear and nonlinear guided wave features is demonstrated by comparing the signals experimentally measured from a metal plate with and without liquid. Nonlinear interactions between guided waves and the microstructures in materials are investigated. The focus has been on the generation of second harmonics and combination harmonics.

Objective 4: To evaluate the sensitivity of linear and nonlinear leaky guided waves to various damage in the metallic plate with one side exposed to liquid

Fatigue is one of the major concerns for submerged structures that are subjected to cyclic loading with varying amplitudes. In the fatigue stage, the microstructural defects in the material continue to grow and accumulate, which can be evaluated by the nonlinear guided wave features. Corrosion damage is another important issue for metallic structures operating in humid environments. Corrosion pits with a few millimeters can be evaluated by linear guided wave features. Numerical and experimental studies are conducted to evaluate the sensitivity of both linear and nonlinear guided waves to different types of damage in the immersed plate.

1.4 Structure of the thesis

This thesis consists of four journal articles in regard to applying guided waves for damage detection of submerged structures. Chapter 1 provides a brief background on the research and introduces the significance of safety inspection for submerged structures. This is followed by an overview of guided wave techniques for damage detection, which can be further categorized into linear guided wave testing and nonlinear guided wave testing. Then, the aims and objectives of the research are presented and a brief outline of the thesis is formulated.

Chapter 2 (Paper 1) discusses the propagation characteristics and sensitivity to damage of linear guided wave features on a metallic plate loaded with water on one side. The targeted damage is local thickness thining (e.g. corrosion pits) with a size of around a few millimeters, which is the major concern for metallic structures. To simulate corrosion pits, blind holes are mechanically drilled on a steel plate with one side exposed to water. The interaction of guided waves with the blind holes is investigated.

Chapter 3 (Paper 2) further investigates the behaviors of guided waves in a metallic plate with one side partly exposed to water. The influence of the surrounding liquid medium on the guided wave propagation is demonstrated

experimentally and numerically by comparing the guided wavefields between the plate surrounded by air and the plate with one side partly exposed to water. The findings of this chapter indicate that the defects (e.g. corrosion pits) on partially immersed plates (e.g. tanks or pipes partially filled with liquids) can be evaluated by sending guided waves on the dry section of the plates and measuring the guided wave signals on the immersed section.

Chapter 4 (Paper 3) explores the nonlinear guided wave testing using tone burst signals with a single central excitation frequency. In the literature, the linear guided wave testing can only identify defects with a size comparable to the wavelength of the passing guided waves, which are around a few millimeters. The nonlinear guided wave features have better sensitivity to microstructural defects that precede the damage in the macroscale and allow earlier damage detection. This chapter investigates the feasibility of the second harmonic generation by guided waves in metallic plates with one side exposed to water. Three criteria are proposed for the selection of guided wave modes and excitation frequencies, which ensures the measurable and cumulative generation of the second harmonics due to the material nonlinearity. Both experiments and numerical simulations are conducted and the results demonstrated that the second harmonics by leaky S_0 waves are sensitive to the early-stage damage in plates with one side immersed in water.

Chapter 5 (Paper 4) numerically and experimentally investigates the nonlinear guided waves mixing two different frequencies in an aluminum plate loaded with water on one side. Leaky S_0 waves are excited at two different frequencies on the wall of a metal tank filled with water. The nonlinear interaction between leaky S_0 waves with two different frequencies can produce cumulative combination harmonics at the sum frequency. Compared to the second harmonics studied in Paper 3, the combination harmonics are less affected by the higher harmonics produced by the instrumentations. In addition, mixing guided waves with different frequencies provides more flexibility for the selection of guided wave modes and excitation frequencies. In addition, the combination harmonics show a better sensitivity to the early stage of fatigue damage than the second harmonics.

Chapter 6 summarizes the contributions and significance of the research carried out in this thesis and provides recommendations for future studies.

1.5 References

[1] G. Koch, Cost of corrosion, Trends in oil and gas corrosion research and technologies, (2017) 3-30.

[2] L. Christensen, N. Fischer, S. Kroffke, J. Lemburg, R. Ahlers, Cost-effective autonomous robots for ballast water tank inspection, Journal of ship production and design, 27 (2011) 127.

[3] M. Hassanzadeh, K. Rahmani, Hydrostatic test of storage tanks using seawater and corrosion considerations, Engineering Failure Analysis, 122 (2021) 105267.

[4] S.T. Jayanto, M. Chendra, A.T. Wijayanta, Estimating corrosion rate and remaining life of a pressure vessel of H2S absorber, AIP Conference Proceedings, 2097 (2019) 030007.

[5] B.A. Zárate, A. Pollock, S. Momeni, O. Ley, Structural health monitoring of liquid-filled tanks: a Bayesian approach for location of acoustic emission sources, Smart Materials and Structures, 24 (2014) 015017.

[6] C. Mukhopadhyay, T. Haneef, T. Jayakumar, G. Sharma, B. Rao, Structural integrity assessment of H2S storage tanks using acoustic emission and ultrasonic techniques, International Journal of Structural Integrity, (2015).

[7] L. Peng, S. Huang, S. Wang, W. Zhao, Three-dimensional magnetic flux leakage signal analysis and imaging method for tank floor defect, The Journal of Engineering, 2018 (2018) 1865-1870.

[8] M. Grosso, C.J. Pacheco, M.P. Arenas, A.H.M. Lima, I.C.P. Margarit-Mattos, S.D. Soares, G.R. Pereira, Eddy current and inspection of coatings for storage tanks, Journal of Materials Research and Technology, 7 (2018) 356-360.

[9] V.K. Chillara, C.J. Lissenden, Review of nonlinear ultrasonic guided wave nondestructive evaluation: theory, numerics, and experiments, Optical Engineering, 55 (2015) 011002.

[10] J.L. Rose, Ultrasonic guided waves in solid media, Cambridge university press, 2014.

[11] S.V. Walker, J.-Y. Kim, J. Qu, L.J. Jacobs, Fatigue damage evaluation in A36 steel using nonlinear Rayleigh surface waves, NDT & E International, 48 (2012) 10-15.

[12] C.-T. Ng, H. Mohseni, H.-F. Lam, Debonding detection in CFRP-retrofitted reinforced concrete structures using nonlinear Rayleigh wave, Mechanical Systems and Signal Processing, 125 (2019) 245-256.

[13] M.V. Wilde, M.V. Golub, A.A. Eremin, Experimental and theoretical investigation of transient edge waves excited by a piezoelectric transducer bonded to the edge of a thick elastic plate, Journal of Sound and Vibration, 441 (2019) 26-49.

[14] J.M. Hughes, M. Mohabuth, A. Kotousov, C.-T. Ng, The fundamental ultrasonic edge wave mode: Propagation characteristics and potential for distant damage detection, Ultrasonics, 114 (2021) 106369.

[15] J. Hua, X. Cao, Y. Yi, J. Lin, Time-frequency damage index of Broadband Lamb wave for corrosion inspection, Journal of Sound and Vibration, 464 (2020) 114985.

[16] R. Soleimanpour, C.-T. Ng, Scattering analysis of nonlinear Lamb waves at delaminations in composite laminates, Journal of Vibration and Control, (2021) 1077546321990145.

[17] M. Santos, J. Perdigao, Leaky Lamb waves for the detection and sizing of defects in bonded aluminium lap joints, NDT & E International, 38 (2005) 561-568.

[18] E. Pistone, K. Li, P. Rizzo, Noncontact monitoring of immersed plates by means of laser-induced ultrasounds, Structural Health Monitoring, 12 (2013) 549-565.

[19] S. Sharma, A. Mukherjee, Damage detection in submerged plates using ultrasonic guided waves, Sadhana, 39 (2014) 1009-1034.

[20] S. Sharma, A. Mukherjee, Ultrasonic guided waves for monitoring corrosion in submerged plates, Structural Control and Health Monitoring, 22 (2015) 19-35.

[21] Q. Xie, C. Ni, Z. Shen, Defects detection and localization in underwater plates using laser laterally generated pure non-dispersive S0 mode, Applied Sciences, 9 (2019) 459.

[22] A.E. Takiy, C. Kitano, R.T. Higuti, S.C.G. Granja, V.T. Prado, L. Elvira, O. Martínez-Graullera, Ultrasound imaging of immersed plates using high-order Lamb modes at their low attenuation frequency bands, Mechanical Systems and Signal Processing, 96 (2017) 321-332.

[23] T. Hayashi, R. Fujishima, Defect detection using quasi-Scholte wave for plate loaded with water on single surface, Materials Transactions, (2016) M2016204.

[24] X. Hu, C.-T. Ng, A. Kotousov, Damage detection of partially immersed plates using guided waves, Recent Advances in Structural Health Monitoring Research in Australia, Nova Science Publishers Inc., 2021.

[25] X. Hu, C.-T. Ng, A. Kotousov, Scattering characteristics of quasi-Scholte waves at blind holes in metallic plates with one side exposed to water, NDT & E International, 117 (2021) 102379.

[26] K.-Y. Jhang, Nonlinear ultrasonic techniques for nondestructive assessment of micro damage in material: A review, International Journal of Precision Engineering and Manufacturing, 10 (2009) 123-135.

[27] M. Mitra, S. Gopalakrishnan, Guided wave based structural health monitoring: A review, Smart Materials and Structures, 25 (2016) 053001.

[28] K.H. Matlack, J.-Y. Kim, L.J. Jacobs, J. Qu, Experimental characterization of efficient second harmonic generation of Lamb wave modes in a nonlinear elastic isotropic plate, Journal of Applied Physics, 109 (2011) 014905.

[29] W. Li, Y. Cho, J.D. Achenbach, Detection of thermal fatigue in composites by second harmonic Lamb waves, Smart Materials and Structures, 21 (2012) 085019.

[30] C.J. Lissenden, Y. Liu, G.W. Choi, X. Yao, Effect of localized microstructure evolution on higher harmonic generation of guided waves, Journal of Nondestructive Evaluation, 33 (2014) 178-186.

[31] F. Ciampa, S. Pickering, G. Scarselli, M. Meo, Nonlinear damage detection in composite structures using bispectral analysis, SPIE, 2014.

[32] R. Soleimanpour, C.-T. Ng, C.H. Wang, Higher harmonic generation of guided waves at delaminations in laminated composite beams, Structural Health Monitoring, 16 (2017) 400-417.

[33] J. Jiao, X. Meng, C. He, B. Wu, Nonlinear Lamb wave-mixing technique for micro-crack detection in plates, NDT & E International, 85 (2017) 63-71.

[34] W. Zhu, Y. Xiang, C.-j. Liu, M. Deng, C. Ma, F.-z. Xuan, Fatigue damage evaluation using nonlinear Lamb Waves with Quasi phase-velocity matching at low frequency, Materials, 11 (2018) 1920.

[35] S. Shan, M. Hasanian, H. Cho, C.J. Lissenden, L. Cheng, New nonlinear ultrasonic method for material characterization: Codirectional shear horizontal guided wave mixing in plate, Ultrasonics, 96 (2019) 64-74.

[36] K.-Y. Jhang, C.J. Lissenden, I. Solodov, Y. Ohara, V. Gusev, Measurement of nonlinear ultrasonic characteristics, Springer, 2020.

Chapter 2. Scattering characteristics of quasi-Scholte waves at blind holes in metallic plates with one side exposed to water

Abstract

Corrosion is one of the major issues in metallic structures, especially those operating in humid environments and submerged in water. It is important to detect corrosion at its early stage to prevent further deterioration and catastrophic failures of the structures. Guided wave-based damage detection technique is one of the promising techniques for detecting and characterizing damage in structures. In water-immersed plate structures, most of the guided wave modes have strong attenuation due to energy leakage into the surrounding liquid. However, there is an interface wave mode known as quasi-Scholte waves, which can propagate with low attenuation. Therefore, this mode is promising for structural health monitoring (SHM) applications. This paper presents an analysis of the capability of quasi-Scholte waves in detecting internal corrosion-like defects in water-immersed structures. A three-dimensional (3D) finite element (FE) model is developed to simulate quasi-Scholte wave propagation and wave scattering phenomena on a steel plate with one side exposed to water. The accuracy of the model is validated through experimental measurements. There is good agreement between the FE simulations and experimental measurements. The experimentally verified 3D FE model is then employed in a series of parametric studies to analyze the scattering characteristics of quasi-Scholte waves at circular blind holes with different diameters and depths, which are the simplest representation of progressive corrosion. The findings of this study can enhance the understanding of quasi-Scholte waves scattering at corrosion damage of structures submerged in water and help improve the performance of in-situ damage detection techniques.

Keywords: Quasi-Scholte waves; guided waves; scattering; submerged structure; corrosion; metallic plate

Statement of Authorship

Title of Paper	Scattering characteristics of quasi-Scholte waves at blind holes in metallic plates with one side exposed to water
Publication Status	☑ Published ☐ Accepted for Publication ☐ Submitted for Publication ☐ Unpublished and Unsubmitted w ork w ritten in manuscript style
Publication Details	X. Hu, C.T. Ng, A. Kotousov (2021), Scattering characteristics of quasi-Scholte waves at blind holes in metallic plates with one side exposed to water, *NDT & E International*, 117, 102379.

Principal Author

Name of Principal Author (Candidate)	Xianwen Hu		
Contribution to the Paper	Conceptualization, Developing and validating numerical models, Conducting experimental measurements, Signal processing and data analysis, Writing the original draft and editing.		
Overall percentage (%)	80%		
Certification:	This paper reports on original research I conducted during the period of my Higher Degree by Research candidature and is not subject to any obligations or contractual agreements with a third party that would constrain its inclusion in this thesis. I am the primary author of this paper.		
Signature		Date	07/03/2022

Co-Author Contributions

By signing the Statement of Authorship, each author certifies that:

i. the candidate's stated contribution to the publication is accurate (as detailed above);

ii. permission is granted for the candidate in include the publication in the thesis; and

iii. the sum of all co-author contributions is equal to 100% less the candidate's stated contribution.

Name of Co-Author	Ching-Tai Ng		
Contribution to the Paper	Supervision, writing – review & editing.		
Signature		Date	9/3/2022

Name of Co-Author	Andrei Kotousov		
Contribution to the Paper	Supervision, writing – review & editing.		
Signature		Date	07/03/2022

Please cut and paste additional co-author panels here as required.

2.2. Introduction

Structures that have one side exposed to water are commonly encountered, such as water tanks, pipelines, and ship hulls. These structures often incorporate plate-like components, which are prone to corrosion as a result of electrochemical reactions in the presence of water. Corrosion can occur in a localized region and deteriorate the strength of the structures. It is important to detect and control corrosion so that catastrophic failures and leakage can be avoided.

Among various structural health monitoring (SHM) techniques [1-3], guided wave-based techniques have attracted increasing interest due to the ability to inspect large areas compared to the conventional non-destructive evaluation (NDE) techniques, high sensitivity to different types and small damage, and the ability to inspect inaccessible locations. A review of guided wave-based SHM techniques can be found in [4]. However, the majority of the studies on guided waves have focused on the structures with traction free boundary conditions [5-8]. Meanwhile, there are limited studies on using guided waves for safety inspections on structures submerged in water, especially the quasi-Scholte waves.

2.2.1. Damage detection of submerged structures using guided waves

Energy of guided waves in structures immersed in water can leak into the surrounding medium so that most of the guided wave modes have high attenuation characteristics, which significantly reduces the inspection area. As a result, the practical applications are limited to specific guided wave modes and the excitation frequencies need to be at their corresponding low attenuation frequency bands [9]. Several studies demonstrated the feasibility of using guided waves for damage inspection in submerged structures. Na and Kundu [10] investigated the capability of the flexural cylindrical guided wave modes in detecting defects in underwater pipes. They found that the amplitudes of the transmitted signals would be decreased after they passed through various types of damage in pipes. This phenomenon could be used to evaluate the extent and distinguish the type of damage. Chen et al. [11] employed the fundamental antisymmetric leaky lamb wave mode (leaky A_0 waves) to evaluate corrosion damage in a submerged metallic plate. The amplitudes and

the speed of leaky A_0 waves were found to be significantly affected by the surrounding fluid medium. Pistone et al. [12] used a pulsed laser to generate guided waves in a water-immersed aluminum plate and collected the wave signal by an array of immersed transducers. They concluded that the fundamental symmetric leaky lamb wave mode (leaky S_0 waves), which had the fastest wave speed and the least decay, could be used to detect cracks and holes in the plate. Sharma and Mukherjee [13] used a pair of immersed ultrasonic transducers to generate and measure guided waves in a steel plate, both sides of which were fully immersed in water. Leaky S_0 waves, the first order symmetric leaky lamb wave mode (leaky S_1 waves), and the first order anti-symmetric leaky lamb wave mode (leaky A_1 waves) were excited at their corresponding low attenuation frequency bands. Each of these wave modes demonstrated a different sensitivity to notch-like defects and the decrease in amplitudes of the transmitted signal could be related to the severity of the damage. Takiy et al. [9] implemented experiment studies to verify the existence of guided wave modes at their theoretically predicted low attenuation frequency bands. It was confirmed that the higher order guided wave modes at their corresponding low attenuation frequency bands were also suitable to be used for damage detection in submerged structures.

2.2.2. Quasi-Scholte waves in immersed structures

In addition to the symmetric and anti-symmetric guided wave modes, there is an interface wave mode known as quasi-Scholte waves existing at the water-plate interface. This interface wave mode has low attenuation but it is rarely used for evaluating damage in structures since it has been reported that a large proportion of energy is propagating into the fluid at high frequencies [14]. However, it is found that most of the wave energy of the quasi-Scholte mode at low excitation frequencies is conserved in the structures during the propagation. Tian and Yu [15, 16] experimentally investigated guided wave propagation on a steel plate loaded with water on a single side. They used a scanning laser Doppler vibrometer to measure the wave signals along a line and plotted the data in the frequency-wavenumber spectrum. It was demonstrated that leaky A_0 waves were indiscernible at low frequencies due to high attenuation while quasi-Scholte waves appeared

clearly. Recently, Hayashi and Fujishima [17] studied the feasibility of using quasi-Scholte waves for damage detection in a thin aluminum plate that had one side immersed in water. The scattered waves due to a through-thickness notch could be observed at the low-frequency range. It should be noted that this study only measured the reflected signals. The scattering characteristics were not investigated.

The practical application of the guided waves relies on a distributed transducer network, by which the guided wave signal is sequentially emitted by one of the transducers, and the rest of the transducers are used to measure the impinging waves. The majority of guided wave-based damage detection techniques employ the waves scattered at the damage and received by the transducers at different directions to detect and identify the damage [5, 18-20]. Therefore, understanding the scattering characteristics at different directions plays an important role in the development of the guided wave-based damage detection techniques. In the literature, different studies investigated the scattering characteristics of guided waves at different types of defects. However, the majority of the studies focused on traction free conditions, and the scattering characteristics of guided waves in plates loaded with water have not been well investigated. In particular, there are very limited studies investigating the scattering characteristics of the interface wave mode, quasi-Scholte waves, in plates loaded with water.

This paper presents comprehensive numerical and experimental analyses of the scattering characteristics of quasi-Scholte waves at corrosion-like defects in structures exposed to water, such as water tanks and pipelines. The numerical method using a three-dimensional (3D) finite element (FE) model is employed to investigate the guided wave propagation and scattering phenomena on a one-side water-immersed steel plate with a circular blind hole that represents a corrosion spot or wall thinning, which is exposed to water. The scattering characteristics are investigated in terms of scattering directivity patterns (SDPs), which display the energy distribution of the scattered waves around the damage. The findings of this study provide a guide on the selection of appropriated excitation frequencies and sensor locations to evaluate corrosion damage, which can advance the guided wave-based damage detection techniques for submerged structures.

This paper first presents the theoretical prediction of guided waves traveling along a steel plate that has one side submerged in water in Section 2.3. Sections 2.4 and 2.5 describe the 3D FE simulation and experimental verification, respectively. The accuracy of the simulation results is validated through experimental measurements. Then, a series of numerical studies are carried out using the experimentally verified 3D FE model to investigate the characteristics of the scattered quasi-Scholte waves at blind holes with different dimensions in Section 2.6. Finally, discussions and conclusions are provided and drawn in Sections 2.7 and 2.8, respectively.

2.3. Guided waves in one-side water-immersed plates

Guided waves in plate-like structures are comprised of multiple symmetric and anti-symmetric wave modes, which are represented by symbols S_i and A_i, respectively, with the subscript (i = 0, 1,…) representing the order of the wave modes. The majority of the studies consider the plates that are placed open to the air. The boundary conditions for the top and bottom sides of the plates are traction-free as shown in Figure 2.1(a). The characteristic equation of the guided waves can be described as [21]

$$\frac{\tan(qh)}{\tan(ph)} = -\frac{4k^2qp}{\left(k^2-q^2\right)^2} \tag{2.1}$$

for symmetric modes S_i, and

$$\frac{\tan(qh)}{\tan(ph)} = -\frac{\left(k^2-q^2\right)^2}{4k^2qp} \tag{2.2}$$

for anti-symmetric modes A_i, where $h = d/2$; $q^2 = w^2/c_{\mathrm{T}}^2 - k^2$; $p^2 = w^2/c_L^2 - k^2$; d, w, and k represent the plate thickness, circular frequency, and wavenumber, respectively; c_{L} and c_{T} are the longitudinal wave speed and the transverse wave speed of the plate, respectively. It can be seen from Eqs (2.1) and (2.2) that the characteristics of guided wave modes depend on the product of the plate thickness and the frequency. The solutions can be presented as guided wave dispersion curves

that describe the relationship between the frequency-thickness product and the characteristics of the guided wave modes.

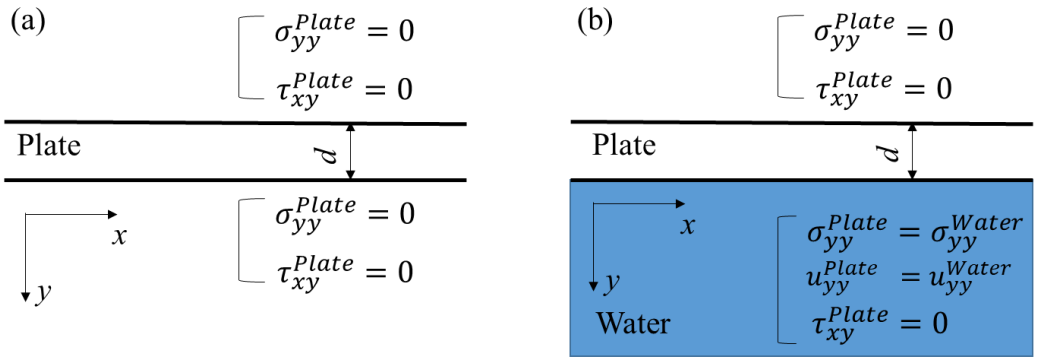

Figure 2.1. Boundary conditions (a) free plate; and (b) one-side water-immersed plate

When one side of the plate is immersed in water, as shown in Figure 2.1(b), the interface between the water and the plate is no longer traction free and the guided wave propagation changes [22]. The wave energy can leak into the water through out-of-plane motions of the particles at the water-plate interface. However, the displacements of the water and the plate are discontinuous in the shear direction because water cannot sustain shear loads [23, 24]. The governing equations of guided waves in the one-side water-immersed plate can be expressed as [25, 26]

$$\det\left(G\left(w,k,c_w,c_{\mathrm{T}},c_{\mathrm{L}},d,\rho_w,\rho\right)\right)=0 \tag{2.3}$$

where c_w and ρ_w represent the bulk wave speed and density of water, respectively. G represents the characteristic matrix for the coupled fluid and solid waveguide. By solving Eq (2.3), one can obtain the dispersion curves of guided waves for the one-side water-immersed steel plate.

The calculation can be done by the commercial software DISPERSE, which employs the global matrix method to calculate dispersion curves in a multi-layer waveguide [27]. In this method, the bulk wave characteristics of each layer are first determined from the corresponding material properties. Then, the stresses and

displacements in each layer can be expressed in terms of the partial waves, which are assembled into one large global matrix with the boundary conditions. The global matrix can be solved for its modal response to find valid combinations of a certain frequency, wavenumber, and attenuation. The process repeats until all dispersion curves are traced.

Figure 2.2 shows the phase velocity and attenuation dispersion curves of a steel plate that has its bottom surface immersed in water. There are three wave modes within the frequency-thickness band up to 1 MHz-mm: quasi-Scholte waves, leaky A_0 waves, and leaky S_0 waves. Unlike leaky A_0 waves and leaky S_0 waves, quasi-Scholte waves are one of the interface wave modes that have the most energy concentrated at the water-plate interface instead of radiating into the liquid [28]. In general, the phase velocity of quasi-Scholte waves, at a given excitation frequency, is much smaller than leaky S_0 waves and leaky A_0 waves as shown in Figure 2.2(a). Smaller phase velocity means a shorter wavelength, which means higher sensitivity to small defects [11]. In addition, the attenuation of quasi-Scholte waves is almost zero for the entire frequency-thickness range (Figure 2.2(b)). Therefore, quasi-Scholte waves theoretically have the potential for long-range inspection and are expected to have a high sensitivity to damage.

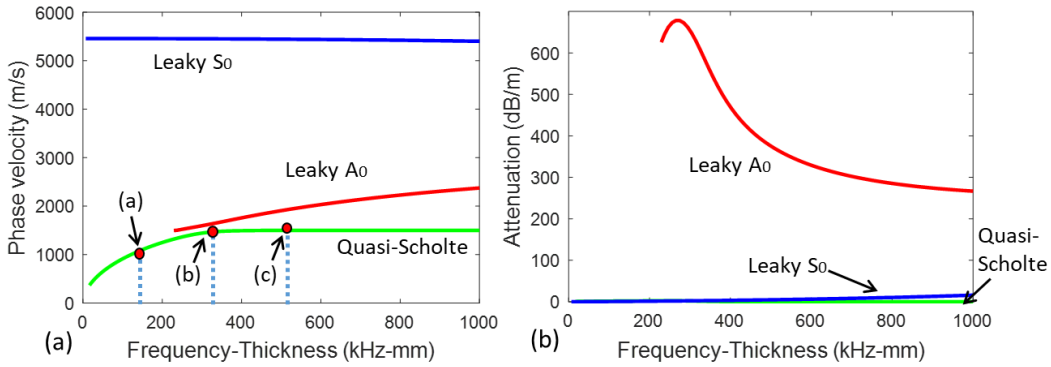

Figure 2.2. (a) Phase velocity and (b) attenuation dispersion curves of 1 mm thick steel plate with one side immersed in water

Figures 2.3(a)-2.3(c) present the mode shapes of quasi-Scholte waves at 100 kHz-mm, 300 kHz-mm, and 500 kHz-mm as denoted by the three red dots in Figure 2.2(a). It should be noted that the mode shape diagram only demonstrates the maximum amplitudes of the in-plane displacements and the out-of-plane displacements. A 1mm thick steel plate is located in the upper region while the bottom region represents the half-space water area. It can be seen that the displacements in the plate comprise the main part of the total displacements at the frequency-thickness range lower than 300 kHz-mm. This range is known as the dispersive region, in which the phase velocity of quasi-Scholte waves changes significantly with the product of the frequency and plate thickness as shown in Figure 2.2(a). The range of frequency-thickness over 300 kHz-mm is the non-dispersive region. In this region, the phase velocity of the quasi-Scholte wave is almost constant. However, the deformation of the modeshape in the plate is negligible compared to the deformation of the modeshape in the water as shown in Figure 2.3(c). Due to this observation, the quasi-Scholte wave in the non-dispersive region cannot be detected from the dry plate surface since most of the wave energy concentrates at the waterside of the submerged plate. Therefore, the rest of the study focuses on the frequency-thickness product values lower than 300 kHz-mm.

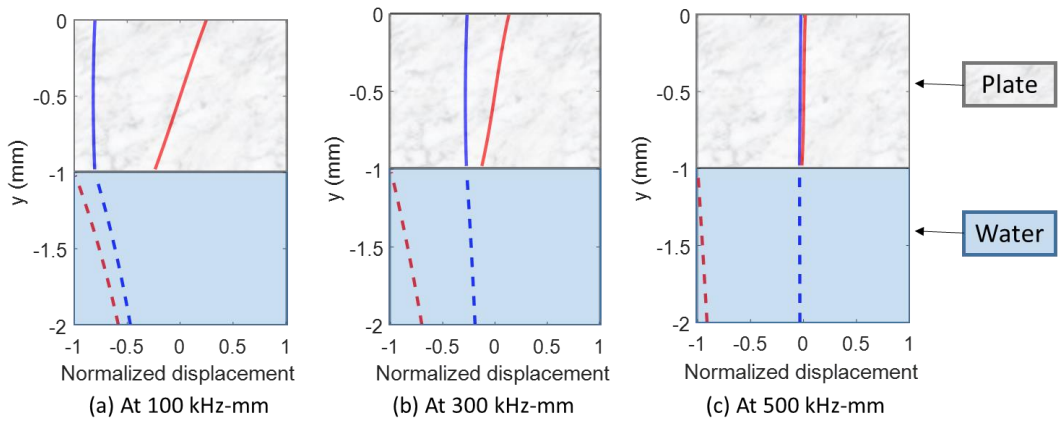

Figure 2.3. Theoretical mode shapes of quasi-Scholte waves at (a) 100 kHz-mm, (b) 300 kHz-mm, and (c) 500 kHz-mm. (red line denotes in-plane displacements; blue line denotes out-of-plane displacements)

2.4. Wave propagation and interaction simulation

3D FE simulation was used to simulate guided wave propagation on a steel plate loaded with water on a single side. The commercial FE software, ABAQUS, was used to generate the geometry and mesh the FE model. This study aims to investigate the interaction of quasi-Scholte waves with blind holes, which is a local phenomenon. Therefore, only a rectangular section of the plate was modeled with absorbing regions attached to its edges to reduce unwanted waves reflected from the boundaries and improve the computational efficiency. Figure 2.4 shows the configuration of the 3D FE model. The dimension of the steel plate was 270 mm × 320 mm × 2 mm ($W \times L \times H$) with 40 mm wide absorbing regions applied to its edges. The bottom surface was in contact with a 100 mm thick water layer. Table 2.1 summarizes the material properties of the steel plate and the water for the 3D FE model. The plate and absorbing regions were discretized by 3D eight-node reduced integration solid elements (C3D8R). The water layer was modeled using 3D eight-node reduced integration acoustic elements (AC3D8R). The interface between the water and the steel plate was defined by surface-based tie constraint in ABAQUS/Explicit, which tied the acoustic pressure on the fluid surface with the displacements on the solid surface [29]. This allowed the wave energy in the plate to transmit into the water through the out-of-plane displacements.

Table 2.1 Material properties of the steel and water used in the 3D FE model

	Density (kg/m^3)	Young's modulus (GPa)	Poisson's ratio	Bulk modulus (GPa)
Plate	7800	200	0.3	--
Water	1000	--	--	2.2

The guided waves were excited on the top water-free surface through applying the out-of-plane nodal displacements by a 5 mm diameter circular transducer [30, 31]. The excitation signal was a five-cycle Hann window-modulated sinusoidal tone bust [32]. In order to compare the FE simulations with experiment results, the excitation frequency in this study was selected as 100 kHz, at which the

measured signal in the experiment had the highest signal-to-noise ratio. At this excitation frequency, the theoretical wavelength of the selected wave mode, the quasi-Scholte wave, was around 10 mm as predicted by the phase velocity dispersion curves. Then, the in-plane dimension of the solid elements in the plate was set as 0.5 × 0.5 mm^2, which was small enough to ensure that at least ten elements exist per wavelength of the selected wave mode as recommended in the literature to simulate guided wave interaction with defects [33, 34]. Eight layers of solid elements were used in the thickness direction, by which the aspect ratio of the elements was two. A convergence study was implemented to confirm that the accuracy of the simulation results using elements with the aspect ratio of two was the same as that using the cubic elements.

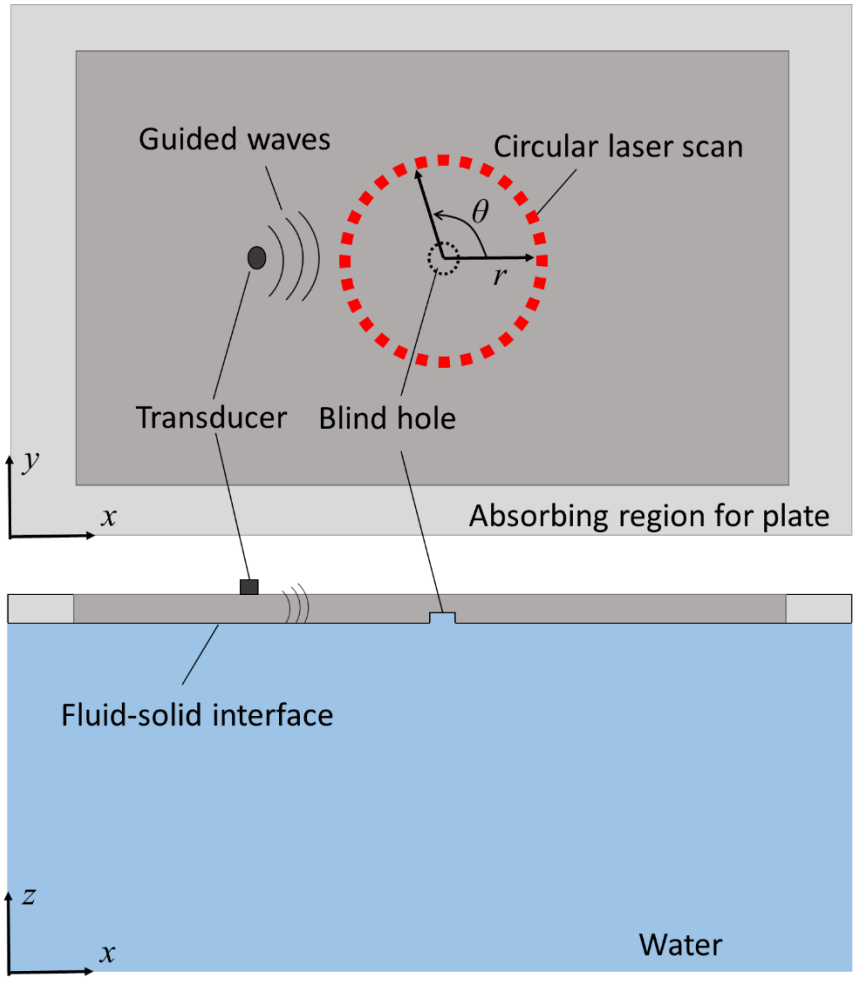

Figure 2.4. Schematic diagram of the configuration used in FE simulation

The absorbing regions located at the four edges of the plate were divided into 40 layers of which the mass-proportional damping coefficients (C_M) gradually increased from the innermost layer to the outmost layer. The absorbing layers can avoid the wave reflections from the boundaries, and hence, it allows using a small FE model to analyze the wave propagation and the scattering phenomena in a large structure. The mass-proportional damping coefficient of each absorbing layer was defined as [35, 36]

$$C_M = C_{M\max} X(x^3) \tag{2.4}$$

where x represents the distance between the current layer and the interface between the absorbing regions and the steel plate; $X\left(x^3\right)$ denotes a function of x, whose value varies from 0 when $x = 0$ to 1 at the outmost layer of the absorbing region $x = x_{\max}$; $C_{M\max}$ is the mass-proportional damping coefficient of the outmost layer in the absorbing region and was set as 3×10^6, which was obtained by trial and error [37].

The dynamic simulations were accomplished by the explicit module of ABAQUS, which used the central-difference integration. For wave propagation problems, it is recommended that the time step increment should be less than the ratio of the minimum element size to the speed of the dilatational wave. In this study, the increment time step was automatically determined by ABAQUS in all simulations [38].

Figures 2.5(a) and 2.5(b) present the snapshots of the simulated out-of-plane displacements in the 2 mm thick one-side water-immersed steel plate before and after the guided wave interaction with a circular blind hole, respectively. The excitation frequency was 100 kHz and the corresponding frequency-thickness product was 200 kHz-mm, which was in the dispersion region of quasi-Scholte waves. The diameter and depth of the blind hole were 10 mm and 1.5 mm, respectively. Guided waves were excited and propagated omnidirectionally and gradually diminished when they reached the absorbing layers as shown in Figure 2.5(b). There were no obvious boundary reflections observed from the plate edges. After the interaction of the incident waves with the circular blind hole, part of wave

energy transmitted through and there were some waves reflected from the blind hole. Figures 2.5(c) and 2.5(d) show the contour snapshot of the corresponding acoustic pressure in the water. It can be seen that there was only one wave packet observed in the plate. This wave packet had a flexure mode shape and most of the wave energy was confined to the water-plate interface rather than radiating into water. Due to these features, it was identified that this wave packet was related to the quasi-Scholte mode. The simulation results demonstrated that the out-of-plane excitation on the surface of the one-sided water-loaded plate dominantly generates the quasi-Scholte waves that are able to detect damage at the water-plate interface by wave scattering.

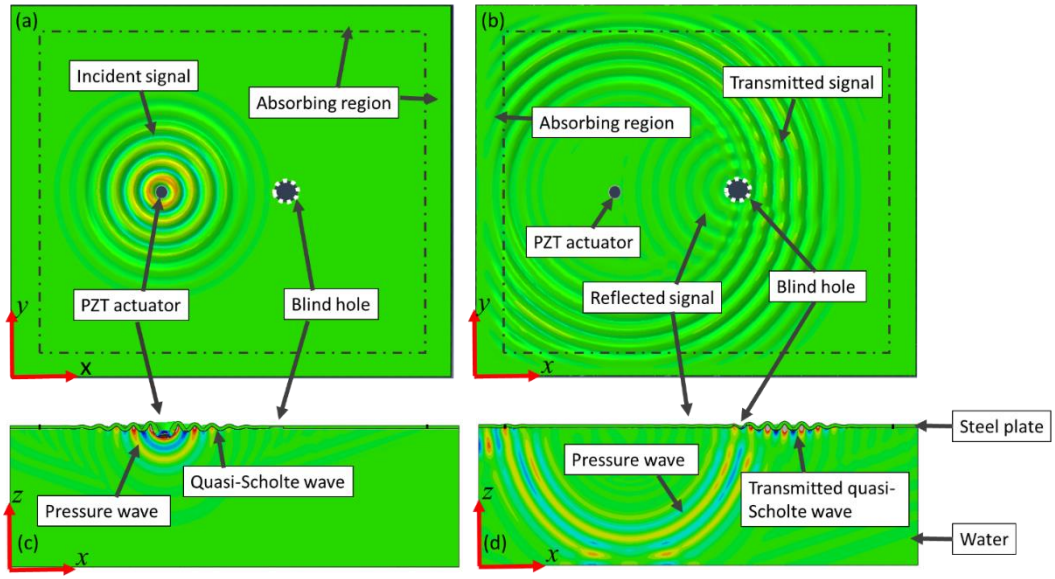

Figure 2.5. Snapshots of the simulated out-of-plane displacements in a 2 mm thick one-side water-immersed steel plate at different time instances; (a) before the incident wave reaches the circular blind hole; (b) after interaction of the incident wave with the circular blind hole; (c) and (d) the corresponding contour snapshots of the acoustic pressure.

2.5. Experimental validation

To study the wave propagation in a plate with one side exposed to water, a test metal tank was designed with the front wall being the test plate as shown in Figure

2.6(a). The test plate was a 2 mm thick steel plate and the material properties are given in Table 2.1. During the test, the metal tank was filled with water so that the internal surface of the test plate was in contact with water while the external surface of the test plate was exposed to the air. To validate the accuracy of the 3D FE model to simulate guided wave scattering phenomena, a blind hole was drilled at the internal surface of the test plate to model a corrosion pit (see, Figure 2.6(b)). A Cartesian coordinate system was defined with the origin being located at the left bottom of the test plate (see, Figure 2.6(a)). A circular piezoceramic transducer (5 mm diameter, 2 mm thickness) was mounted to the outer side (water-free surface) of the test plate at x = 200 mm and y = 200 mm, and it was used as the actuator to excite guided wave bursts. The excitation signal was generated by a function generator (AFG 3021B) and the voltage was increased by an amplifier (Krohn-Hite 7500). The out-of-plane displacements at various scanning points were measured by the non-contact laser scanning Doppler vibrometer (Polytec PSV-400-M2-20). The excitation signal was a five-cycle Hann window-modulated sinusoidal tone burst. The experimentally measured data were collected with a sampling rate of 10.26 MHz. The measured signals were filtered by applying a band-pass filter and averaging procedure applied to 1000 recordings. The overall experiment setup is shown in Figure 2.6(c).

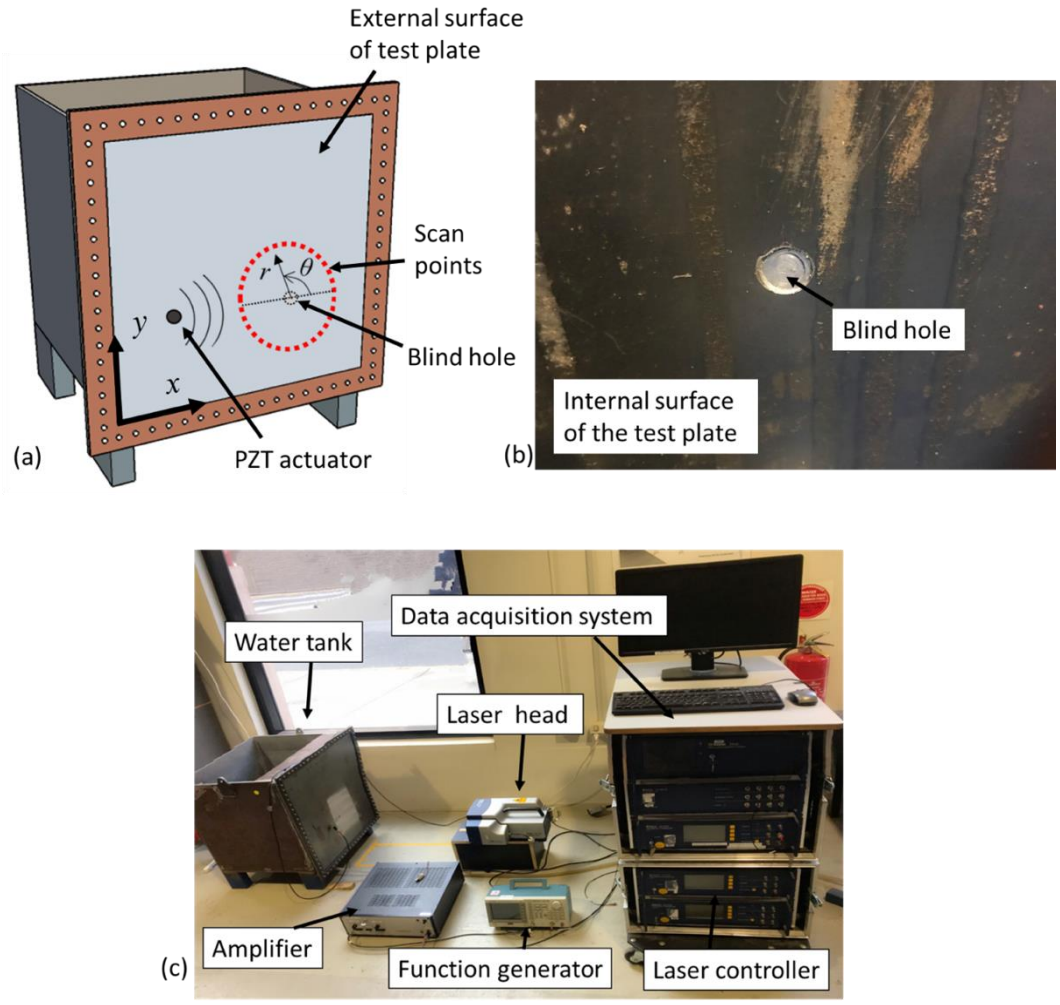

Figure 2.6. (a) Schematic diagram of the water tank and; (b) blind hole at the internal surface of the test plate; and (c) the experiment setup

2.5.1. Verification of the intact FE model

This section details the outcomes of the experimental study on guided wave propagation in the intact steel plate (before drilling the blind hole) with one side exposed to water. Figure 2.7(a) compares the FE simulated and experimentally measured signal in the time domain and the excitation frequency is 100 kHz. There is good agreement between the FE simulations and experimental measurements. The results confirm that the signal measured at the water-free surface of the one-side water-immersed plate is dominated by a single wave packet, which is identified as the quasi-Scholte mode as discussed in Section 2.4. At such excitation frequency, leaky S_0 waves have negligible out-of-plane components [15, 39] and the

magnitudes of leaky A_0 waves are too small to be observed due to its high attenuation characteristics as shown in Figure 2.2(b). To further investigate the accuracy of the 3D FE model, the phase velocity dispersion curves were calculated with the same strategy for the experimental measurements and FE simulations.

The excitation frequency was swept from 70 kHz to 150 kHz in steps of 10 kHz. In this frequency range, the measured signals had a good signal-to-noise ratio in the experiment. At each excitation frequency, the out-of-plane displacements were collected at eleven points along the horizontal direction with a spatial step of 2 mm, which was less than half of the wavelength of the quasi-Scholte wave mode. The measured time domain signals were then transformed into the frequency domain by fast Fourier transform (FFT). After that, the phase of each measured signal was calculated and the phase velocity between two measurements was calculated by

$$C_p = \frac{2\pi f \Delta\phi}{\Delta x} \tag{1}$$

where $\Delta\phi$ and Δx are the phase difference and distance between the two measurement points, respectively. C_p and f are the phase velocity and the central frequency of the excitation, respectively. The phase velocity at each excitation frequency was determined by taking the average of the calculated phase velocities at the measurement points. Figure 2.7(b) presents the phase velocity dispersion curves of quasi-Scholte waves calculated by DISPERSE, FE simulations, and experimental measurements. The maximum deviation is less than 2%. There is good agreement between the theoretically calculated, numerically simulated, and experimentally measured phase velocity dispersion curves.

The measured signals were also converted into the time-frequency spectrum by short-time Fourier transform (STFT) to determine the traveling time of quasi-Scholte waves. The group velocity was calculated by

$$C_g\left(f_c\right) = \frac{\Delta x}{\Delta t} \tag{2}$$

where Δt is the difference of the time of arrival between the two measurement points, which were away from each other by Δx. For the excitation frequency of 100 kHz, the group velocities obtained from the FE simulations and the experimental measurements are 2143 m/s and 2131 m/s, respectively. They are very close to the theoretical value of 2143 m/s calculated by DISPERSE. Therefore, it can be concluded that the FE model can accurately simulate the wave on the steel plate loaded with water on a single side.

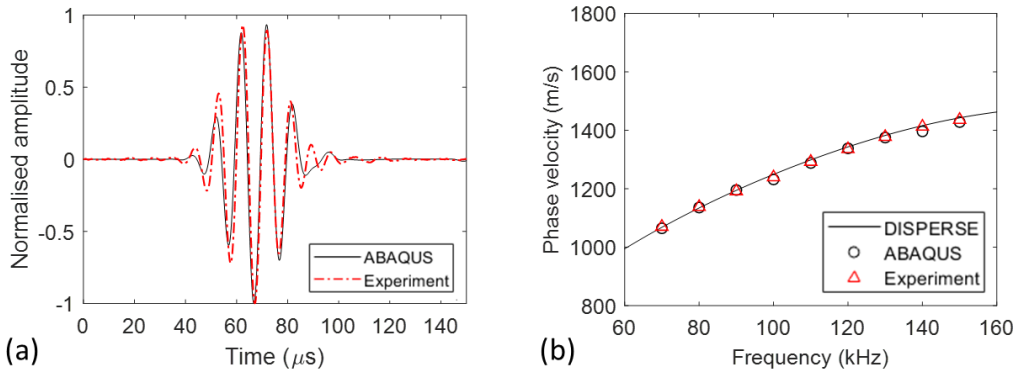

Figure 2.7. (a) Typical FE simulated and experimentally measured signal at 100 kHz (black solid lines: simulation results; red dash lines: experimental results); (b) Phase velocity dispersion curves from the theoretical calculation (solid black line), FE simulations (black circles), and experimental measurements (red triangles).

2.5.2. Guided wave scattering at a blind hole

The accuracy of wave scattering simulation using the 3D FE model was investigated through experimental measurements. A circular blind hole was drilled at the internal surface of the plate as shown in Figure 2.6(b). The depth and the diameter of the blind hole were measured to be 1.3 mm and 12 mm, respectively. A polar coordinate system was defined with the origin being the center of the blind hole as shown in Figure 2.6(a). Incident waves were excited by a piezoceramic transducer located at r = 80 mm and θ = 180°. A scanning laser Doppler vibrometer was employed to scan a circular path covered by 36 points at r = 50 mm, from 0° to 360° with the increment step of 10°. The 3D FE model of the damaged plate with the same dimensions has a blind hole at the water-plate interface. The same strategy

was employed to obtain the simulated out-of-plane displacements at the same 36 locations at the top surface (water-free surface).

Figure 2.8(a) shows a typical signal obtained from the FE simulations and experimental measurements. The measurement point was located at r = 50 mm and θ = 170^{o}. The incident wave was the selected interface wave mode, the quasi-Scholte wave, and a small magnitude of the scattered wave, which was generated by the interaction of the quasi-Scholte wave with the blind hole. There is a small phase shift in the scattered waves, which could be the result of a small misalignment of the blind hole between the 3D FE model and the experiment. However, the simulated scattering amplitudes relative to the incident wave were consistent with the experimental measurements. Figure 2.8(b) shows the maximum absolute amplitudes of the simulated and the experimentally measured signals, where the amplitudes were normalized by the peak amplitudes of the signal at r =50 mm and θ =180^{o}. In general, the 3D FE model well predicted the experimental results. It should be noted that although this study focuses on a particular excitation frequency, the 3D FE model can simulate wave propagation for other excitation frequencies as long as the size of elements is small enough to meet the minimum number of the FE nodes per wavelength requirement.

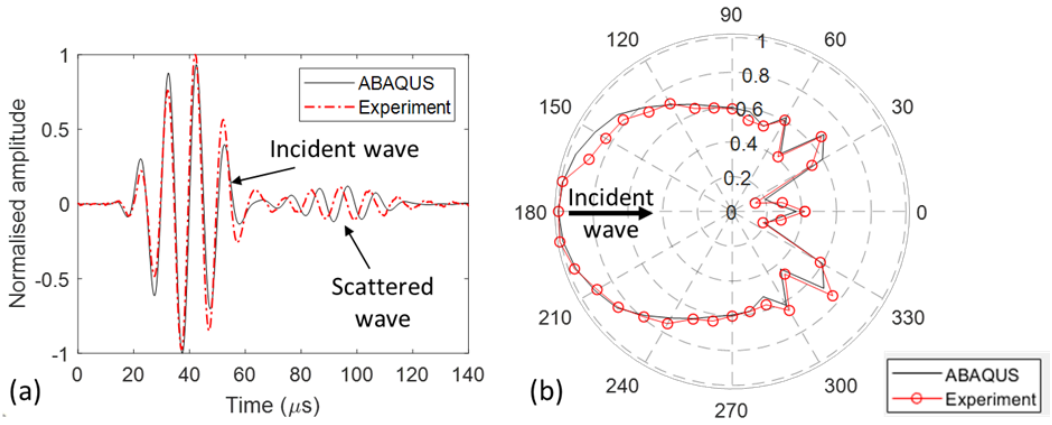

Figure 2.8. (a) FE simulated and experimentally measured signal at r =50 mm, θ =170^{o} of the one-side water-immersed steel plate with a blind hole; (b) Polar directivity patterns of the normalized maximum absolute amplitudes of quasi-Scholte waves measured on the circular path.

2.6. Scattering of quasi-Scholte waves due to circular blind holes at the water-plate interface

The experimentally validated 3D FE model was employed in a series of parametric studies to analyze the scattering characteristics of quasi-Scholte waves at circular blind holes at the water-plate interface. The simulations were carried out for the model with and without the blind hole so that the scattered waves could be extracted by subtracting the signals of the intact model from those measured from the model with the blind hole. The center of the blind hole was set as the origin of the polar coordinate system. Guided waves were generated on the water-free side by a 5 mm diameter circular transducer, of which the center was located at r = 80 mm and θ = 180^o. The normal displacements were obtained at 36 nodal points which were located at r = 50 mm and 0^o < θ < 360^o with a 10^o step increment. Then, the SDPs were determined by plotting the maximum magnitudes of the scattered waves in all directions around the blind hole. The amplitudes of the SDPs were normalized by the maximum absolute amplitudes of the wave signal at r =50 mm and θ =180^o. Figures 2.9(a)-2.9(c) show the SDPs of the 100 kHz incident quasi-Scholte waves at the 2 mm, 6 mm, and 10 mm diameter circular blind holes with the depth of 0.5 mm located at the water-plate interface. The results indicate that the SDPs are dependent on the size of the circular blind hole. For the 2 mm diameter circular blind hole, the amplitudes of the reflected waves are comparable to the forward scattering amplitudes. However, the forward scattered waves increase significantly for the blind hole with larger diameters. The following sections investigate the effect of the diameter and the depth of the blind hole on the SDPs.

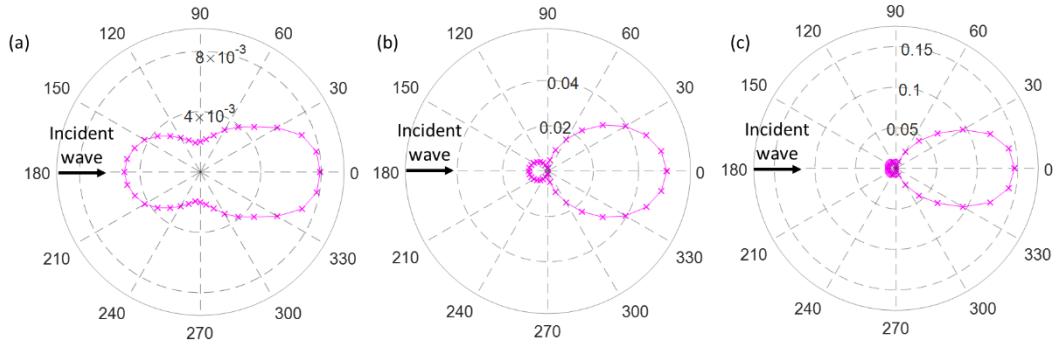

Figure 2.9. SDPs for the one-side water-loaded plate with (a) 2 mm, (b) 6 mm, and (c) 10 mm diameter circular blind hole with 0.5 mm depth.

2.6.1. Influence of the diameter of the circular blind hole

The SDPs of quasi-Scholte waves have been shown to change significantly with the size of the blind hole. This section explores the effect of the diameter of the blind hole on the scattering phenomenon in terms of the blind hole diameter to wavelength ratio (RDW). For a circular blind hole with a depth of 0.5 mm, the forward scattering amplitudes are given in Figure 2.10(a) at θ = 0º, 20º, 40º, 60º, 80º, 280º, 300º, 320º, and 340º. For θ = 0º, 20º, and 340º, the amplitudes increase with RDW and have relatively larger amplitudes than those in other directions. The scattering amplitudes at θ = 40º and 320º rise until the RDW reaches 1.2 then reduce with RDW. The magnitudes of the scattered waves at θ = 60º, 80º, 280º, and 300º are small and exhibit slight fluctuation with RDW.

Figure 2.10(b) presents the backward scattering amplitudes at θ = 100º, 120º, 140º, 160º, 180º, 200º, 220º, 240º, and 260º. It can be seen that the overall behavior of the scattering magnitudes in the backward direction is much more complicated than that in the forward direction. For θ = 180º, 200º, 160º, 220º, 140º, 240º, and 120º, the amplitudes fluctuate following a sinusoidal pattern but the overall trend is a slow increase. The minima of the scattering amplitudes at θ = 220º and 140º and θ = 240º and 120º are obtained with RDW of around 1.2, which are slightly behind the minima of scattered waves at θ = 180º, 200º, and 160º. Additionally, the amplitudes at θ = 260º and 100º are considerably small and show moderate variation with RDW. In general, the amplitudes of the backward scattered waves are smaller than those in the forward directions. Besides, the scattering amplitudes are almost

negligible in the directions perpendicular to the incident waves. Therefore, a sensor located at these directions is unlikely to detect any differences between damaged and undamaged plates.

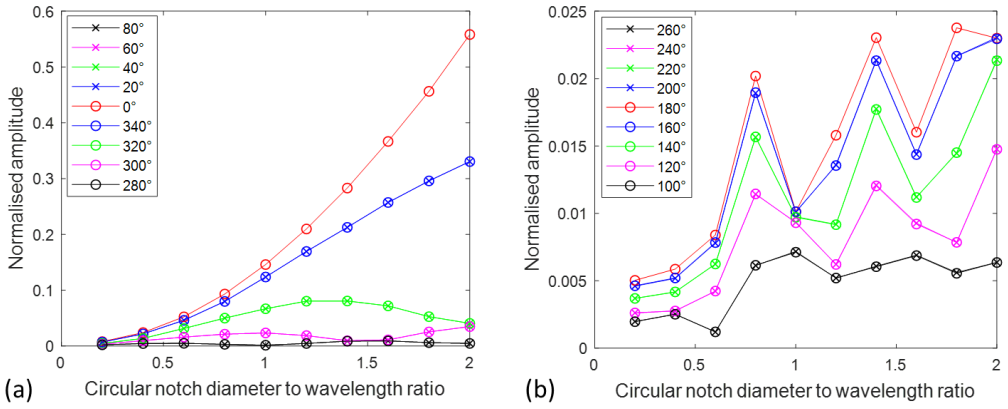

Figure 2.10. Normalized amplitudes for (a) the forward scattered waves and (b) the backward scattered waves at a circular blind hole in the one-side water-loaded steel plate as a function of RDW.

2.6.2. Influence of the depth of the circular blind hole

The above section demonstrates that the scattering characteristics are dependent on RDW. This section shows that the SDPs of quasi-Scholte waves also relate to the depth of the circular blind hole. Figures 2.11(a) and 2.11(b) show the SDPs of the 100 kHz incident quasi-Scholte waves at the 6 mm diameter circular blind hole with the depth being 1.0 mm and 1.5 mm located at the water-plate interface. Both the forward and backward scattering amplitudes increase with the depth of the blind hole. For shallow blind holes (Figures 2.9(b) and 2.11(a)), the forward scattering amplitudes are much larger than the magnitudes of the backward scattered waves. However, the backward and forward scattering amplitudes are comparable in the case of deeper damage (Figure 2.11(b)). In addition, the scattering amplitudes at the directions perpendicular to the incident wave are weak for shallow damage (Figures 2.9(b) and 2.11(a)) but they become comparable to those in other directions for the deeper blind hole (Figure 2.11(b)). Therefore, it can be seen that both the diameter and depth of the blind hole have a significant influence on the SDPs.

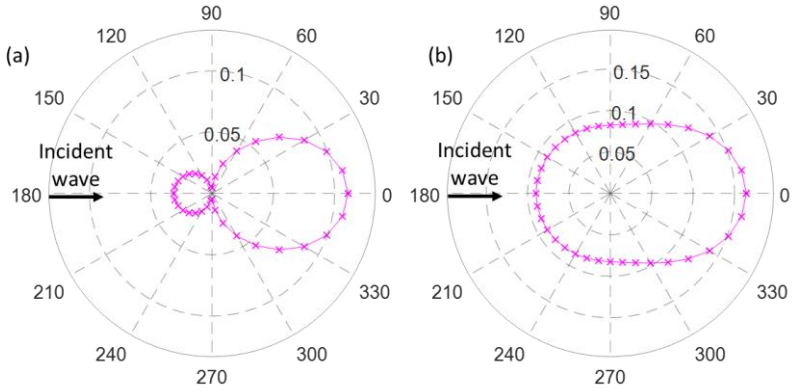

Figure 2.11. SDPs for the one-side water-loaded plate with a 6 mm diameter circular blind hole with a depth of (a) 1.0 mm and (b) 1.5 mm

2.7. Advantages of quasi-Scholte waves for damage detection

In the foregoing studies, it has been demonstrated that it is feasible to utilize guided waves for detecting damages in submerged structural components. One of the biggest challenges in terms of practical applications is that guided waves have multimodal features. For example, within the frequency-thickness range up to 1 MHz-mm, there are only quasi-Scholte waves, leaky A_0 waves, and leaky S_0 waves existing simultaneously on the one-side water-loaded steel plate. Other higher-order wave modes will appear if the excitation frequency is higher [9]. When the measured signals contain multiple guided wave modes, it is very difficult to extract the damage-related wave signals that convey the information about the damage. Therefore, the use of guided waves at low excitation frequencies for damage detection is much more preferable since the measured signal has limited guided wave modes, which does not require sophisticated signal processing techniques.

Among these aforementioned three wave modes at the low-frequency band, leaky A_0 waves and leaky S_0 waves continuously radiate energy into the surrounding medium. Leaky A_0 waves have mostly out-of-plane displacements and decay rapidly due to the significant energy leakage into water. While leaky S_0 waves have a small attenuation because it is dominated by the in-plane motions. But leaky S_0 waves are relatively insensitive to shallow surface corrosion since most of it is

wave energy is confined to the mid-plane region of the plate [13, 40]. Unlike the leaky A_0 mode and the leaky S_0 modes, the quasi-Scholte mode is an interface wave mode whose energy is confined to the water-plate interface instead and does not significantly radiate into the water. This behavior enables the quasi-Scholte wave mode to travel over long distances with very low attenuation. In addition, the quasi-Scholte wave mode has a much smaller wavelength than leaky A_0 waves and leaky S_0 waves, which means that quasi-Scholte waves are more sensitive to small-scale damage at the same excitation frequency. Sections 2.4 and 2.5 have numerically and experimentally demonstrated that at low frequencies, quasi-Scholte waves dominate over other wave modes when a circular piezoceramic transducer is installed on the water-free surface of the one-side water-immersed plate to excite guided waves. This phenomenon indicates that damage in the submerged structures can be potentially detected and evaluated based on a single wave mode. This significantly simplifies the practical implementations. In recognition of the above observations, it can be finally concluded that the quasi-Scholte wave mode is promising for damage detection in submerged structures. However, it should be noted that only the quasi-Scholte waves at the low frequency-thickness range (in the dispersive region) could be applicable for detecting damage in the submerged structures. Because at higher frequencies where the quasi-Scholte mode is non-dispersive, the signal of quasi-Scholte waves cannot be detected from the plate surface since the displacements in the plate are negligible compared to the displacements in the water (see Figure 2.3).

2.8. Conclusion

This paper has presented a study on guided wave propagation in a steel plate with one side immersed in water for SHM application on water-filled tanks and pipes, in particular, the focus has been directed on the interface wave mode, quasi-Scholte waves, and its scattering characteristics at circular blind holes. This interface wave mode at low frequencies has low attenuation and most of the excitation energy is conserved in the structures during the propagation. A 3D FE model has been developed to simulate the guided wave propagation in a steel plate exposed to water on one side. It has been confirmed that the signal measured from the water-free

surface of the one-side water-immersed plate, which is excited by a circular piezoceramic transducer, is dominated by quasi-Scholte waves. The accuracy of the simulation results has been verified by comparing the phase velocities with the theoretical dispersion curves as well as the experimental measurements. The numerical simulations of wave scattering of the quasi-Scholte mode at a circular blind hole have been compared with the experimental measurements. A good agreement has been observed between the FE simulations and experimental measurements. It has been concluded the 3D FE model is able to accurately simulate quasi-Scholte wave propagation and its scattering characteristics for non-regular geometries.

Further numerical studies have demonstrated that the scattering directivity patterns (SDPs) depend on both the diameter and the depth of the circular blind hole. At a given depth of the damage, the amplitudes of the backward scattered waves are comparable to the forward scattering amplitudes for small values of RDW. For larger RDW, the forward scattering amplitudes increase quickly with slight variation while the backward scattering magnitudes fluctuate following a sinusoidal pattern with the overall trend being a slow increase. In general, the forward scattered waves are more suitable to be used for identifying the size of the damage since they have larger amplitudes and follow a relatively simple scattering pattern. For the local damage of the same diameter, the forward and backward scattering amplitudes increase with the depth of the damage. The backward scattering amplitudes increase faster than the forward scattered waves. Also, for the directions perpendicular to the incident wave, the scattering amplitudes are weak for damage whose depth is less than half of the plate thickness but significantly increase for deeper damage.

Finally, this study has provided a comprehensive investigation of the scattering phenomena due to low-frequency quasi-Scholte waves interacting with a circular blind hole. The findings of this study can be used to provide a guide on selecting appropriate excitation frequencies, guided wave modes, and transducer locations, and hence, it will help to improve the performance of in-situ damage detection techniques for structures exposed to the corrosive environment.

2.9. Acknowledgment

This work was funded by the Australia Research Council (ARC) under the grant number DP200102300. The authors are grateful for this support.

2.10. References

[1] C. Yeung, C.T. Ng, Time-domain spectral finite element method for analysis of torsional guided waves scattering and mode conversion by cracks in pipes, Mechanical Systems and Signal Processing, 128 (2019) 305-317.

[2] Z. Zhang, C. Zhan, K. Shankar, E.V. Morozov, H.K. Singh, T. Ray, Sensitivity analysis of inverse algorithms for damage detection in composites, Composite Structures, 176 (2017) 844-859.

[3] T. Zheng, W. Luo, R. Hou, Z. Lu, J. Cui, A novel experience-based learning algorithm for structural damage identification: simulation and experimental verification, Engineering Optimization, (2019) 1-24.

[4] M. Mitra, S. Gopalakrishnan, Guided wave based structural health monitoring: A review, Smart Materials and Structures, 25 (2016) 053001.

[5] X. Yu, Z. Fan, M. Castaings, C. Biateau, Feature guided wave inspection of bond line defects between a stiffener and a composite plate, NDT & E International, 89 (2017) 44-55.

[6] H. Qi, M. Xiang, J. Guo, Scattering of a shear horizontal wave by a circular cavity in a piezoelectric bi-material strip based on guided wave theory, Mathematics and Mechanics of Solids, 25 (2020) 968-985.

[7] C.A. Chua, P. Cawley, P.B. Nagy, Scattering of the Fundamental Shear Guided Wave From a Surface-Breaking Crack in Plate-Like Structures, IEEE Transactions on Ultrasonics, Ferroelectrics, and Frequency Control, 66 (2019) 1887-1897.

[8] G.T. Pudipeddi, C.-T. Ng, A. Kotousov, Mode Conversion and Scattering of Lamb Waves at Delaminations in Composite Laminates, Journal of Aerospace Engineering, 32 (2019) 04019067.

[9] A.E. Takiy, C. Kitano, R.T. Higuti, S.C.G. Granja, V.T. Prado, L. Elvira, O. Martínez-Graullera, Ultrasound imaging of immersed plates using high-order Lamb modes at their low attenuation frequency bands, Mechanical Systems and Signal Processing, 96 (2017) 321-332.

[10] W.-B. Na, T. Kundu, Underwater pipeline inspection using guided waves, Journal of pressure vessel technology, 124 (2002) 196-200.

[11] J. Chen, Z. Su, L. Cheng, Identification of corrosion damage in submerged structures using fundamental anti-symmetric Lamb waves, Smart Materials and Structures, 19 (2009) 015004.

[12] E. Pistone, K. Li, P. Rizzo, Noncontact monitoring of immersed plates by means of laser-induced ultrasounds, Structural Health Monitoring, 12 (2013) 549-565.

[13] S. Sharma, A. Mukherjee, Damage detection in submerged plates using ultrasonic guided waves, Sadhana, 39 (2014) 1009-1034.

[14] F.B. Cegla, P. Cawley, M.J.S. Lowe, Material property measurement using the quasi-Scholte mode—A waveguide sensor, The Journal of the Acoustical Society of America, 117 (2005) 1098-1107.

[15] Z. Tian, L. Yu, Study on guided wave propagation in a water loaded plate with wavenumber analysis techniques, in: AIP Conference Proceedings, AIP, 2014, pp. 365-372.

[16] Z. Tian, L. Yu, Lamb wave structural health monitoring using frequency-wavenumber analysis, in: AIP Conference Proceedings, AIP, 2013, pp. 302-309.

[17] T. Hayashi, R. Fujishima, Defect detection using quasi-Scholte wave for plate loaded with water on single surface, Materials Transactions, (2016) M2016204.

[18] P.K. Jaya, L.R. Joseph, Mode controlled guided wave tomography using annular array transducers for SHM of water loaded plate like structures, Smart Materials and Structures, 22 (2013) 125021.

[19] C.-T. Ng, H. Mohseni, H.-F. Lam, Debonding detection in CFRP-retrofitted reinforced concrete structures using nonlinear Rayleigh wave, Mechanical Systems and Signal Processing, 125 (2019) 245-256.

[20] B. Masserey, P. Fromme, In-situ monitoring of fatigue crack growth using high frequency guided waves, NDT & E International, 71 (2015) 1-7.

[21] J.L. Rose, Ultrasonic guided waves in solid media, Cambridge university press, 2014.

[22] P. Rizzo, J.-G. Han, X.-L. Ni, Structural health monitoring of immersed structures by means of guided ultrasonic waves, Journal of Intelligent Material Systems and Structures, 21 (2010) 1397-1407.

[23] T. Hayashi, D. Inoue, Guided wave propagation in metallic and resin plates loaded with water on single surface, AIP Conference Proceedings, AIP Publishing, 2016, pp. 030003.

[24] T. Hayashi, D. Inoue, Calculation of leaky Lamb waves with a semi-analytical finite element method, Ultrasonics, 54 (2014) 1460-1469.

[25] P. Guo, B. Deng, X. Lan, K. Zhang, H. Li, Z. Tian, H. Xu, Water level sensing in a steel vessel using A0 and Quasi-Scholte waves, Journal of Sensors, 2017 (2017).

[26] L. Yu, Z. Tian, Case study of guided wave propagation in a one-side water-immersed steel plate, Case Studies in Nondestructive Testing and Evaluation, 3 (2015) 1-8.

[27] B. Pavlakovic, M. Lowe, Disperse user manual: a system for generating dispersion curves, Copyright B Pavlakovic, M Lowe, (2003).

[28] V. Aubert, R. Wunenburger, T. Valier-Brasier, D. Rabaud, J.-P. Kleman, C. Poulain, A simple acoustofluidic chip for microscale manipulation using evanescent Scholte waves, Lab on a Chip, 16 (2016) 2532-2539.

[29] Abaqus, Abaqus 6.13 Analysis User's Guide, Dassault Systems Simulia Corp, Providence, RI, (2013).

[30] Y. Yang, C.-T. Ng, A. Kotousov, Second harmonic generation of guided wave at crack-induced debonding in FRP-strengthened metallic plates, International Journal of Structural Stability and Dynamics, 19 (2019) 1940006.

[31] P. Aryan, A. Kotousov, C.-T. Ng, B. Cazzolato, A model-based method for damage detection with guided waves, Structural Control and Health Monitoring, 24 (2017) e1884.

[32] P. Aryan, A. Kotousov, C. Ng, S. Wildy, Reconstruction of baseline time-trace under changing environmental and operational conditions, Smart Materials and Structures, 25 (2016) 035018.

[33] D.N. Alleyne, P. Cawley, The interaction of Lamb waves with defects, IEEE transactions on ultrasonics, ferroelectrics, and frequency control, 39 (1992) 381-397.

[34] Y. Yang, C.T. Ng, M. Mohabuth, A. Kotousov, Finite element prediction of acoustoelastic effect associated with Lamb wave propagation in pre-stressed plates, Smart Materials and Structures, 28 (2019) 095007.

[35] P. Rajagopal, M. Drozdz, E.A. Skelton, M.J. Lowe, R.V. Craster, On the use of absorbing layers to simulate the propagation of elastic waves in unbounded isotropic media using commercially available finite element packages, NDT & E International, 51 (2012) 30-40.

[36] H. Mohseni, C.-T. Ng, Rayleigh wave propagation and scattering characteristics at debondings in fibre-reinforced polymer-retrofitted concrete structures, Structural Health Monitoring, 18 (2019) 303-317.

[37] J.R. Pettit, A. Walker, P. Cawley, M. Lowe, A stiffness reduction method for efficient absorption of waves at boundaries for use in commercial finite element codes, Ultrasonics, 54 (2014) 1868-1879.

[38] H. Mohseni, C. Ng, Higher harmonic generation of Rayleigh wave at debondings in FRP-retrofitted concrete structures, Smart Materials and Structures, 27 (2018) 105038.

[39] Q. Xie, C. Ni, Z. Shen, Defects detection and localization in underwater plates using laser laterally generated pure non-dispersive S0 Mode, Applied Sciences, 9 (2019) 459.

[40] S. Sharma, A. Mukherjee, Ultrasonic guided waves for monitoring corrosion in submerged plates, Structural Control and Health Monitoring, 22 (2015) 19-35.

Chapter 3. Numerical and experimental investigations on mode conversion of guided Waves in partially immersed plates

Abstract

This paper numerically and experimentally investigates the guided wave propagation in a steel plate with one side partly exposed to water. The fundamental anti-symmetric Lamb wave (A_0) is excited on the dry plate section and travels to the water-immersed plate section, where the generated A_0 wave is mode converted to the quasi-Scholte (QS) wave. The results demonstrate that the energy of QS wave converted by the A_0 wave decreases when the excitation frequency increases. In addition, it is revealed that the guided wave energy can shift in the frequency domain if the phase velocity of the incident A_0 wave is larger than the sound speed of water. The frequency shift phenomenon should be noticed in practical applications because the behaviors of guided waves vary with frequency. Finally, discussions are provided on the frequency selection for exciting guided waves to detect damage on partially immersed structures and assess liquid properties.

Keywords: Quasi-Scholte waves; Lamb waves; leaky guided waves; mode conversion; submerged structures.

Statement of Authorship

Title of Paper	Numerical and experimental investigations on mode conversion of guided waves in partially immersed plates
Publication Status	☑ Published ☐ Accepted for Publication ☐ Submitted for Publication ☐ Unpublished and Unsubmitted w ork w ritten in manuscript style
Publication Details	X. Hu, C.T. Ng, A. Kotousov (2022), Numerical and experimental investigations on mode conversion of guided waves in partially immersed plates, *Measurement*, 190, 110750.

Principal Author

Name of Principal Author (Candidate)	Xianwen Hu		
Contribution to the Paper	Conceptualization, Developing and validating numerical models, Conducting experimental measurements, Signal processing and data analysis, Writing the original draft and editing.		
Overall percentage (%)	80%		
Certification:	This paper reports on original research I conducted during the period of my Higher Degree by Research candidature and is not subject to any obligations or contractual agreements with a third party that would constrain its inclusion in this thesis. I am the primary author of this paper.		
Signature		Date	07/03/2022

Co-Author Contributions

By signing the Statement of Authorship, each author certifies that:

i. the candidate's stated contribution to the publication is accurate (as detailed above);
ii. permission is granted for the candidate in include the publication in the thesis; and
iii. the sum of all co-author contributions is equal to 100% less the candidate's stated contribution.

Name of Co-Author	Ching-Tai Ng		
Contribution to the Paper	Supervision, writing – review & editing.		
Signature		Date	9/3/2022

Name of Co-Author	Andrei Kotousov		
Contribution to the Paper	Supervision, writing – review & editing.		
Signature		Date	07/03/2022

Please cut and paste additional co-author panels here as required.

3.2. Introduction

Ultrasonic guided waves are elastic waves that travel along the boundary of a structure and have been widely used for identifying damage in structures [1-5], detecting debonding in adhesively bonded structures [6-9], sensing liquid levels and properties [10-12], and assessing coatings on the substrate surface [13, 14]. The advantages of ultrasonic guided waves are that they can propagate for a long distance, enabling an efficient large-area inspection. Lamb waves are guided waves in thin-walled structures, such as plates, shells, and pipes. When the plate is surrounded by air, Lamb waves are composed of multiple symmetric and anti-symmetric wave modes [15]. When one or both sides of the plate are exposed to liquid, there is a substantial increase in the energy leakage into the surrounding liquid medium [16, 17]. Therefore, guided waves in immersed plates are called leaky Lamb waves and they behave differently from their counterparts in the plates surrounded by air.

In addition to the symmetric and antisymmetric leaky Lamb wave modes, there is an interface mode called quasi-Scholte (QS) wave in the plate immersed in liquid [18]. Recently, studies have been conducted on the QS wave for a wide range of applications because of its ability to propagate along the plate-fluid interface over a long distance and high sensitivity to changes in the properties of both the plate and fluid. Tietze et al. [19] experimentally demonstrated that QS wave propagating at the interface between electrode and electrolyte is able to remove the diffusion boundary layer, which can be employed to accelerate the electrochemical process. Aubert et al. [20] invented a low-cost fluid manipulation device that employed the generation of QS wave to sort living cells and separate plasma from a blood microdroplet. Through schlieren imaging, the acoustic fields of the QS wave were experimentally visualized to be evanescent in the direction normal to the plate surface, which is a promising characteristic for microfluidic applications. Hayashi and Fujishima [21] experimentally confirmed that QS wave could be excited by applying the normal vibration directly on the surface of a plate loaded with water. The generated QS wave was shown to be sensitive to the change of the physical conditions on the plate surface. Thus, the QS wave is feasible for non-destructive testing (NDT) of water-filled storage tanks and pipes.

There are other studies focused on the application of QS wave, in which the QS wave is excited by mode conversion from the fundamental anti-symmetric mode (A_0) of Lamb waves. Cegla et al. [18] developed a novel method for sensing fluid property by exciting guided waves on a plate that was partially immersed in the fluid. A transducer was attached at the end of the dry plate section (outside the fluid) to excite A_0 wave. When the generated A_0 wave traveled from the dry section of the plate to the section immersed in the fluid, part of the wave energy was reflected backward, and the rest of the wave energy was converted into the leaky A_0 and QS waves. Leaky A_0 wave decayed rapidly and disappeared after a short propagation distance. While QS wave propagated along the immersed plate with low attenuation, and then reached the end of the immersed section and reflected back to the measurement location. At the point where the plate was outside the fluid, the QS wave was converted back to A_0 wave. The time-of-arrival and amplitude of the measured signals changed with the viscosity and bulk longitudinal velocity of the fluid, and hence, they could be employed to measure the fluid properties. Yu et al. [22] proposed a Lamb wave-based method for assessing liquid levels in the nuclear cooling pipe system. The method used a pair of piezoelectric wafer transducers that were mounted on the wall of a test tank. One of the transducers was used as an actuator and the other was used as a receiver. The wave signals were measured on the test tank filled with different amounts of water. It was found that the fundamental symmetric mode (S_0) of Lamb waves was not influenced by the change of water level. In contrast, the presence of water significantly changed both the amplitude and phase of A_0 wave. The phase change was shown to have a linear relationship with the change of water level. It should be noted that this study did not take into account the QS and leaky A_0 waves, which also exist in the water-immersed plate [21, 23].

Guo et al. [24] developed two-dimensional (2D) finite element (FE) models to simulate guided wave propagation along an empty steel vessel and the steel vessel filled with water, respectively. At the selected excitation frequency, A_0 and QS waves were identified on the water-free vessel and the water-filled vessel, respectively. The latter was found to propagate more slowly than the former. Therefore, the traveling time of the guided waves between two transducers could be also utilized for measuring the liquid level in the steel vessel. This study only

considered a single excitation frequency, at which the leaky A_0 wave mentioned in [18] was not detected in the water-immersed plate-like structure by both the 2D FE simulations and the experimental measurements [24].

The aforementioned studies employed the mode conversion between QS and A_0 waves at different excitation frequencies to achieve different applications, where the interactions among various guided wave modes were shown to be different. To date, there are very limited studies on the variation with frequency of the mode conversion phenomenon. However, studying the influence of excitation frequency on guided wave propagation is very important because the behaviors of guided waves are frequency-dependent. For example, it was reported that the displacements of the QS wave mainly occur in the liquid, and the majority of studies on QS wave had been focused on the fluid properties sensing [10, 18]. Only in recent years, its applications were extended to detect damage for plate structures submerged in liquid due to the observation that the QS wave at low frequencies has most of its wave motions conserved in the immersed plate [21, 25]. QS wave is dispersive at low frequencies and becomes nondispersive at high frequencies. The wave structure of QS wave at a low frequency significantly differs from that at a high frequency. Between the high and low frequencies, there is a frequency range, at which QS wave transitions from dispersive to nondispersive. In this frequency range, the wave structure of the QS wave changes rapidly with frequency, while that of the A_0 wave does not change much. Therefore, the mode conversion between QS and A_0 waves should also vary significantly with frequency, which has not been discussed in the literature.

In the present study, the frequency dependence of the mode conversion from A_0 wave to QS wave is studied numerically and experimentally. The findings of this study complement the current knowledge about guided wave propagation in partially immersed plates and provide a guide on selecting appropriate excitation frequencies for NDT of partially immersed structures and assessing liquid properties and levels. The numerical method using a three-dimensional (3D) FE model is proposed to portray guided wave propagation in a steel plate, of which one side is partly exposed to water. A_0 wave is excited at different frequencies on the dry section of the plate and travels to the immersed section. The simulation results

provide a visualization of the interaction of different guided wave modes in both the plate and water. Then, experiments are conducted on a steel tank that is partially filled with water. The time-space wave fields are captured by a scanning laser Doppler vibrometer (SLDV) before and after guided waves travel from the dry section of the plate into the immersed section. The mode conversion process is graphically shown with the use of 2D Fourier transform (FT). The experimental results show a good agreement with the numerical simulations. After that, the variation of the mode conversion from A_0 wave to QS wave with the excitation frequency is analyzed based on the theoretical dispersion curves and mode shapes of guided waves. Furthermore, it is observed that the energy of guided waves can shift in the frequency domain during the mode conversion process if the phase velocity of the incident A_0 wave is larger than the sound speed of the surrounding liquid medium. The energy shift in frequency can change the behaviors of guided waves, which should be paid attention to in practical applications.

The paper is organized as below. Section 3.3 compares the theoretical dispersion curves and mode shapes of guided waves in a plate surrounded by air and the plate with one side exposed to water. Section 3.4 describes the 3D FE model and presents the simulated guided wave fields in the partially immersed plate. After that, Section 3.5 shows the experimental setup and the configuration of measurement points. Section 3.6 illustrates the signal processing techniques and the analysis of experimentally measured signals. Then, Section 3.7 summarizes the frequency dependence of the mode conversion from A_0 wave to QS wave and explains the mechanism of the energy shift in frequency phenomena according to the theoretical dispersion curves and mode shapes of the guided waves. Based on the findings, the selection of appropriate excitation frequency is discussed for reliable testing through the mode conversion from A_0 wave to QS wave. Finally, conclusions are drawn in Section 3.8.

3.3. Guided waves in plates surrounded by air and plates with one side exposed to water

Guided waves behave differently in plates surrounded by air and plates immersed in water. When guided waves propagate in a plate in gaseous environments, there is a very small energy leakage from the plate to the air. The energy leakage to the air is not modeled in this study because the resistance of air to the displacements of particles at the plate surface is very small. As shown in Figure 3.1, traction-free boundary conditions are applied to the plate surface open to the air. In comparison, when one side of the plate is exposed to water, the out-of-plane displacements and stresses at the plate-water interface become continuous. The shear stresses are disconnected because water cannot sustain shear forces [26]. The energy leakage to the water layer is substantially larger than that to the air.

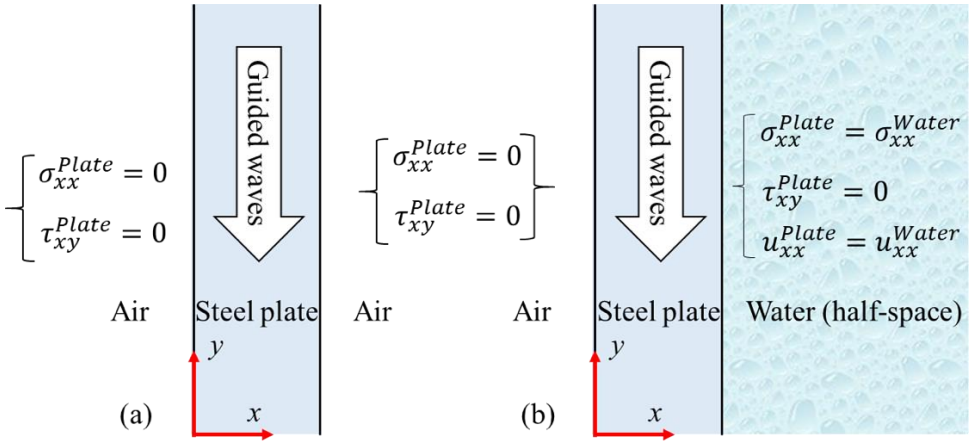

Figure 3.1. Guided wave propagation models and boundary conditions for (a) a dry plate surrounded by air, and (b) a plate with one side exposed to water

The properties of guided waves vary with frequency, which can be theoretically predicted by dispersion curves. The present study employed the global matrix method to calculate the dispersion curves and the theoretical results were used to interpret the following numerical and experimental data. Two guided wave propagation models were constructed using the commercially available software DISPERSE [27]. They were a 2 mm thick steel plate and the plate with water loaded

on one side, respectively. Table 3.1 gives the material properties of the steel plate and water. The water layer was defined as a semi-infinite half-space. The boundary conditions of the plate-air interface and plate-water interface were modeled by the solid-vacuum and solid-liquid interfaces, respectively. Based on the geometry and material properties, the stresses and displacements in the plate and water layers could be determined in terms of the partial waves. Then, a global matrix equation representing the whole model was assembled by matching the boundary conditions of each interface. The global matrix equation is a function of frequency, wavenumber, and attenuation. Solving this global matrix equation gives a series of combinations of frequency, wave number, and attenuation, at which the partial waves can combine to a guided wave mode that propagates on the plates in the directions as shown in Figure 3.1.

Table 3.1. Material properties of the steel and water

Material	Density (kg m^{-3})	Young's modulus (GPa)	Poisson's ratio	Bulk modulus (GPa)	Bulk wave velocity (m s^{-1})
Steel	7800	212.038	0.287	--	
Water	1000	--	--	2.2	1480

Figure 3.2 compares the dispersion curves of guided waves for the 2 mm thick steel plate surrounded by air and the plate with water loaded on its one side. At the frequency range up to 500 kHz, only A_0 and S_0 waves exist in the plate without water. They are represented by the green and blue dash-dot lines in Figure 3.2, respectively. The black solid lines, red dashed lines, and magenta dotted lines denote QS, leaky A_0, and leaky S_0 waves in the one-side water-immersed plate, respectively. The phase velocity C_p and the group velocity C_g can be related to the angular frequency w and the real wavenumber k as $C_p = w/k$ and $C_g = \partial w/\partial k$. As shown in Figure 3.2(c), the wavenumber dispersion curves of A_0 wave and S_0 wave are almost overlapped with those of leaky A_0 wave and leaky S_0 wave, respectively. It should be noted that leaky A_0 wave appears only after 150 kHz where its phase velocity is greater than the sound speed of the surrounding

water [28]. At a frequency lower than 150 kHz, the wavenumber of QS wave in the one-side water-immersed plate (black solid line) is just slightly larger than that of A_0 wave in the dry plate (green dash-dot line) and the difference between them increases with frequency.

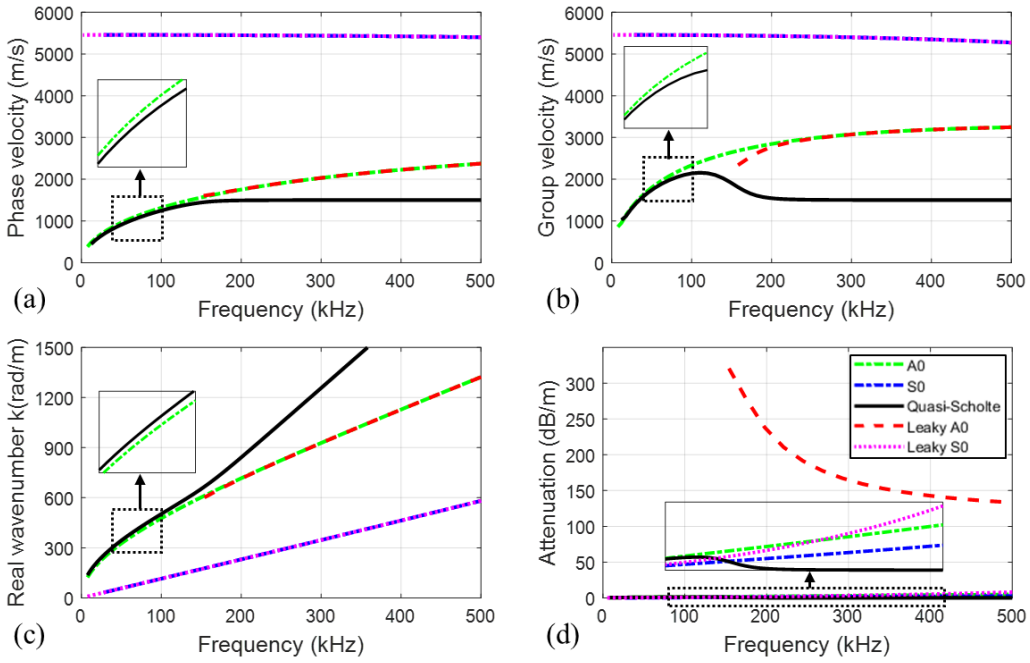

Figure 3.2. Comparison of dispersion curves of a 2 mm thick steel plate and the plate with one side exposed to water: (a) phase velocity curves; (b) group velocity curves; (c) wavenumber curves; (d) attenuation curves (the legends in Figure 3.2(d) are applied for Figures 3.2(a)-3.2(d)).

Figure 3.2(d) shows the attenuation dispersion curves where significant deviations can be observed between the dry plate and the one-side water-immersed plate. Obviously, leaky A_0 wave (red dashed line) has a much higher attenuation than any other wave mode. This is because leaky A_0 wave is dominated by the out-of-plane displacements so that the wave energy can easily and massively radiate into the surrounding water [29]. The attenuation dispersion curve of leaky A_0 wave declines sharply in the selected frequency range. This means that the low-frequency leaky A_0 wave has larger attenuation than the high-frequency leaky A_0 wave. The levels of attenuation of other wave modes are close for the frequency lower than

200 kHz. Over 200 kHz, the attenuation of QS wave drops to almost zero, while the attenuations of A_0, S_0, and leaky S_0 waves slowly increase with frequency. From the above observations, it can be concluded that when guided waves propagate from the dry plate to the water-immersed plate, S_0 wave is converted to leaky S_0 wave that has the same wavenumber but slightly higher attenuation. A_0 wave is converted to QS wave at a frequency lower than 150 kHz where both the wavenumber and attenuation of QS wave in the immersed plate are similar to those of A_0 wave in the dry plate. However, leaky A_0 wave appears when the excitation frequency exceeds 150 kHz. A_0 wave can be mode converted to both QS wave and leaky A_0 wave. Thus, the mode conversion process can be different with frequency.

The similarity between A_0 wave in the dry plate and QS wave in the one-side water-immersed plate is also studied by their mode shapes. The mode shape of a guided wave mode shows the distributions of the displacements through the thickness of the structure and it can be calculated using DISPERSE [27]. The frequency band of interest is selected from 100 kHz to 200 kHz, in which the wavenumber dispersion curves of the A_0 and QS waves gradually separate as the frequency increases. Figure 3.3 shows the mode shapes of A_0 wave at 100 kHz, 150 kHz, and 200 kHz for the 2 mm thick steel plate that is not in contact with water. The deformation of the dry plate is dominated by out-of-plane displacements denoted by the blue solid lines. As the frequency increases, the mode shape diagrams of A_0 wave do not display much difference.

Figure 3.4 shows the mode shapes of QS wave at 100 kHz, 150 kHz, and 200 kHz for the 2 mm thick steel plate with one side exposed to water. The water layer was defined as a semi-infinite half-space. As shown in Figure 3.4, the normalized displacement fields of the mode shapes in the water layer monotonically decrease with the distance away from the plate-water interface. To better compare the wave structures in the plate with and without water, the mode shape diagrams only show the 2 mm water regions near the plate-water interface. As shown in Figures 3.3(a) and 3.4(a), the deformation of QS wave in the immersed plate is similar to that of A_0 wave in the dry plate when the frequency is lower than 150 kHz. However, the deformation in the immersed plate of QS wave decreases rapidly with frequency. At frequencies above 150 kHz, most of the displacements of QS

wave occur in the water and the displacement fields in the immersed plate are very small (see Figures 3.4(b) and 3.4(c)). In general, when the frequency increases from 100 kHz to 200 kHz, QS wave changes significantly, while A_0 wave remains almost unchanged. Therefore, it is expected that as the frequency increases, the mode conversion from A_0 wave to QS wave should become more and more difficult since the similarity between the two wave modes reduces with frequency.

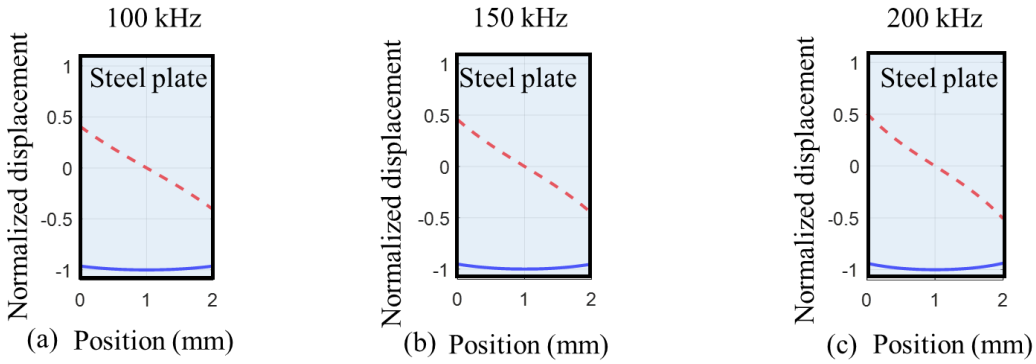

Figure 3.3. A_0 mode shapes for the 2 mm thick steel plate at (a) 100 kHz, (b) 150 kHz, and (c) 200 kHz (red dashed lines denote the in-plane displacements; blue solid lines denote the out-of-plane displacements)

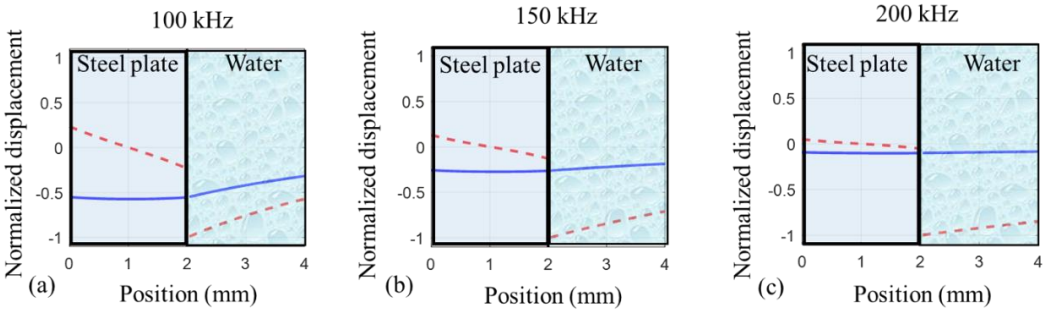

Figure 3.4. QS mode shapes for the 2 mm thick steel plate with one side exposed to water at (a) 100 kHz, (b) 150 kHz, and (c) 200 kHz (red dashed lines denote the in-plane displacements; blue solid lines denote the out-of-plane displacements)

3.4. Numerical simulation of guided wave propagation

To portray the guided wave propagation in partially water-immersed plates, a 3D FE model was developed using the commercial FE software ABAQUS. Table 3.1 gives the material properties used for the FE simulation. A 300 mm × 150 mm × 2 mm steel plate was modeled with symmetry boundary conditions applied to the top and right edges and absorbing regions attached to the left and bottom edges, as shown in Figure 3.5. The absorbing regions were 50 mm wide and were divided into 50 layers. The mass-proportional damping of the material in the absorbing regions gradually increased layer by layer from zero at the innermost layer to 4×10^6 at the outmost layer. The absorbing region by increasing damping can reduce unwanted waves reflected from the plate edges and has been widely used for ultrasonic guided wave simulation analysis [25, 30-33].

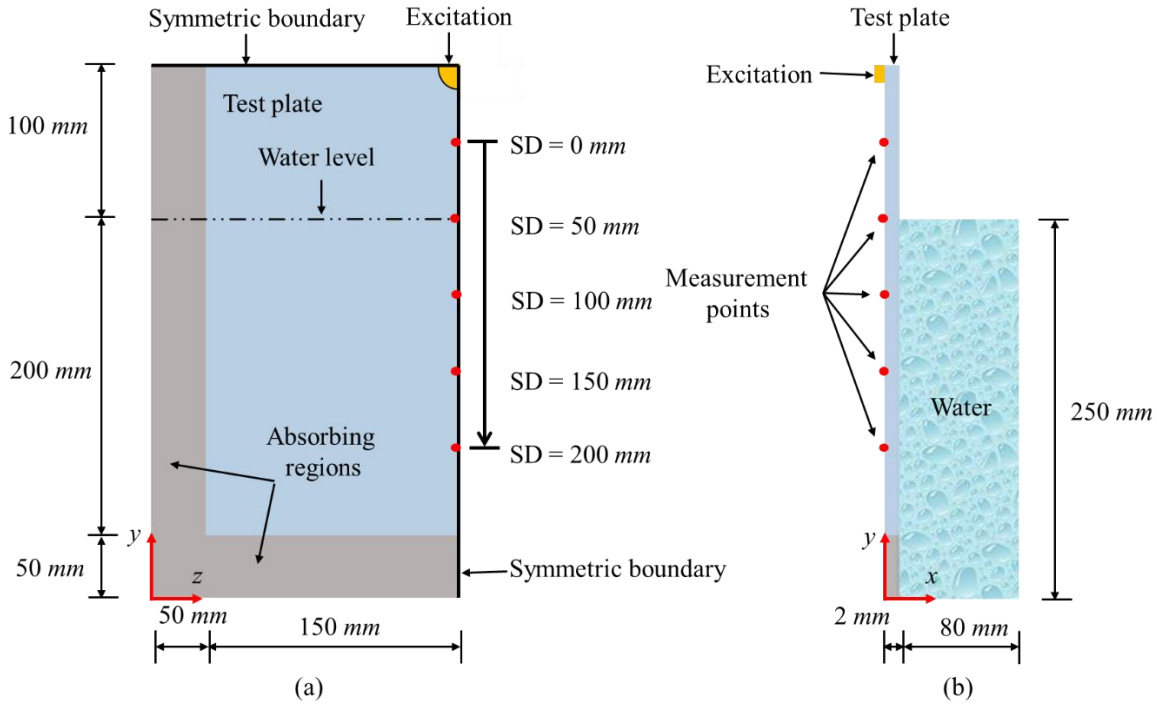

Figure 3.5. Schematic diagram of the 3D FE model for a steel plate with one side partly exposed to water: (a) front view and (b) side view.

A_0 wave was generated by applying the out-of-plane displacements to the plate surface covered by a 5 mm diameter quarter-circle located at the top right corner of the plate [34]. Figure 3.9(b) shows the waveform of the excitation signal, which is a 10-cycle narrowband tone burst. To define the locations of the measurement points, a one-dimensional coordinate, scanning distance (SD), was defined along the right edge of the plate vertically downward as shown in Figure 3.5. The origin (SD = 0 mm) was set at the position of 50 mm below the excitation center. Then, the out-of-plane displacements were collected at five measurement points, which were evenly distributed at 50 mm apart from SD = 0 mm to SD = 200 mm. The other side of the plate was partially in contact with water as shown in Figure 3.5(b). The water level was located at the second measurement point (SD = 50 mm). The thickness of the water layer was chosen to separate the pressure wave reflections from the incident wave signals. The steel plate and the water layer were meshed using 3D eight-node solid elements with reduced integration (C3D8R) and 3D eight-node acoustic elements with reduced integration (AC3D8R), respectively. The fluid and solid interface was simulated by node-surface tie constraints [16, 25]. The element size was set as 0.5 mm, which ensured approximately fifteen elements exist per wavelength of QS wave at 200 kHz. The simulation results were calculated using the central-difference integration by ABAQUS/Explicit [35].

Figure 3.6 presents the snapshots of the simulation results with the excitation frequency of 120 kHz. The color in the water regions denotes the acoustic pressure. At this excitation frequency, a large proportion of the QS wave energy is conserved in the one-side water-immersed plate, of which the deformation is similar to that of A_0 wave in the dry plate as shown in Figures 3.3 and 3.4. When A_0 wave travels from the dry section of the plate into the water-immersed section, part of the wave energy is converted to the pressure waves in the water, and the rest of the wave energy continues to propagate along the water-immersed plate at a speed slightly quicker than the pressure waves in the water. After a short propagation distance in the water-immersed plate, the first wave packet decays slowly and the acoustic field is tethered to the plate-water interface as shown in Figure 3.6(d). These are the typical characteristics of QS wave.

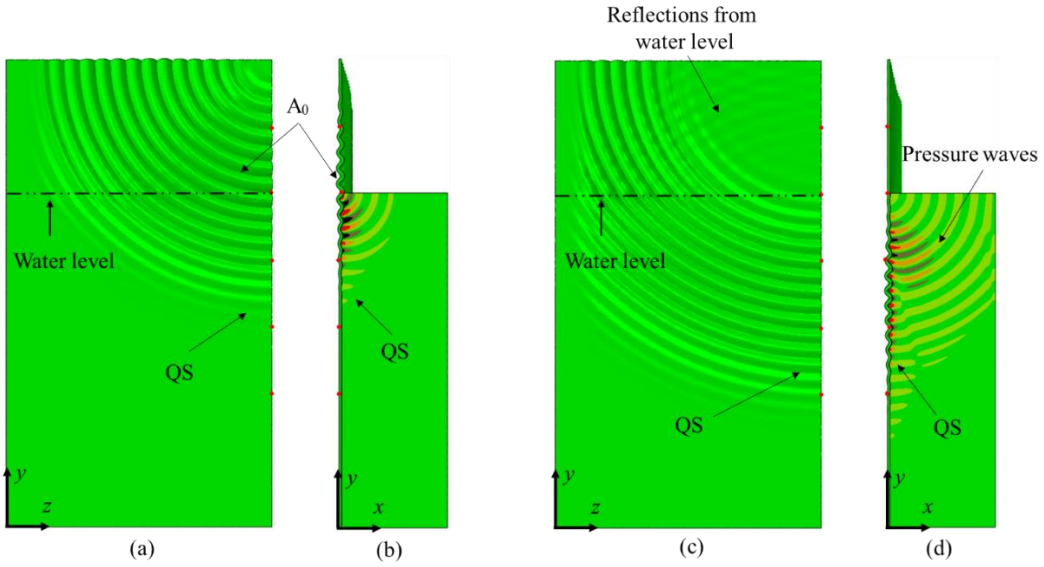

Figure 3.6. Snapshots of the simulation results with the excitation frequency of 120 kHz (a) front view and (b) side view when the guided waves just travel from the dry section of the plate into the water-immersed section; (c) front view and (d) side view after a short propagation distance in the water-immersed plate.

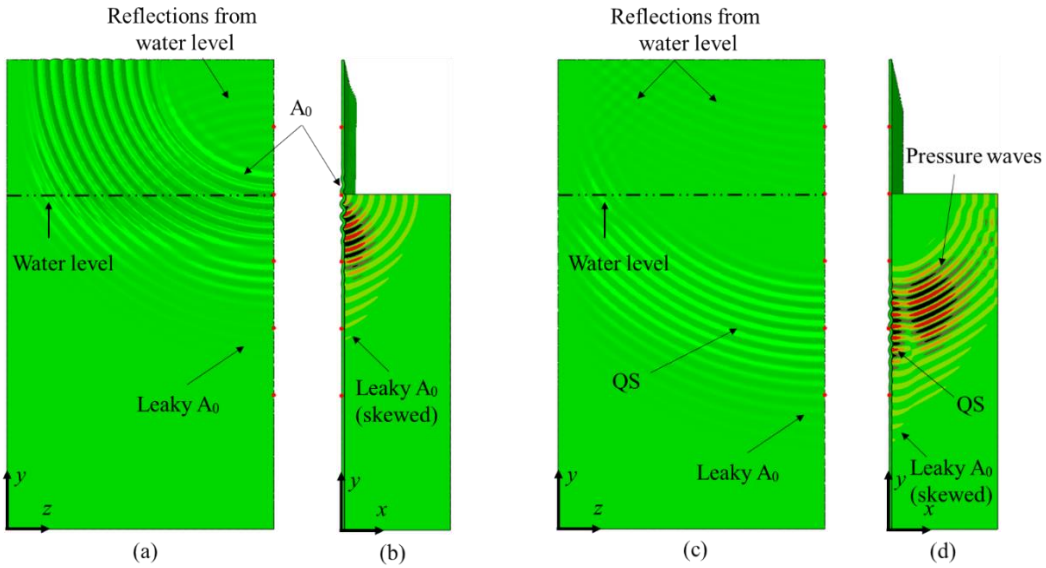

Figure 3.7. Snapshots of the simulation results with the excitation frequency of 170 kHz (a) front view and (b) side view when the guided waves just travel from the dry section of the plate into the water-immersed section; (c) front view and (d) side view after a short propagation distance in the water-immersed plate.

Figure 3.7 shows the snapshots of the simulation results with the excitation frequency of 170 kHz. The mode shape of QS wave at 170 kHz is dominated by the in-plane displacements of water and the deformation of QS wave in the water-immersed plate is no longer similar to that of A_0 wave in the dry plate (see Figures 3.3 and 3.4). The first wave packet in Figure 3.7 continuously radiates wave energy into the surrounding liquid medium, as shown by the skewed acoustic fields (skewed yellow lines) in the water layer in Figures 3.7(b) and 3.7(d). This wave packet with continuous wave energy leakage cannot be detected in Figure 3.6. Following the first wave packet, another wave packet propagates along the immersed plate at a speed slightly quicker than the pressure waves in water. Unlike the first wave packet, the second wave packet propagates with most of the energy confined to the plate-water interface. Based on the propagation speeds and the acoustic pressure in the water, the first and second wave packets in Figure 3.7 are identified as leaky A_0 and QS waves, respectively.

To better observe how the signals change with the propagation distance, Figure 3.8 presents the simulated out-of-plane displacements at the five measurement points that are denoted by the red dots in Figure 3.5. Figures 3.8(a) and 3.8(b) show the time-domain data for the excitation frequencies of 120 kHz and 170 kHz, respectively. Their corresponding frequency spectrums are given in Figures 3.8(c) and 3.8(d), respectively. The amplitudes are normalized by the maximum absolute amplitudes of the signals measured at the first measurement point (SD = 0 mm). It should be noted that when the excitation frequency is 170 kHz, the time-domain signals measured at SD = 100 mm, 150 mm, and 200 mm are so small that they are magnified by a factor of four and shown in Figure 3.8(b). The normalized amplitudes of the signals collected in the immersed section of the plate (SD > 50 mm) significantly decrease with the excitation frequency. In addition, when the excitation frequency is 170 kHz, the simulated signals show apparent frequency shifts in the frequency spectrums. For example, the central frequency of the signal measured at SD = 100 mm, denoted by the orange dash-dot line in Figure 3.8(d), shifts to a frequency slightly higher than the central excitation frequency of 170 kHz. Subsequently, the wave energy shifts to a lower frequency as shown by the signals measured at SD = 150 mm (purple solid line) and SD = 200 mm (yellow solid line) in Figure 3.8(d). The simulation results demonstrate that the guided wave

propagation in the partially water-immersed plate varies significantly with the excitation frequency. The following sections present experimental investigations to validate the simulation results, and the phenomenon of energy shift in the frequency domain due to the presence of water is discussed in detail.

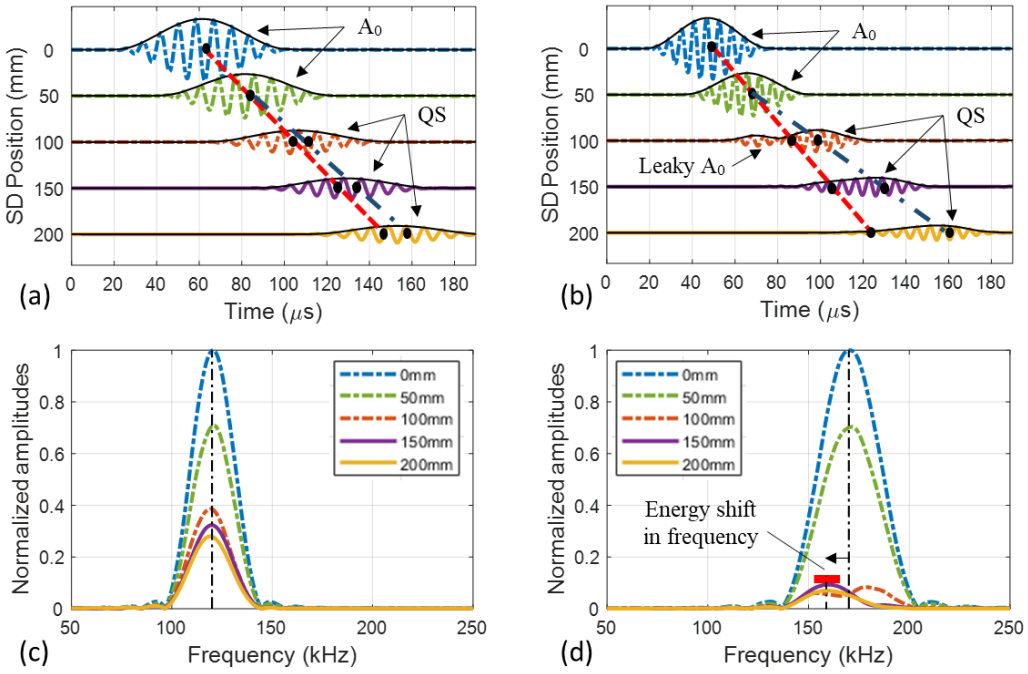

Figure 3.8. Simulated time-domain signals for a steel plate with one side partly exposed to water (the same conditions as Case B presented in the experimental section) with the excitation frequency of (a) 120 kHz and (b) 170 kHz, respectively; (c) and (d) are the frequency spectrums of (a) and (b), respectively (the time-domain signals measured at SD = 100 mm, 150 mm, and 200 mm in Figure 3.8(b) are magnified by a factor of four).

3.5. Experiment setup

Experiments were conducted on a steel tank, of which the front wall was used as the test plate. The test plate was 2 mm thick and made of mild steel. A circular piezoceramic wafer (Ferroperm Pz27, Denmark) was used as the guided wave actuator and it was bonded on the external surface of the test plate as indicated by the PZT transducer in Figure 3.9(a). The diameter and the thickness of the

piezoceramic wafer were 5 mm and 2 mm, respectively. An arbitrary function generator (AFG 2021, China) was used to generate the excitation signal. Figure 3.9(b) gives the waveform of the excitation signal that is a 10-cycle narrowband tone burst. The excitation signal was magnified by a voltage amplifier (Krohn-Hite 7500, USA), and then sent to the piezoceramic wafer transducer.

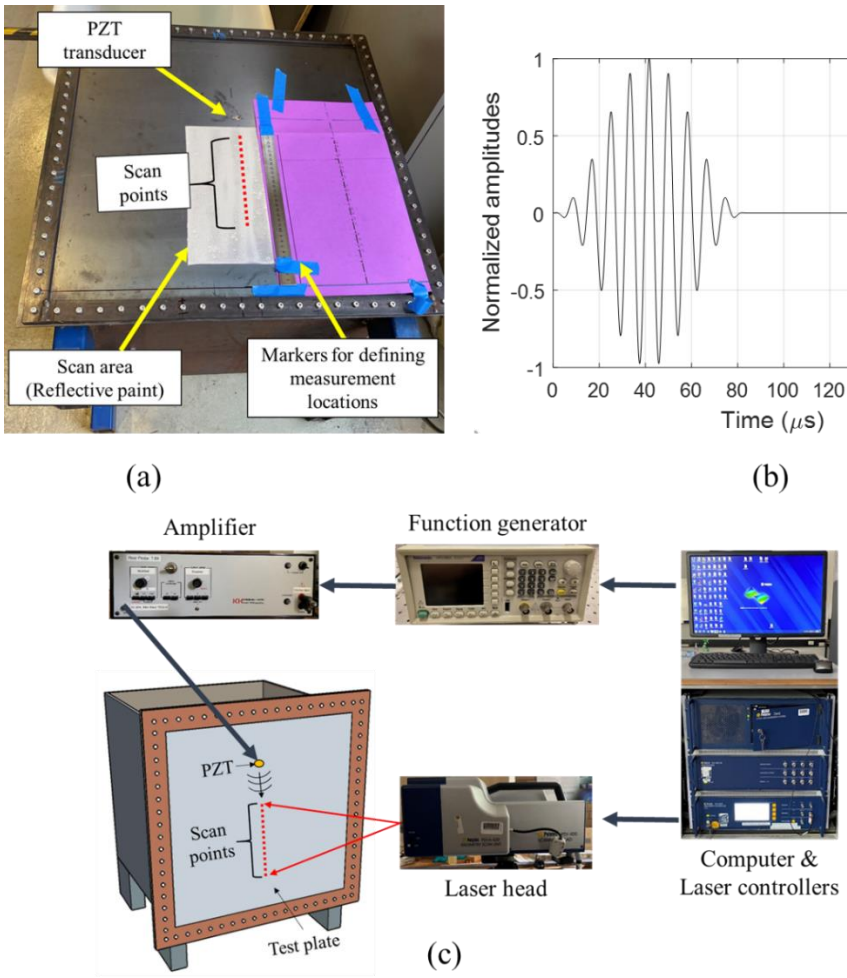

Figure 3.9. (a) A photo of the metal tank, (b) the waveform of the excitation signal, and (c) the experiment setup

An SLDV (Polytec PSV-400-M2-20, Germany) was used to collect the experimental signals. The silver-white paint on the plate surface in Figure 3.9(a) is the reflective paint (CRC, USA) that was sprayed on the scan area to increase the reflection of the laser beam. Next to the scan area, a ruler was placed to assist with

defining measurement points. Then, the out-of-plane displacements were recorded by the SLDV at a sampling rate of 10.24 MHz. Each measurement was improved by averaging the signals with 800 acquisitions and applying a low-pass filter with the cut-off frequency being 1MHz. Figure 3.9(c) shows the schematic diagram of the experiment setup.

Similar to the 3D FE model, a one-dimensional coordinate, SD, was defined on the external surface of the test plate. The origin (SD = 0 mm) was set at the position of 50 mm vertically below the center of the piezoceramic wafer. The experimental study included two parts, which were five-point scan tests and line scan tests, respectively. Firstly, the five-point scan tests were conducted on the steel tank to validate the simulation results. The signals were measured at SD = 0 mm, 50 mm, 100 mm, 150 mm, and 200 mm, which were at the same locations as the simulations as shown in Figure 5.

Then, line scan tests were carried out to visualize guided wave fields on the test plate. The objective of the line scan test was to experimentally demonstrate the interaction of each guided wave mode during the mode conversion process. According to the simulation results shown in Figures 3.6, 3.7, and 3.8, the mode conversion process mainly occurs between SD = 50 mm and SD = 150 mm. After SD = 150 mm, only the QS wave can be detected as shown by the signals measured at SD = 150mm and SD = 200 mm in Figure 3.8. Therefore, the line scan tests focused on the region between SD = 0 mm and SD = 150 mm as shown in Figure 3.10(a). The signals were collected at 127 measurement points, which were evenly distributed along the scan line from SD = 0 mm to SD = 150 mm. With these measurements, the time-space wave fields could be constructed by plotting the amplitudes of the measured signals versus time and SD.

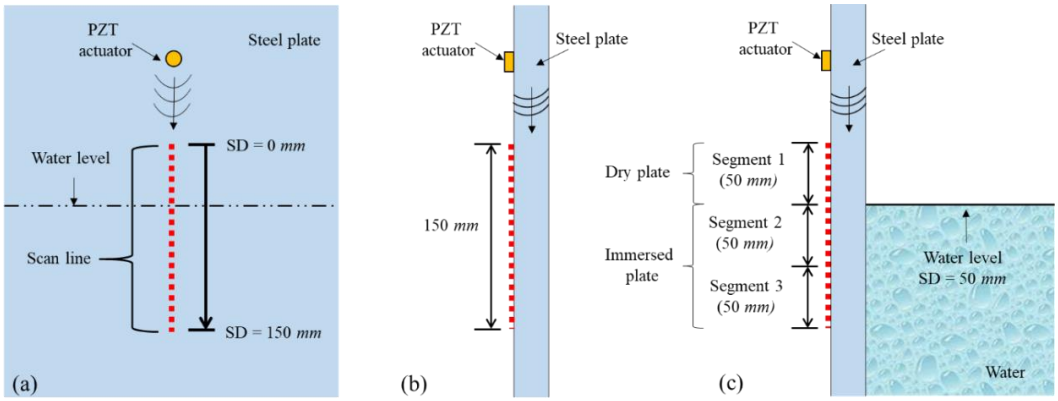

Figure 3.10. Schematic diagram of the scan line on the test plate (a) front view; (b) side view of Case A (empty tank); (c) side view of Case B (partially water-filled tank).

In order to demonstrate the influence of water on the guided wave propagation, both the five-point scan tests and line scan tests were carried out on the empty tank (Case A) and the partially water-filled tank (Case B), respectively. Figures 3.10(b) and 3.10(c) show the side view of the scan line on the test plate for Case A and Case B, respectively. In Case B, the steel tank was partially filled with water with the water level set at SD = 50 mm. Therefore, one-third of the scan line was located in the non-immersed section of the plate (from SD = 0 mm to SD = 50 mm), called “dry plate”, and the rest of the scan line was located in the section of the one-side water-immersed plate (from SD = 50 mm to SD = 150 mm), which was denoted as “immersed plate”. Guided waves were generated on the test plate by the piezoceramic wafer located at 100 mm above the water level. The time-space wave fields were captured before and after guided waves traveled from the dry plate into the immersed plate.

3.6. Experimental results and analysis

3.6.1. Validation of numerical simulations

This section presents the experimental measurements to validate the accuracy of the 3D FE model. Figure 3.11 presents the experimental results with the central excitation frequency of 120 kHz. Figures 3.11(a) and 3.11(b) show the time-space

wave fields for the empty tank and the partially water-filled tank, respectively. The amplitudes are normalized by the maximum absolute amplitudes of the signals measured at the first scan point (SD = 0 mm). The black dashed line in Figure 3.11(b) denotes the water level located at SD = 50 mm. The generated guided wave fields in the dry section of the plate (between SD = 0 mm and SD = 50 mm) are similar for both the empty tank in Figure 3.11(a) and the partially water-filled tank in Figure 3.11(b). However, the amplitudes of the signals measured in the immersed plate (SD > 50 mm) of the partially water-filled tank in Figure 3.11(b) are smaller than their counterparts in the empty tank in Figure 3.11(a). This indicates that part of the wave energy leaks from the immersed plate into the water as shown in the snapshots of the simulation results (see Figures 3.6(a) and 3.6(b)).

Figures 3.11(c) and 3.11(d) show typical examples of the signals measured at SD = 0 mm, 50 mm, 100 mm, 150 mm, and 200 mm for the empty tank and the partially water-filled tank, respectively. The wave speed in the immersed plate of the partially water-filled tank, as denoted by the dark blue dash-dot line in Figure 3.11(b), is slightly slower than the wave speed in the dry plate that is marked by the red dashed line. From the wave speed evaluation, the wave packets measured from the empty tank in Figure 3.11(a) and the dry section of the partially water-filled tank in Figure 3.11(b) are identified as A_0 wave [24]. S_0 wave can be not observed because it has negligible out-of-plane motions at the selected excitation frequency [25, 36]. The changes of the wave speed and amplitude in the immersed section of the test plate demonstrate that A_0 wave is mode converted to QS wave. Figures 3.11(e) and 3.11(f) present the frequency spectrums of Figures 3.11 (c) and 3.11(d), respectively. The amplitudes are normalized by the signal measured at the first scan point (SD = 0 mm). The peaks of all measured signals are concentrated around the central frequency of the excitation signal of 120 kHz. There is a good agreement between the experimental measurements shown in Figures 3.11 (d) and 3.11(f) and the simulation results (see Figures 3.8(a) and 3.8(c)).

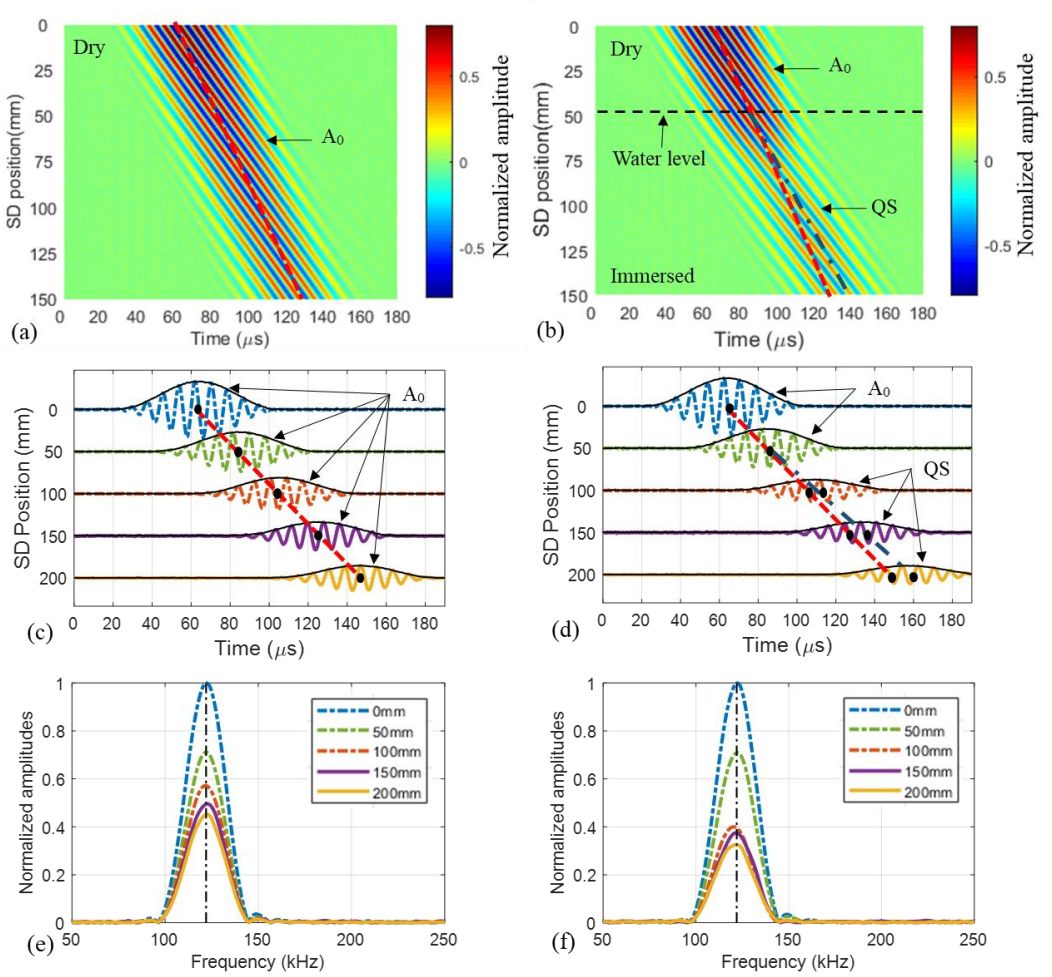

Figure 3.11. Experimental results with the excitation frequency of 120 kHz: (a) and (b) are time-space wave fields for the empty tank and the partially water-filled tank, respectively; (c) and (d) are typical examples of the time-domain signals for the empty tank and the partially water-filled tank, respectively; (e) and (f) are the frequency spectrums of (c) and (d), respectively.

For comparison, Figure 3.12 presents the experimental results with the central excitation frequency of 170 kHz. Figures 3.12(a) and 3.12(b) present the time-space wave fields for the empty tank and the partially water-filled tank, respectively. For the empty tank, the waves propagate at a consistent speed as represented by the red dashed line in Figure 3.12(a). The same wave fields are observed in the dry section of the plate (SD < 50 mm) of the partially water-filled tank as shown in Figure 3.12(b). However, when guided waves propagate into the water-immersed section (SD > 50 mm), the wave amplitudes decrease rapidly and

reach the minimum between SD = 80 mm and SD = 90 mm as indicated in Figure 3.12(b). After that, the waves slightly increase in amplitude near the position of SD = 100 mm, and then continue to propagate at a speed (dark blue dash-dot line) that is much slower than the original speed of the waves in the dry plate (red dashed line).

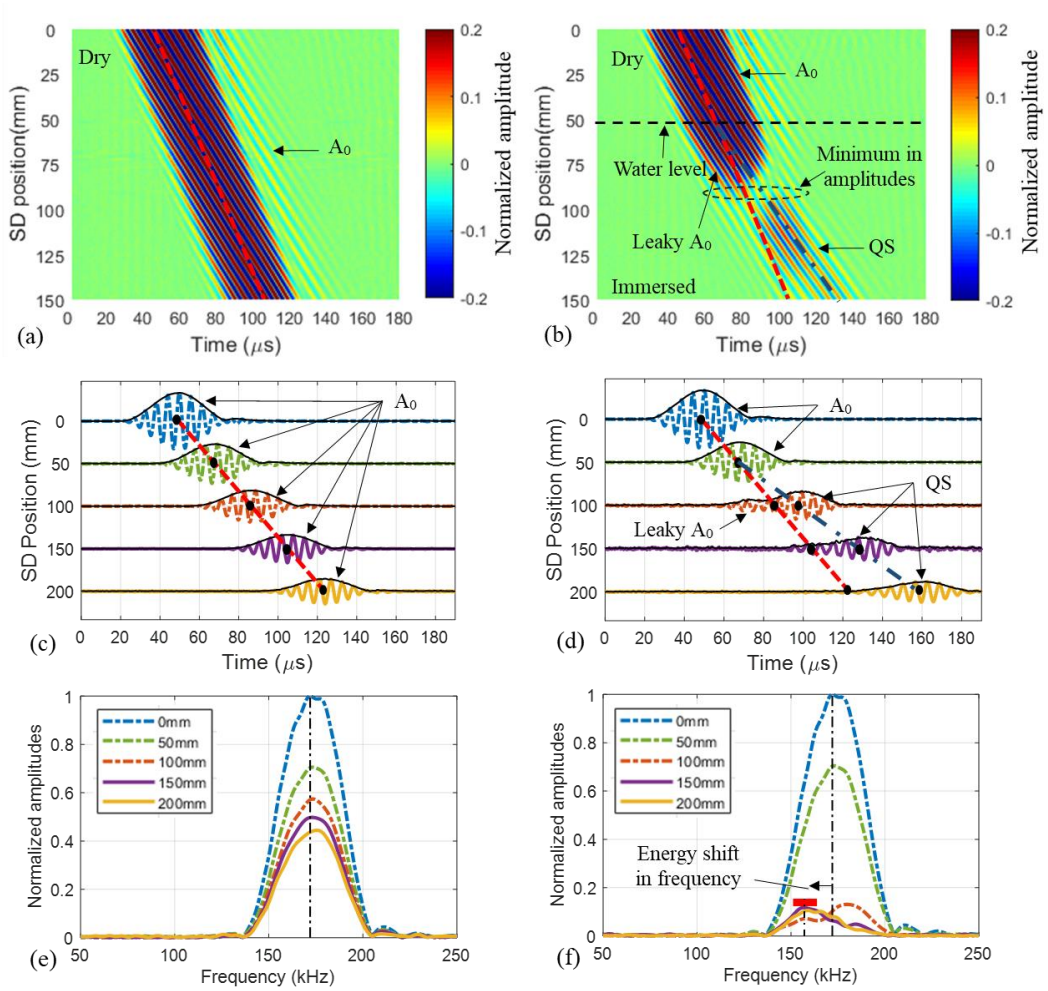

Figure 3.12. Experimental results with the excitation frequency of 170 kHz: (a) and (b) are time-space wave fields for the empty tank and the partially water-filled tank, respectively; (c) and (d) are typical examples of the time-domain signals for the empty tank and the partially water-filled tank, respectively; (e) and (f) are the frequency spectrums of (c) and (d), respectively (the time-domain signals measured at SD = 100 mm, 150 mm, and 200 mm in Figure 3.12(d) are magnified by a factor of four).

Figures 3.12(c) and 3.12(d) show typical time-domain signals measured at SD = 0 mm, 50 mm, 100 mm, 150 mm, and 200 mm for the empty tank and the partially water-filled tank, respectively. To provide better observation, the signals measured from the partially water-filled tank at SD = 100 mm, 150 mm, and 200 mm are magnified by a factor of four and shown in Figure 3.12(d). Guided waves propagate as a single wave packet along the dry section of the plate (between SD = 0 mm and SD = 50 mm). However, after a short propagation distance in the immersed plate, the signal measured at SD = 100 mm shows two wave packets, each propagating at different speeds. It should be noted that the mode split phenomenon is not observed on the water-immersed plate with the central excitation frequency of 120 kHz (see Figure 3.11(d)). The first wave packet decays quickly and disappears as shown by the signal measured at SD = 150 mm in Figure 3.12(d), while the second wave packet propagates with low attenuation at a slower wave speed (dark blue dash-dot line). Figures 3.12(e) and 3.12(f) show the frequency spectrums of Figures 3.12(c) and 3.12 (d), respectively. The signals measured at SD = 100 mm, 150 mm, and 200 mm from the partially water-filled tank in Figures 3.12(f) have much smaller amplitudes than their counterparts from the empty tank in Figures 3.12(e). In addition, Figure 3.12(f) displays the energy shift in frequency, which has a good agreement with the simulation results (see Figure 3.8(d)). It is confirmed that the energy shift in the frequency domain is due to the presence of water because this phenomenon does not occur in the case of the empty tank as shown in Figure 3.12(e).

To further investigate the accuracy of the 3D FE model, Figure 3.13 compares the peak amplitudes of the simulated and experimentally measured signals in the frequency domain for both the empty tank (Case A) and the partially water-filled tank (Case B), respectively. The magnitudes are normalized by their corresponding peak amplitudes of the signals measured at SD = 0 mm. Figures 3.13(a) and 3.13 (b) present the results with the excitation frequency of 120 kHz and 170 kHz, respectively. In the dry section of the plate (SD < 50 mm), the amplitudes of the simulated and experimentally measured signals are identical for both cases. When guided waves just pass the water level (from SD = 50 mm to SD = 100 mm), the measured signals of Case A decrease slowly and smoothly, but the signal amplitudes of Case B drop substantially. After SD = 100 mm, the guided

wave amplitudes in both Case A and Case B decrease slowly with distance. When the excitation frequency increases from 120 kHz to 170 kHz, the amplitudes of the signals of Case A do not show obvious changes as shown by the red hexagons and circles in Figure 3.13. However, the amplitudes of the signals of Case B significantly decrease when the excitation frequency increases. In general, the proposed 3D FE model well predicts the frequency shift phenomena and wave attenuation characteristics and hence, the simulation results are validated to interpret the experimental data.

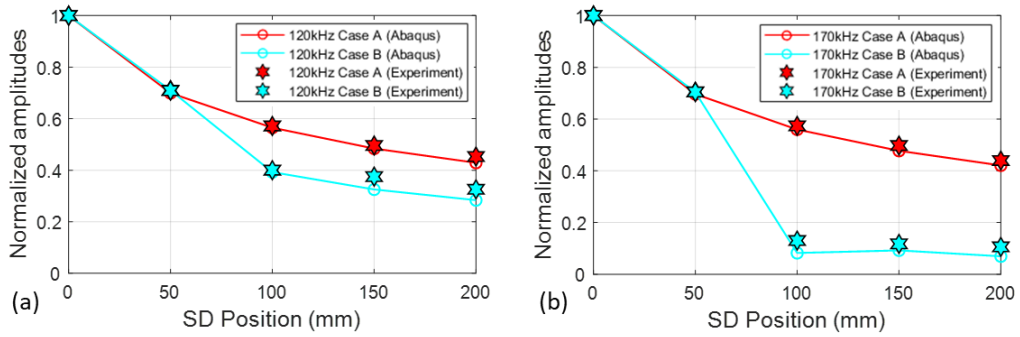

Figure 3.13. Normalized amplitudes of the simulated and experimentally measured signals in the frequency domain for the empty tank (Case A) and the partially water-filled tank (Case B) with the excitation frequency of (a) 120 kHz and (b) 170 kHz, respectively.

3.6.2. Segmented frequency wavenumber analysis

Although the time-space analysis displays the variation of wave amplitudes with the time and propagation distance, it cannot determine the wave mode conversion characteristics such as mode identities and their corresponding frequency components. To graphically demonstrate the mode conversion process, 2D FT is employed to identify the mode information of the experimental data collected along the scan line on the partially water-filled tank (Case B). The scan line is divided into three segments, each of which is 50 mm long and comprises 43 measurement points as shown in Figure 3.10(c). The generated guided waves first propagate through Segment 1 (Dry plate) and then to Segment 2 (Water-immersed plate) and

finally to Segment 3 (Water-immersed plate). The water level is between Segment 1 and 2. The time-space data of each segment is converted to the frequency-wavenumber spectrum through 2D FT, which is defined as:

$$\mathbf{u}(k, f) = \int\int \mathbf{u}(x,t) e^{-i(2\pi ft - kx)} dt dx \tag{3.1}$$

where $\mathbf{u}(k, f)$ and $\mathbf{u}(x,t)$ are the data in the frequency-wavenumber domain and time-space domain, respectively. k and f denote the wavenumber and frequency, respectively. x and t represent the space and time coordinate, respectively.

Figures 3.14(a)-3.14(c) present the experimentally measured data in the time-space domain for the three segments and their corresponding frequency-wavenumber spectrums are given in Figures 3.14(d)-3.14(f), respectively. The excitation frequency is 120 kHz. The color in the frequency-wavenumber spectrums denotes the wave energy of the experimentally measured signals, which is calculated by 2D FT. The black solid lines are the theoretical wavenumber dispersion curves of A_0, S_0, and QS waves calculated by DISPERSE. As mentioned in Section 3.3, the wavenumber dispersion curves of leaky A_0 and leaky S_0 waves overlap with A_0 and S_0 waves. For convenience, leaky A_0 and leaky S_0 waves are labeled as A_0 and S_0 in the figures, respectively. In Segment 1, where the plate is not immersed in water, only the energy of A_0 wave is identified in the frequency-wavenumber spectrum as shown in Figure 3.14(d). The energy of S_0 wave is absent because it has negligible out-of-plane displacements [25, 36]. Next, the wave energy is converted from A_0 wave to QS wave immediately in Segment 2 as shown in Figure 3.14(e). The mode conversion occurs rapidly and the energy of QS wave decays slowly with distance and dominates the frequency-wavenumber spectrums of Segments 2 and 3. At this excitation frequency, leaky A_0 wave is not detected and the energy shift in frequency is not observed.

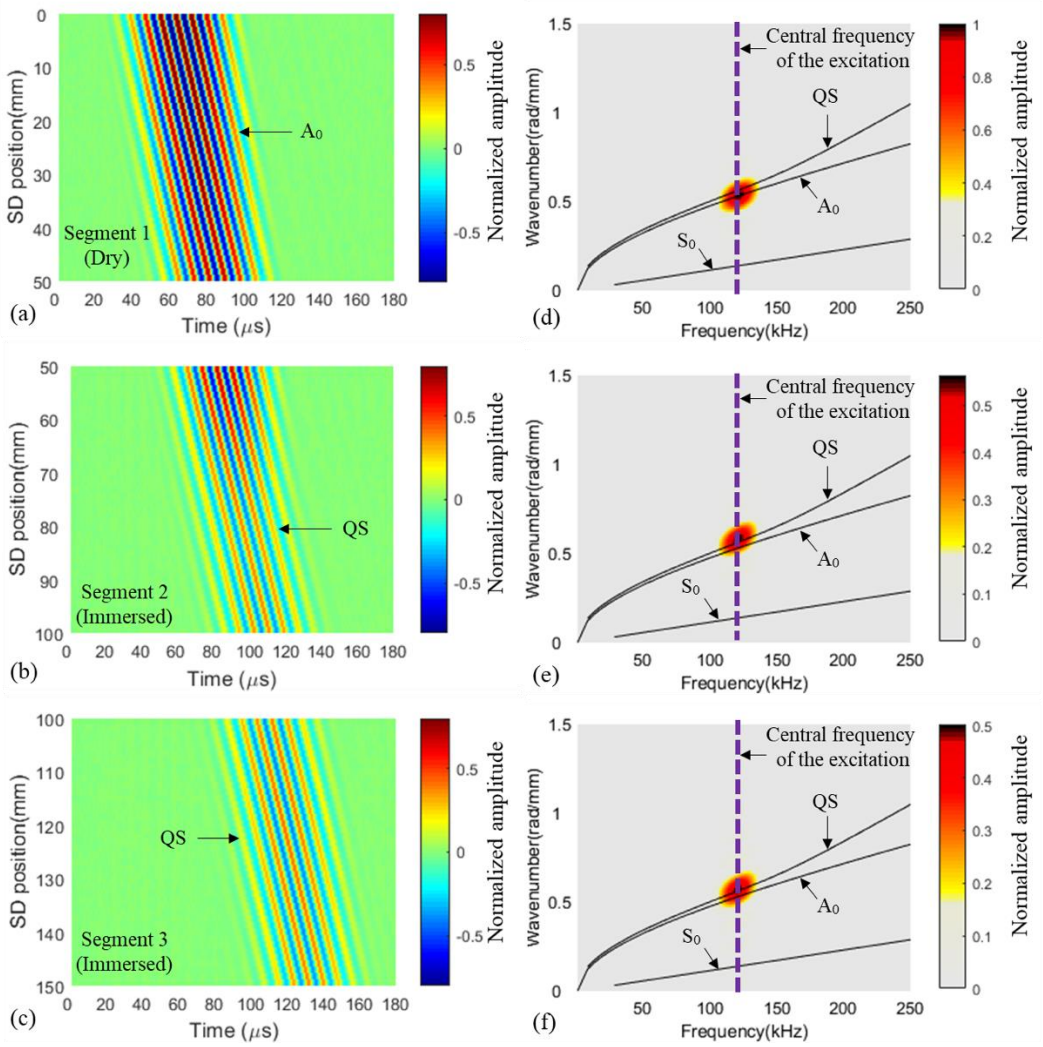

Figure 3.14. Experimental results for the partially water-filled tank with the central excitation frequency of 120 kHz: time-space wave fields for (a) Segment 1, (b) Segment 2, and (c) Segment 3, respectively; frequency wavenumber spectrums for (d) Segment 1, (e) Segment 2, and (f) Segment 3, respectively.

The measured data with the central excitation frequency of 170 kHz is shown in Figure 3.15. Only A_0 wave is identified in Segment 1 as shown in Figures 3.15(a) and 3.15(d). When A_0 wave just propagates into the water-immersed plate, most of the wave energy is converted to leaky A_0 wave that has the same wavenumber as A_0 wave as shown in Figures 3.15(b) and 3.15(e). The signals measured between SD = 50 mm and SD = 80 mm are dominated by leaky A_0 wave whose amplitude decays rapidly. In the meantime, QS wave is also generated as the

amplitude slowly increases with propagation distance until leaky A_0 wave nearly disappears at the end of Segment 2. Leaky A_0 wave and QS wave have different wavenumbers and phase velocities (see Figure 3.2). Therefore, The minimum wave amplitudes between SD = 80 mm and SD = 90 mm can be caused by the destructive interference between the QS wave and leaky A_0 wave.

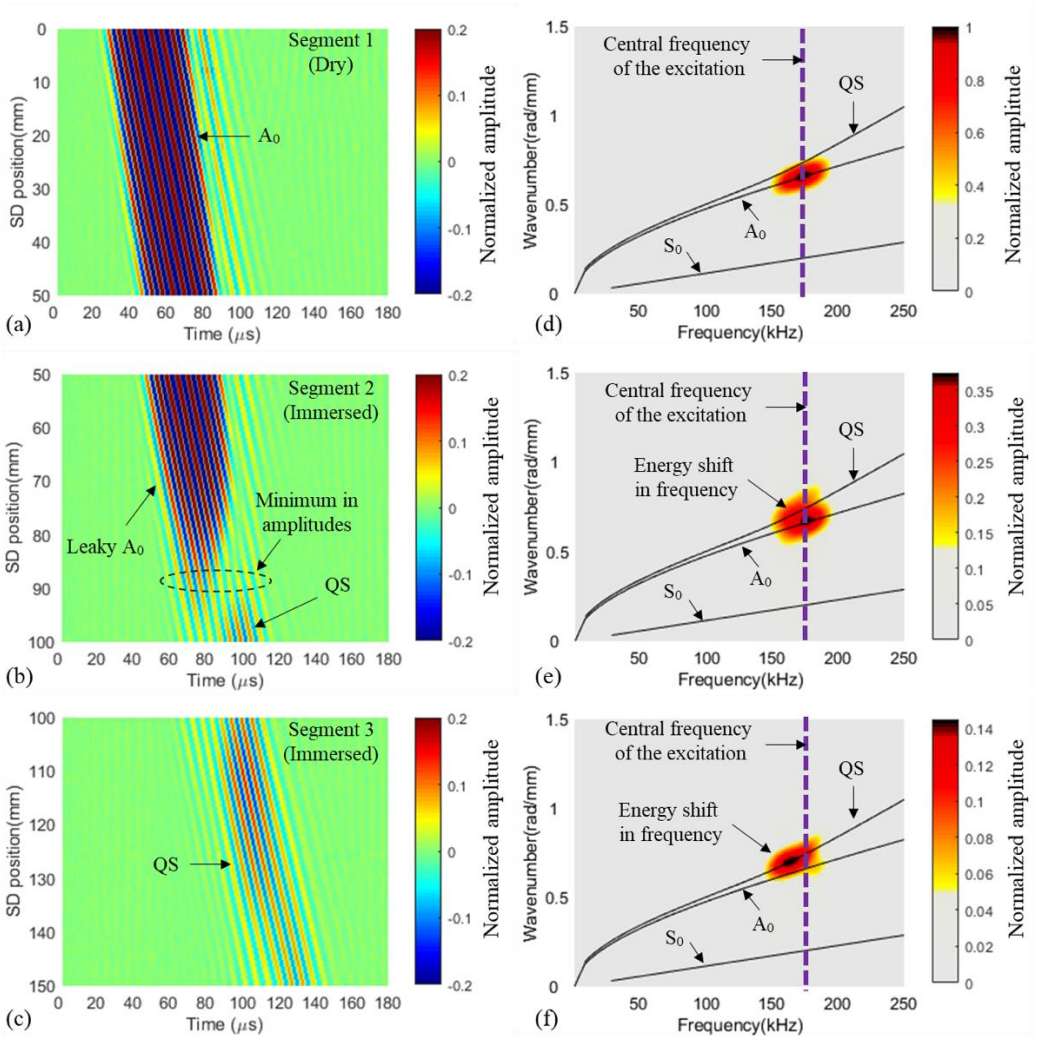

Figure 3.15. Experimental results for the partially water-filled tank with the central excitation frequency of 170 kHz: time-space wave fields for (a) Segment 1, (b) Segment 2, and (c) Segment 3, respectively; frequency wavenumber spectrums for (d) Segment 1, (e) Segment 2, and (f) Segment 3, respectively.

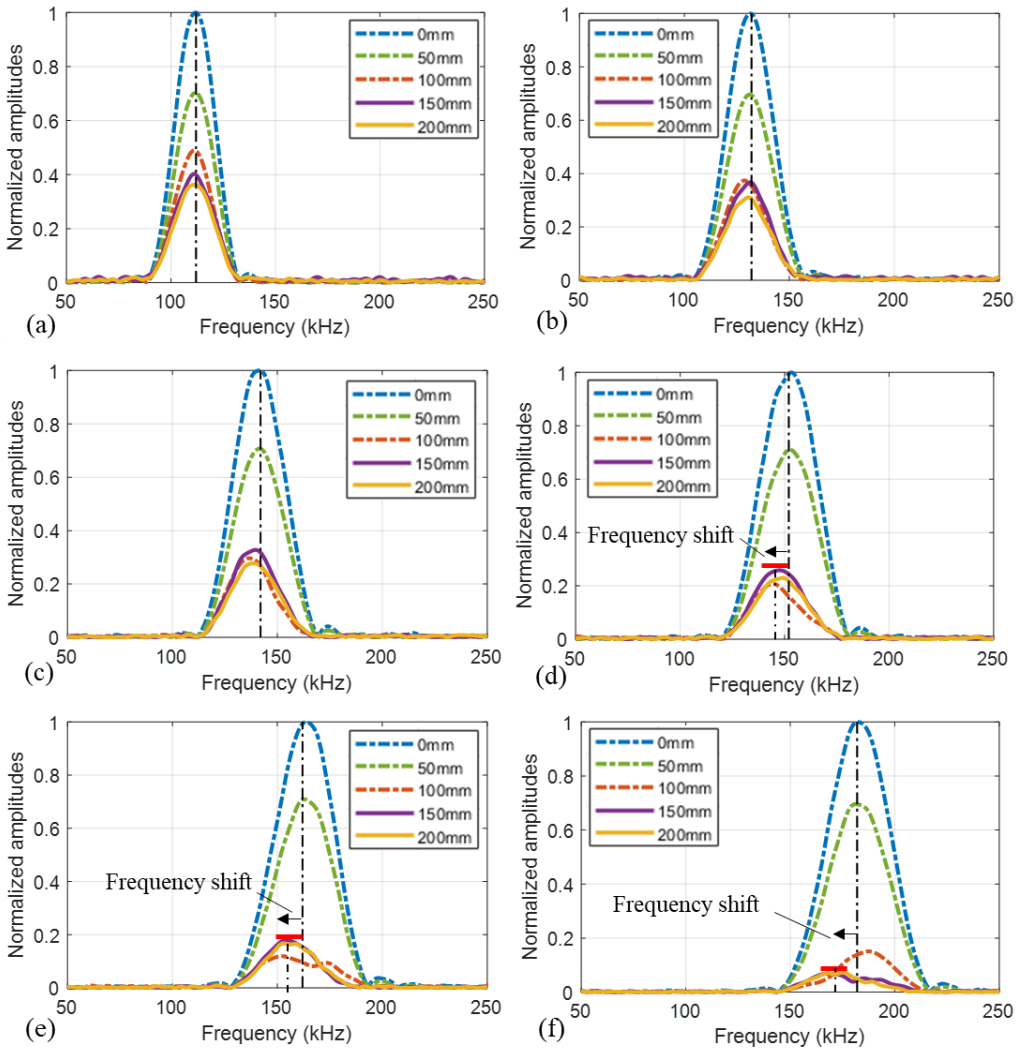

Figure 3.16. Frequency spectrums of the signals experimentally measured from the partially water-filled tank with the excitation frequency of (a) 110 kHz; (b) 130 kHz; (c) 140 kHz; (d) 150 kHz; (e) 160 kHz; and (f) 180 kHz.

After that, the wave fields in Segment 3 are dominated by only QS wave (see Figures 3.15(c) and 3.15(f)). The energy of the mode converted QS wave concentrates at a frequency slightly lower than the central excitation frequency of 170 kHz, which agrees well with Figures 3.8(d) and 3.12(f). Therefore, conclusions can be drawn that at the intersection between the dry plate and immersed plate, A_0 wave is mode converted to both QS wave and leaky A_0 wave with more energy transferred to the latter. Leaky A_0 wave that has mostly out-of-plane displacements in the plate continuously radiates compressional waves in the liquid and also excites

QS wave. Considering that the deformation in the immersed plate of QS wave at low frequencies is greater than that at high frequencies (see Figure 3.4), the anti-symmetrical excitation of leaky A_0 wave is more likely to produce QS wave at lower frequencies. This can be also manifested by the frequency spectrums (see Figures 3.8(d) and 3.12(f)) where the wave energy is progressively transferred from a higher frequency at SD = 100 mm to a frequency lower than the central excitation frequency at SD = 150 mm. After that, the wave energy is conserved at the frequency (lower than the excitation frequency of 170 kHz) and propagates with small attenuation.

3.6.3. Further study by sweeping the excitation frequency

To further investigate the phenomenon of energy shift in the frequency domain, the five-point scan tests were conducted on the partially water-filled tank using the excitation signals with the central frequencies of 110 kHz, 130 kHz, 140 kHz, 150 kHz, 160 kHz, and 180 kHz. The collected signals were transformed to the frequency domain and shown in Figure 3.16. The amplitudes were normalized by the signals measured at the first scan point (SD = 0 mm). As it is confirmed from the segmented frequency wavenumber plots (see Figures 3.14 and 3.15), the signals measured at SD = 150 mm to 200 mm, denoted by the purple and yellow solid lines in Figures 3.11(f), 3.12(f), and 3.16, are dominated by the low-attenuation QS wave. Therefore, it can be concluded that the normalized amplitude of QS wave converted by A_0 wave decreases when the excitation frequency increases.

For excitation frequencies below 140 kHz, the signals measured from both the dry section and water-immersed section of the plate are concentrated around the central excitation frequency (see Figure 3.11(f) and Figures 3.16(a)-3.16(c)). The energy shift in frequency can be observed for excitation frequencies over 150 kHz, where leaky A_0 wave appears as the phase velocity of the incident A_0 wave becomes larger than the sound speed of the surrounding water. Under the central excitation frequency of 150 kHz and 160 kHz, the signals measured at SD = 100 mm, 150 mm, and SD = 200 mm have most of their wave energy concentrated at a frequency lower than the central excitation frequency (see Figures 3.16(d) and 3.16(e)). The range of the frequency shift also increases when the central excitation frequency

increases. However, the signals measured at SD = 100 mm under the central excitation frequency of 170 kHz and 180 kHz are shown to have more energy conserved at higher frequencies (see Figures 3.12(f) and 3.16(f)). This is because the amplitudes of QS wave converted by A_0 wave are so small that leaky A_0 wave can be detected clearly at this measurement point. Leaky A_0 wave at higher frequencies decays more slowly than that at lower frequencies as discussed in Section 3.3, making the central frequency of the signal shift to a relatively higher frequency. However, leaky A_0 wave completely disappears after a short propagation distance, and only the QS wave can be detected at SD =150 mm and SD = 200 mm, as shown in Figure 3.15. Since the low-attenuation QS wave at lower frequencies has a larger deformation fraction in the immersed plate, the measured signals from the surface of the immersed plate eventually concentrate at a frequency lower than the central excitation frequency. The next section summarizes the frequency dependence of the mode conversion from A_0 wave to QS wave and further explains the mechanism of the frequency shift phenomena.

3.7. Discussion and application

3.7.1. The influence of excitation frequency on the mode conversion process

The mode conversion from A_0 wave to QS wave has been numerically and experimentally shown to be dependent on the excitation frequency. The frequency dependence is summarized in this section and analyzed according to the dispersion behaviors of the guided waves. The theoretical dispersion curves and mode shapes of guided waves have been derived from the global matrix theory and are present in Section 3.3. In the following discussion, the term “high frequency” means the frequency range, in which the phase velocity of the incident A_0 wave is larger than the sound speed of the surrounding liquid medium and the leaky A_0 wave appears. The term “low frequency” indicates the frequency range, in which the phase velocity of the incident A_0 wave is smaller than the sound speed of the surrounding liquid medium and the quasi-Scholte wave is dispersive. The transition frequency between the high and low frequency ranges can be estimated from the phase velocity dispersion curves. For example, the phase velocity of A_0 wave for a metallic plate monotonically increases with frequency until it reaches the Rayleigh

wave speed, which is around 3000 m/s for steel. The sound speed of water is around 1500 m/s, which is constant for all frequencies. Therefore, the transition frequency is around 150 kHz, at which the phase velocity of A_0 wave traveling along the 2 mm thick steel plate is around 1500 m/s, as shown in Figure 3.2(a). The phase velocity dispersion curves can be calculated by the commercial software DISPERSE. The input data includes the material properties of the plate, the plate thickness, and the sound speed of the surrounding liquid medium.

At low frequencies, the difference in wavenumber between A_0 wave and QS wave is small. In addition, the deformation of QS wave in the immersed plate is similar to that of A_0 wave in the dry plate (see Figures 3.3 and 3.4). Thus, A_0 wave can be mode converted to QS wave rapidly with most of the wave energy conserved in the plate. When the excitation frequency increases, the energy distribution of QS wave in the immersed plate decreases sharply and the similarity reduces between A_0 and QS waves (see the dispersion curves in Figure 3.2 and mode shapes diagrams in Figures 3.3 and 3.4). Therefore, the amplitude of QS wave converted by A_0 wave significantly decreases with frequency.

At high frequencies, leaky A_0 wave appears when the phase velocity of the incident A_0 wave becomes larger than the sound speed of the water. A_0 wave is mode converted to both QS wave and leaky A_0 wave with more energy transferred to the latter. Leaky A_0 wave that has the flexural mode shape in the plate continuously radiates compressional waves in the liquid and also excites QS wave. After a short propagation distance, leaky A_0 wave decays quickly and disappears so that only QS wave can be detected.

3.7.2. The mechanism of the energy shift in frequency phenomenon

The energy shift in frequency occurs during the mode conversion process when the incident A_0 wave is generated at high frequencies. The mechanism of the energy shift in frequency phenomenon can be explained by the dispersion curves and the mode shapes of guided wave modes as follows.

Firstly, the central frequency of the signal can shift to a frequency higher than the center frequency of the excitation, when the wave fields are dominated by

the leaky A_0 wave (see signals at SD = 100 mm in Figures 3.12(f) and 3.16(f)). This is due to the fact that the attenuation dispersion curve of leaky A_0 wave declines sharply in the selected frequency region (see Figure 3.2). The low-frequency components of leaky A_0 wave decay much quicker than the high-frequency components. Therefore, leaky A_0 wave at high frequencies can travel longer distances, making the central frequency of the signals measured in the immersed plate near the water level relatively higher than the central excitation frequency.

Secondly, the central frequency of the mode converted QS wave is relatively lower than the central frequency of the excitation. One reason is that the deformation in the immersed plate of QS wave at low frequencies has a flexural mode shape, which is similar to A_0 wave in the dry plate. But the similarity between QS and A_0 waves reduces with frequency. This makes the mode conversion from A_0 wave to QS wave (at the intersection of the dry plate and the water-immersed plate) much easier at low frequencies than that at high frequencies, with more energy transferred and conserved in the plate. The other reason is that the deformation of QS wave in the plate is rapidly reduced with frequency (see Figure 3.4). Thus, QS wave at low frequencies can be excited on the plate more easily by the out-of-plane motions of leaky A_0 wave after guided waves propagate into the water-immersed plate. Since the generated QS wave has low attenuation, the measured signals in the immersed plate eventually shift to a frequency lower than the central excitation frequency (see signals at SD = 150 mm and SD = 200 mm in Figure 3.12(f) and Figures 3.16(d)-3.16(f)).

3.7.3. Implications for practical applications

The findings of the present study suggest that the low-attenuation QS wave can be easily excited by mode conversion from A_0 wave that is generated at low frequencies on the dry plate section. This phenomenon can be employed to detect damage for the plate structures that are partially immersed in liquid, such as partially water-filled tanks and pipelines. These structures generally experience uniform corrosion and pitting corrosion. The latter is more critical because it damages the deep structures with little loss of metal [37].

Previous studies have characterized corrosion damage using A_0 wave for plates surrounded by air [38-40] and QS wave for plates in contact with liquid [21, 41]. For partially immersed plates, it is also possible to evaluate the defects by sending A_0 waves on the dry section of the plate and measuring the QS wave signals on the immersed section. This method is very promising for long-range inspection because QS wave does not radiate energy in the liquid (see Figures 3.6 and 3.7) and is able to travel along the plate-fluid interface with low attenuation. The measurement range through using the dispersive QS wave by mode conversion from A_0 wave can be of the order of several meters based on the low attenuation characteristics as shown in Figure 3.13. However, the actual propagation distance is dependent on the material properties of the plate and the surrounding liquid medium as well as the excitation frequency. As discussed in Section 3.7.1, the lower the excitation frequency, the more wave energy conserved in the plate during the mode conversion process, and therefore the longer the propagation distance. Another advantage is that this method has the potential to characterize the structural defects entirely based on the QS wave, which is appealing for accurate detection and imaging of the defects [42]. After a short propagation distance, leaky A_0 wave decays quickly and disappears due to high attenuation. The low-attenuation QS wave can be well separated from the leaky S_0 wave, of which the propagation speed is three times that of QS wave (see Figure 3.2(b)). Although leaky S_0 wave has low attenuation, it is not sensitive enough to identify small and shallow corrosion damage in the early stage [43-45]. In contrast, the QS wave has the shortest wavelength at a given frequency and provides better sensitivity than the leaky S_0 wave to shallow hidden corrosion pits in immersed plates [41].

It should be noted that the damage detection algorithm for the partially immersed structures should consider the change of wave behaviors due to the mode conversion phenomenon and the presence of liquid. It is recommended to select an excitation frequency below the transition frequency, at which the proposed phenomenon of guided wave energy shift in frequency can be avoided. (see Figures 3.11 and 3.14). Otherwise, the effect of the potential wave energy shift in the frequency domain should also be carefully considered and compensated. For instance, it is observed in the present study that the wave energy of the mode converted QS wave in the immersed plate moves to a frequency below the central

excitation frequency, making the actual wavenumber of the QS wave smaller than that at the central excitation frequency (see Figure 3.15(f)). This also indicates a smaller phase velocity, a higher group velocity, and a larger wavelength (see Figure 3.2). The change of the propagation characteristics of guided waves will affect the performance of conventional damage detection and imagining algorithms [16, 46].

The mode conversion between QS and A_0 waves in partially immersed plates was widely used for liquid-level assessing [22, 24, 47] and fluid-property sensing [18, 48, 49]. The behaviors of A_0 wave depend on the geometry and material properties of the plate, while QS wave reflects the properties of both the plate and the surrounding fluid medium. Generally, the difference between QS and A_0 waves becomes larger with frequency. Therefore, increasing the excitation frequency can result in larger deviations in the signals measured from the partially immersed plate in terms of the time of arrival, amplitude, and phase angle, and hence, it can potentially increase the sensitivity of the signals to the variation of liquid level and fluid properties. However, the results of the present study show that the amplitude of the QS wave converted by A_0 wave significantly decreases with frequency. Therefore, the optimal excitation frequency is a trade-off between the sensitivity and the amplitudes of the measured signals. For simplicity, it is also recommended to excite the guided waves at a low frequency to ensure that the phase velocity of the incident A_0 wave is smaller than the sound speed of the surrounding liquid medium. Without the interference of the leaky A_0 wave, the mode conversion process is simple and the frequency shift phenomena can be avoided.

Lastly, QS wave at high excitation frequencies becomes nondispersive and is promising for fluid manipulation [20] and removing diffusion boundary layer [19, 50], where the focus is directed on the movement of the fluid particles and the deformation in the plate is not interested. The low-attenuation QS wave with most of the wave energy concentrated at the plate-fluid interface has the potential to cover a large area of the fluid near the plate surface. However, attention should be paid to the potential frequency shift of the measured signals. As shown in Figures 3.15 and 3.16, guided wave energy can shift in the frequency domain during the mode conversion process, which gives rise to the change of wave behavior such as group and phase velocities.

3.8. Conclusion

This paper has provided an insight into the measurement of ultrasonic guided waves in partially immersed plates. The main contributions are concluded as follows:

(1). Global matrix method is employed to derive the theoretical dispersion curves and modes shapes of guided waves for a 2 mm thick steel plate and the plate with one side loaded with water. It is found that the low-frequencies QS wave in the one-side water-immersed plate and the A_0 wave in the dry plate have similar wavenumbers and deformations. But the similarity reduces with frequency.

(2). A 3D FE model is developed to simulate the guided wave field in the steel plate with one side partially immersed in water. The simulation results are validated by the experimental data. The frequency shift phenomenon and the guided wave amplitudes with propagation distance can be well predicted.

(3). The experimental studies are conducted on the empty tank and the partially water-filled tank, respectively. It is confirmed that the frequency shift phenomenon is due to the presence of water. The further investigation presents a segmented frequency wavenumber analysis to graphically demonstrate the mode conversion process, which is divided into three segments: (i) before guided waves propagate into the water-immersed plate, (ii) guided waves just propagate into the water-immersed plate, and (iii) after a short propagation distance in the water-immersed plate. The experimental data are compared with the theoretical dispersion curves, through which the mode identities and the corresponding experimentally measured wave energy can be determined.

(4). The guided wave energy shift in the frequency occurs during the mode conversion process, which is not caused by the material nonlinearity (micro cracks) of the plate. The amplitudes of the guided wave signals measured from the water-immersed plate section are much smaller than those obtained from the water-free plate section, on which the frequency shift phenomenon is not observed. Then, the mechanism of the energy shift in frequency

phenomenon is explained by the attenuation dispersion curves of leaky A_0 wave and the mode shapes of QS wave.

(5). Based on the findings, the selection of appropriate excitation frequency is discussed for damage detection of partially submerged structures, assessing liquid properties and levels, and fluid manipulations.

In summary, comprehensive investigations have been carried out for the frequency dependence of the mode conversion from A_0 wave to QS wave in a steel plate with one side partially immersed in water. The findings can provide support for the further development of guided wave-based techniques for damage detection on partially immersed structures, liquid-level assessing, and fluid-property sensing. This paper has only focused on the plate partially immersed in water. Future work can study the partially immersed structures with different geometries and investigate the effect when the structure is immersed in other types of liquid. In addition, the influence of damage such as corrosion pits or stress cracking on the guided wave propagation and mode conversion can be investigated.

3.9. Acknowledgment

This work was funded by the Australia Research Council (ARC) under grant numbers DP200102300 and DP210103307. The authors are grateful for this support.

3.10. Reference

[1] J. Moll, C.P. Fritzen, Guided waves for autonomous online identification of structural defects under ambient temperature variations, Journal of Sound and Vibration, 331 (2012) 4587-4597.

[2] J. He, C.A.C. Leckey, P.E. Leser, W.P. Leser, Multi-mode reverse time migration damage imaging using ultrasonic guided waves, Ultrasonics, 94 (2019) 319-331.

[3] A. Aseem, C.T. Ng, Debonding detection in rebar-reinforced concrete structures using second harmonic generation of longitudinal guided eave, NDT & E International, (2021) 102496.

[4] S. He, C.-T. Ng, C. Yeung, Time-domain spectral finite element method for modeling second harmonic generation of guided waves induced by material,

geometric and contact nonlinearities in beams, International Journal of Structural Stability and Dynamics, 20 (2020) 2042005.

[5] Y. Choi, S.H. Abbas, J.-R. Lee, Aircraft integrated structural health monitoring using lasers, piezoelectricity, and fiber optics, Measurement, 125 (2018) 294-302.

[6] M. Liu, S. Chen, Z.Z. Wong, K. Yao, F. Cui, In situ disbond detection in adhesive bonded multi-layer metallic joint using time-of-flight variation of guided wave, Ultrasonics, 102 (2020) 106062.

[7] K. Wang, M. Liu, Z. Su, S. Guo, F. Cui, Mode-mismatching enhanced disbond detection using material nonlinearity in guided waves at low frequency, Journal of Sound and Vibration, 490 (2021) 115733.

[8] B. Zima, R. Kędra, Baseline-free debonding detection in reinforced concrete structures by elastic wave propagation, Measurement, 172 (2021) 108907.

[9] X. Hong, Y. Liu, Y. Liufu, P. Lin, Debonding detection in hidden frame supported glass curtain walls using the nonlinear ultrasonic modulation method with piezoceramic transducers, Sensors, 18 (2018) 2094.

[10] O. Önen, Dispersion and Sensitivity Analysis of Quasi-scholte wave liquid sensing by analytical methods, Journal of Sensors, 2017 (2017).

[11] R. Kazys, L. Mazeika, R. Sliteris, R. Raisutis, Measurement of viscosity of highly viscous non-Newtonian fluids by means of ultrasonic guided waves, Ultrasonics, 54 (2014) 1104-1112.

[12] X. Hong, B. Zhang, Y. Liu, Z. Zhou, M. Ye, H. Qi, Liquid level detection in porcelain bushing type terminals using piezoelectric transducers based on auto-encoder networks, Measurement, 141 (2019) 12-23.

[13] S. Tietze, F. Singer, S. Lasota, S. Ebert, J. Landskron, K. Schwuchow, K.S. Drese, G. Lindner, Monitoring of soft deposition layers in liquid-filled tubes with guided acoustic waves excited by clamp-on transducers, Sensors, 18 (2018) 526.

[14] M. Schmitt, K. Schmidt, S. Olfert, J. Rautenberg, G. Lindner, B. Henning, L.M. Reindl, Detection of coatings within liquid-filled tubes and containers by mode conversion of leaky Lamb waves, J. Sens. Sens. Syst., 2 (2013) 73-84.

[15] J.L. Rose, Ultrasonic guided waves in solid media, Cambridge university press, 2014.

[16] J. Chen, Z. Su, L. Cheng, Identification of corrosion damage in submerged structures using fundamental anti-symmetric Lamb waves, Smart Materials and Structures, 19 (2009) 015004.

[17] J. Chen, Z. Su, L. Cheng, The medium coupling effect on propagation of guided waves in engineering structures and human bone phantoms, Coupled systems mechanics, (2012).

[18] F.B. Cegla, P. Cawley, M.J.S. Lowe, Material property measurement using the quasi-Scholte mode—A waveguide sensor, The Journal of the Acoustical Society of America, 117 (2005) 1098-1107.

[19] S. Tietze, M. Reißenweber, J. Schlemmer, G. Lindner, Investigation of the Surface Condition of an Electrode after Electropolishing under the Influence of Surface Acoustic Waves, Physics Procedia, 70 (2015) 1039-1042.

[20] V. Aubert, R. Wunenburger, T. Valier-Brasier, D. Rabaud, J.-P. Kleman, C. Poulain, A simple acoustofluidic chip for microscale manipulation using evanescent Scholte waves, Lab on a Chip, 16 (2016) 2532-2539.

[21] T. Hayashi, R. Fujishima, Defect detection using quasi-Scholte wave for plate loaded with water on single surface, Materials Transactions, (2016) M2016204.

[22] L. Yu, B. Lin, Y.-J. Shin, J. Wang, Z. Tian, Ultrasonic gas accumulation detection and evaluation in nuclear cooling pipes, SPIE, 2012.

[23] Z. Tian, L. Yu, Lamb wave structural health monitoring using frequency-wavenumber analysis, in: AIP Conference Proceedings, AIP, 2013, pp. 302-309.

[24] P. Guo, B. Deng, X. Lan, K. Zhang, H. Li, Z. Tian, H. Xu, Water level sensing in a steel vessel using A0 and quasi-Scholte waves, Journal of Sensors, 2017 (2017).

[25] X. Hu, C.-T. Ng, A. Kotousov, Scattering characteristics of quasi-Scholte waves at blind holes in metallic plates with one side exposed to water, NDT & E International, 117 (2021) 102379.

[26] L. Yu, Z. Tian, Case study of guided wave propagation in a one-side water-immersed steel plate, Case Studies in Nondestructive Testing and Evaluation, 3 (2015) 1-8.

[27] B. Pavlakovic, M. Lowe, Disperse user manual: a system for generating dispersion curves, Copyright B Pavlakovic, M Lowe, (2003).

[28] E. Glushkov, N. Glushkova, O. Miakisheva, Analytically based study of ultrasonic sounding of an immersed plate: hidden mode A0 and backward leaky waves, Proceedings of Meetings on Acoustics, 38 (2019) 065008.

[29] P. Rizzo, J.-G. Han, X.-L. Ni, Structural health monitoring of immersed structures by means of guided ultrasonic waves, Journal of Intelligent Material Systems and Structures, 21 (2010) 1397-1407.

[30] P. Rajagopal, M. Drozdz, E.A. Skelton, M.J. Lowe, R.V. Craster, On the use of absorbing layers to simulate the propagation of elastic waves in unbounded isotropic media using commercially available finite element packages, NDT & E International, 51 (2012) 30-40.

[31] J.R. Pettit, A. Walker, P. Cawley, M. Lowe, A stiffness reduction method for efficient absorption of waves at boundaries for use in commercial finite element codes, Ultrasonics, 54 (2014) 1868-1879.

[32] H. Mohseni, C.-T. Ng, Rayleigh wave propagation and scattering characteristics at debondings in fibre-reinforced polymer-retrofitted concrete structures, Structural Health Monitoring, 18 (2019) 303-317.

[33] X. Hu, C.-T. Ng, A. Kotousov, Ultrasonic guided wave field modeling in a one-side water-immersed steel plate, Lecture Notes in Civil Engineering, 2021, pp. 1131-1140.

[34] R. Soleimanpour, C.-T. Ng, Scattering analysis of nonlinear Lamb waves at delaminations in composite laminates, Journal of Vibration and Control, (2021) 1077546321990145.

[35] Abaqus, Abaqus 6.13 Analysis User's Guide, Dassault Systems Simulia Corp, Providence, RI, (2013).

[36] Q. Xie, C. Ni, Z. Shen, Defects detection and localization in underwater plates using laser laterally generated pure non-dispersive S0 mode, Applied Sciences, 9 (2019) 459.

[37] M. Abbas, M. Shafiee, An overview of maintenance management strategies for corroded steel structures in extreme marine environments, Marine Structures, 71 (2020) 102718.

[38] J. Bingham, M. Hinders, Lamb wave characterization of corrosion-thinning in aircraft stringers: Experiment and three-dimensional simulation, The Journal of the Acoustical Society of America, 126 (2009) 103-113.

[39] V.T. Rathod, D. Roy Mahapatra, Ultrasonic Lamb wave based monitoring of corrosion type of damage in plate using a circular array of piezoelectric transducers, NDT & E International, 44 (2011) 628-636.

[40] T. Gao, H. Sun, Y. Hong, X. Qing, Hidden corrosion detection using laser ultrasonic guided waves with multi-frequency local wavenumber estimation, Ultrasonics, 108 (2020) 106182.

[41] X. Hu, C.-T. Ng, A. Kotousov, Damage detection of partially immersed plates using guided waves, Recent Advances in Structural Health Monitoring Research in Australia, Nova Science Publishers Inc., 2021.

[42] A.E. Takiy, C. Kitano, R.T. Higuti, S.C.G. Granja, V.T. Prado, L. Elvira, O. Martínez-Graullera, Ultrasound imaging of immersed plates using high-order Lamb modes at their low attenuation frequency bands, Mechanical Systems and Signal Processing, 96 (2017) 321-332.

[43] S. Sharma, A. Mukherjee, Damage detection in submerged plates using ultrasonic guided waves, Sadhana, 39 (2014) 1009-1034.

[44] S. Sharma, A. Mukherjee, Ultrasonic guided waves for monitoring corrosion in submerged plates, Structural Control and Health Monitoring, 22 (2015) 19-35.

[45] E. Pistone, K. Li, P. Rizzo, Noncontact monitoring of immersed plates by means of laser-induced ultrasounds, Structural Health Monitoring, 12 (2013) 549-565.

[46] Y. Liu, X. Hong, B. Zhang, A novel velocity anisotropy probability imaging method using ultrasonic guided waves for composite plates, Measurement, 166 (2020) 108087.

[47] L. Yu, Z. Tian, L. Zhao, Gas accumulation detection in a water tank using Lamb waves, ASME 2012 Conference on Smart Materials, Adaptive Structures and Intelligent Systems, 2012, pp. 807-815.

[48] A. Takiy, S. Granja, R. Higuti, C. Kitano, L. Elvira, O. Martinez-Graullera, F.M. de Espinosa, Theoretical analysis and experimental validation of the Scholte wave propagation in immersed plates for the characterization of viscous fluids, 2013 IEEE International Ultrasonics Symposium (IUS), Ieee, 2013, pp. 1614-1617.

[49] F.B. Cegla, P. Cawley, M.J.S. Lowe, Fluid bulk velocity and attenuation measurements in non-Newtonian liquids using a dipstick sensor, Measurement Science and Technology, 17 (2005) 264.

[50] S. Tietze, J. Schlemmer, G. Lindner, Influence of surface acoustic waves induced acoustic streaming on the kinetics of electrochemical reactions, SPIE, 2013.

Chapter 4. Early damage detection of metallic plates with one side exposed to water using the second harmonic generation of ultrasonic guided waves

Abstract

Metallic plates are the main structural components in a wide range of thin-walled structures, such as nuclear cooling pipes, pressure vessels, rocket fuel tanks, and submarine hulls. These structures operate in extreme environments and are subjected to transient and repetitive loads. Real-time health monitoring of these structures is indispensable because they are vulnerable to fatigue and corrosion damage. Second harmonic generation is one of the reliable damage detection approaches to evaluate microstructural evolution and has been successfully applied to characterize initial damage on different structures in gaseous environments. However, there have been very limited studies on the second harmonics generation on the structures submerged in liquid. This paper experimentally and numerically investigates the feasibility of using second harmonic generation to evaluate the material degradation of metallic plates with one side exposed to water. The fundamental leaky symmetric Lamb wave mode (leaky S_0) at low frequencies is selected because it has low-attenuation and weakly dispersive features, enabling approximate internal resonance. The experimental results show that the second harmonics of leaky S_0 waves grow linearly with the propagation distance. The growth rate of the relative nonlinearity parameter (β') can be related to the material nonlinearity of the one-side water-immersed plate. In addition, this study proposed a three-dimensional (3D) finite element (FE) model to simulate the generation of second harmonics in the one-side water-immersed plate. The material properties of the plate are modeled by the Murnaghan strain energy function. The Murnaghan constants of aluminum that describe the material nonlinearity at different fatigue levels are obtained from a previous experimental study. The simulation results demonstrate that the values of β' change significantly with the material properties

of the one-side water-immersed plates in the initial stages of fatigue damage. Thus, it can be concluded that the second harmonic generation techniques can be used for early damage detection of metallic plates with one side exposed to water.

Keywords: Leaky Lamb waves; Second harmonic generation; Nonlinear guided waves; Submerged structures; Nondestructive evaluation; Extreme operational condition

Statement of Authorship

Title of Paper	Early damage detection of metallic plates with one side exposed to water using the second harmonic generation of ultrasonic guided waves
Publication Status	☑ Published ☐ Accepted for Publication ☐ Submitted for Publication ☐ Unpublished and Unsubmitted w ork w ritten in manuscript style
Publication Details	X. Hu, C.T. Ng, A. Kotousov, (2022). Early damage detection of metallic plates with one side exposed to water using the second harmonic generation of ultrasonic guided waves. *Thin-Walled Structures*, 176, 109284.

Principal Author

Name of Principal Author (Candidate)	Xianwen Hu		
Contribution to the Paper	Conceptualization, Developing and validating numerical models, Conducting experimental measurements, Signal processing and data analysis, Writing the original draft and editing.		
Overall percentage (%)	80%		
Certification:	This paper reports on original research I conducted during the period of my Higher Degree by Research candidature and is not subject to any obligations or contractual agreements with a third party that would constrain its inclusion in this thesis. I am the primary author of this paper.		
Signature		Date	07/03/2022

Co-Author Contributions

By signing the Statement of Authorship, each author certifies that:

i. the candidate's stated contribution to the publication is accurate (as detailed above);

ii. permission is granted for the candidate in include the publication in the thesis; and

iii. the sum of all co-author contributions is equal to 100% less the candidate's stated contribution.

Name of Co-Author	Ching-Tai Ng		
Contribution to the Paper	Supervision, writing – review & editing.		
Signature		Date	9/3/2022

Name of Co-Author	Andrei Kotousov		
Contribution to the Paper	Supervision, writing – review & editing		
Signature		Date	07/03/2022

Please cut and paste additional co-author panels here as required.

4.2. Introduction

Thin-walled structures are widely used in energy, petrochemical, aerospace, civil, and ocean engineering, such as nuclear cooling pipes, pressure vessel, rocket fuel tanks, storage tanks, and submarine hulls. These structures usually have one side exposed to liquid and serve in extreme environments. They are subjected to cyclic loads due to the draining and refilling process, liquid sloshing impacts, and temperature fluctuations [1, 2]. Over time, fatigue damage takes place even though the peak values of the cyclic loads are much smaller than the loading capacity of the structures [3, 4]. In the early damage stage, fatigue is distributed in the material and appears as microscopic imperfections, such as dislocations, persistent slip bands, precipitates, and short cracks at the micro-scale. Optical images of the microstructural features can be found in [5, 6]. As the number of loading cycles increases, these microscopic defects accumulate, coalesce, and form macroscopic cracks, which continuously grow to their critical sizes and cause catastrophic failures [7]. In addition to the cyclic loading, the corrosive operational conditions of the one-side submerged plate can accelerate the damage-accumulation process by corrosion, which results in the metal wear through electrochemical reaction [8, 9]. To mitigate the risk of in-service failure of the structures, real-time health monitoring of the submerged plate structures is indispensable. Existing non-destructive testing (NDT) for submerged structures has visual inspection by divers and robots [10], acoustic emission [11, 12], hydro test [13], magnetic flux leakage test [14], and eddy current test [15]. Most of these approaches require periodic shutdown of the devices and can only inspect a localized area. They are costly, inconvenient, and inefficient for scanning a large structure.

Guided waves have been extensively studied as a potential alternative to overcome the aforementioned limitations of existing NDT techniques. They have the capability of fast propagation over long distances, volumetric inspection of a relatively large area with a small number of sensors, the ability to scan structures with coatings and insulations, and the ability to monitor defects in inaccessible regions [16, 17]. The majority of the studies on guided wave applications were carried out on the structures in gaseous environments. However, guided waves behave differently when the structures are exposed to liquid. The liquid coupling

can change the dynamic properties of the plate structures [18] and provides a way for the guided wave energy to leak into the surrounding liquid medium [19, 20]. Due to the energy leakage, guided waves that propagate in submerged plates are called leaky Lamb waves, which have multi-modal and dispersive features. At any excitation frequency, multiple leaky symmetric and antisymmetric Lamb wave modes can exist simultaneously. Each of these wave modes behaves differently and varies with the excitation frequency. Compared with structures surrounded by air, guided wave applications on the submerged structures are much more challenging because most of the leaky Lamb wave modes decay quickly and disappear after a short propagation distance. Only a limited number of leaky Lamb wave modes at their corresponding low-attenuation frequency bands can travel a long distance, which has the potential to enable large-area inspection for the submerged structure [19]. Therefore, a good understanding of the wave propagation characteristics is desired for the practical application of leaky Lamb wave-based techniques.

Several researchers studied different leaky Lamb wave modes to evaluate various defects in the submerged plate structures. Santos and Perdigao [21] investigated the fundamental leaky symmetric Lamb wave mode (leaky S_0) in a pitch and catch configuration to detect and estimate the size of circular hole defects in bonded aluminum lap joints fully immersed in water. An empirical parameter that was defined based on the amplitudes of the received signals was shown to have a linear correlation with the dimensions of the defects. Chen, Su, and Cheng [22] investigated the propagation characteristics of the fundamental leaky anti-symmetric Lamb wave mode (leaky A_0) in a submerged plate. Circular holes created on the submerged plate mechanically and chemically were accurately detected by leaky A_0 waves with the appropriate rectification for the medium coupling effect. Rizzo et al. [23] used a pulsed laser focusing on the upper surface of the plate to excite leaky Lamb waves in an immersed aluminum plate. The signals received by immersed transducers included leaky S_0 waves, quasi-Scholte waves, and pressure waves. The leaky S_0 mode that has the fastest propagation speed was well separated from the other wave modes. Then, the leaky S_0 waves were extracted from the rest of the signals for further processing with continuous wavelet transform. Artificial defects, such as notches and circular holes, which were as small as a few millimeters, were successfully captured. Sharma and Mukherjee [24] studied leaky

Lamb waves on an underwater steel plate using two immersed transducers inclined at specific angles. Three leaky Lamb wave modes were generated at their corresponding low-attenuation frequencies, which were the leaky S_0 wave mode, the first-order leaky symmetric Lamb wave mode (leaky S_1), and the first-order leaky anti-symmetric Lamb wave mode (leaky A_1). Each of these wave modes showed different sensitivities in monitoring the progressive notch damage machined on the underwater steel plate. They concluded that leaky S_1 and leaky A_1 waves were more sensitive to surface defects, of which the depth was less than 37.5% of the plate thickness. In contrast, leaky S_0 waves were more suitable for evaluating the deeper defects since the amplitudes of the transmitted leaky S_0 waves consistently decreased with the notch depth. Sharma and Mukherjee [25] used similar techniques to monitor corrosion damage in an underwater plate. The initial surface degradation could be successfully identified by leaky S_1 waves. Further progression of the corrosion was evaluated better by leaky S_0 waves. Takiy et al. [19] conducted experimental measurements on a submerged aluminum plate to confirm the existence of leaky S_0, leaky A_1, leaky S_1, and the second-order leaky symmetric Lamb wave mode (leaky S_2) at their corresponding low-attenuation frequency bands. Then, leaky S_1 waves at 3.4 MHz-mm were selected for characterizing damage. An image of the submerged plate was obtained to precisely identify the locations of five drilled holes. Xie, Ni, and Shen [26] proposed an experimental method to generate pure leaky S_0 waves by applying the pulsed laser radiation laterally at the whole side of an aluminum plate submerged in water. Through interacting with the damage, the generated leaky S_0 waves can mode convert into leaky A_0 waves, which have mostly out-of-plane wave motions. Hence, the damage can be easily recognized. However, clear edges of the real structures are not always accessible, making this pure wave mode excitation at the structural edges very challenging in practice.

These studies demonstrated that it is feasible to use leaky Lamb waves for identifying damage in plate structures submerged in liquid. The presence of defects with sizes in the order of millimeters can be detected and quantified based on the linear features of leaky Lamb waves, such as the change of wave speed and amplitude. It was reported that the sensitivity of linear ultrasonic guided waves is limited to damage of a size comparable to the wavelength of the selected guided

wave mode [27, 28]. However, they are insensitive to smaller defects in the initial damage stage. Before macroscopic cracks nucleate, the evolution of microstructural defects with load accounts for a major part of the total service life of a structure. In many cases, when the microstructural damage grows into macro scale, the remaining life of the structures is very short [29]. Therefore, it is better to identify defects sooner than later. Earlier detection of damage allows more time to characterize the evolution of the damage and schedule the maintenance actions for improving safety. Recent studies have proposed several nonlinear guided wave techniques to capture the microstructure evolution and early-stage material degradation [30]. Second harmonic generation is one of the most popular nonlinear techniques and has been successfully applied to different structures in gaseous environments to evaluate plasticity-induced damage [31, 32], thermal degradation [33, 34], precipitation [35], small fatigue cracks [36-38], debonding [39] and bolt loosening [40]. In the early damage stage (before the appearance of macro cracks), the generation of second harmonics takes advantage of the fact that the microstructural features in real materials distort the passing sinusoidal ultrasonic waves. The distortion can generate new wave components at frequencies other than the excitation frequencies, which provides a way for the evaluation of the microstructural defects. However, the measurement of second harmonics is challenging due to the fact that the material nonlinearity is weak [41]. To ensure measurable generation of second harmonics, the incident waves should have finite amplitudes so that there is sufficient wave energy to interact with the microstructural features. In addition, wave mode selection is required to ensure that the primary waves and second harmonics conform to non-zero power transfer and phase velocity matching conditions [42-47].

The aforementioned studies on the second harmonic generation were carried out on the structures in gaseous environments. Although the nonlinear characteristics of guided waves have been demonstrated by a number of studies to be more sensitive to the microstructural defects in the early stage of damage and are less influenced by environmental changes, there have been very limited studies on the use of nonlinear guided waves for damage detection on the submerged structures. Undoubtedly, the vibration of the plate submerged in liquid behaves differently from that in the air [48-50]. Compared with structures in gaseous

environments, the generation and measurement of second harmonics on the submerged structure are more challenging because the wave energy can be absorbed by the surrounding liquid medium. So, the application of nonlinear guided waves for submerged structures deserves separate and careful studies considering the high reward for the earlier detection of material degradation.

This paper presents experimental and numerical investigations on the feasibility of using second harmonic generation to evaluate material degradation in metallic plates with one side in contact with water. Leaky S_0 mode is selected to generate second harmonic leaky S_0 waves due to the observations from previous studies that leaky S_0 mode at low frequencies has very low attenuation and its phase velocity decreases slowly with frequency [51-53]. These features make the primary and second harmonic leaky S_0 waves satisfy non-zero power flux and approximate phase velocity matching conditions. Then, experiments are carried out on a metal tank filled with water. Leaky Lamb waves are generated on the wall of the water-filled tank by a piezoceramic transducer and measured by a scanning laser vibrometer. It is demonstrated that second harmonics can be generated by leaky S_0 waves at low excitation frequencies and the corresponding relative nonlinearity parameters are growing linearly with the propagation distance. The growth rate of the relative nonlinearity parameters can be used to characterize the material stratus of the one-side water-submerged plate. After that, a three-dimensional (3D) finite element (FE) model is developed with the material nonlinearity of the submerged plate simulated by the Murgnahan strain energy function. The material properties of aluminum at different levels of fatigue damage are obtained from previous experimental results [54]. The numerical simulations are validated through the experimental data. Next, the experimentally validated 3D FE model is employed in the parametric study to analyze the second harmonic generation in the submerged plate at different levels of fatigue damage. The results show that leaky S_0 mode at low frequencies can generate measurable second harmonics, which are sensitive to the change of material properties of the one-side water-immersed plate at the initial stages of the fatigue damage. This paper is organized as follows. Section 4.3 introduces the second harmonic generation techniques and discusses the selection of leaky Lamb modes for the generation of second harmonics in the plate with one side exposed to water. Section 4.4 describes the experimental study. Section 4.5

shows the 3D FE model and simulation results. Finally, conclusions are drawn in Section 4.6.

4.3. Theoretical considerations for the second harmonic generation by leaky Lamb waves

4.3.1. Generation of second harmonics

All materials have microscopic imperfections such as micro-cracks, precipitates, and vacancies at the lattice level [37]. These microscopic defects contribute to weak material nonlinearity, which leads to a small deviation of the stress-strain relationship from the linear assumption of Hook's law. As shown in Figure 4.1, the material nonlinearity distorts a passing sinusoidal ultrasonic wave with central frequency (f_0), and second harmonics are generated at twice the excitation frequency ($2f_0$). This provides a way for characterizing the incipient damage in the structure. More comprehensive descriptions can be found in reviews by Chillara and Lissenden [30] and Lissenden [7].

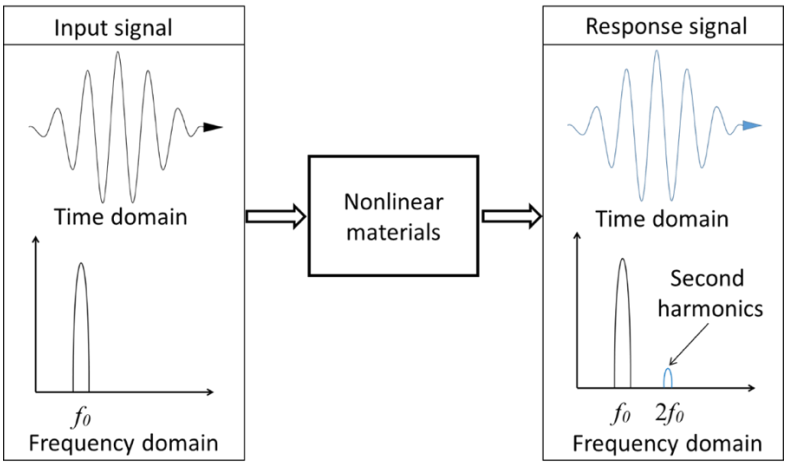

Figure 4.1: Concept of the second harmonic generation due to material nonlinearity

To illustrate the basics of wave distortion phenomena, a one-dimensional homogeneous and lossless media is considered here. The stress-strain relation of

the nonlinear material can be written in terms of the displacement gradient as a Taylor series expansion truncated at order 2

$$\sigma = Eu' + \frac{1}{2}\beta E\left(u'\right)^2 \tag{4.1}$$

where σ, u, E, and β are the stress, displacement, Young's modulus of the medium, and nonlinearity parameters, respectively. $u' = \partial u/\partial x$ is the displacement gradient. The particle motions can be described as

$$\sigma' = \rho\ddot{u} \tag{4.2}$$

where ρ represents the mass density; $\sigma' = \partial\sigma/\partial x$ and $\ddot{u} = \partial^2 u/\partial t^2$. Perturbation theory is employed to solve Eqs. (4.1) and (4.2), leading to the final solution [7]

$$u = A_1\cos(kx - wt) + A_2\cos(2kx - 2wt) \tag{4.3}$$

where k and w are the wavenumber and angular frequency of the excited primary waves. A_1 is the amplitude of the primary waves at w. $A_2 = \frac{1}{8}\beta k^2 A_1^2 x$ represents the amplitude of the second harmonics at $2w$. x is the propagation distance.

Two observations can be obtained from Eq.(4.3). Firstly, the primary waves and the second harmonics should have the same phase velocity, i.e., $c_p = w/k = 2w/2k$. Secondly, when the structure is excited by waves with a fixed wavenumber value k, the nonlinearity parameter β that correlates to the material nonlinearity can be determined by measuring the magnitudes of the primary waves and the second harmonics as

$$\beta = \frac{8}{k^2 x}\frac{A_2}{A_1^2} \tag{4.4}$$

For practical applications, the change in β with its initial value is more important than its absolute value. Therefore, a relative nonlinearity parameter β' is defined as

$$\beta' = \frac{A_2}{A_1^2} \propto \beta x \tag{4.5}$$

It can be seen from Eq.(4.5) that β' is proportional to β and grows linearly with the propagation distance x. β can be evaluated by the gradient of accumulation of β'. Therefore, any abnormal increase in β' indicates an increase in the material nonlinearity and progress in material degradation [36]. Although Eq. (4.1)-Eq. (4.4) are derived for longitudinal waves, Eq.(4.5) has been widely considered to be applicable for characterizing the second harmonic generation of Lamb waves [37, 44], Rayleigh waves [55], and Edge waves [56]. Therefore, β' is employed in this study to quantify the change of the second harmonics of the leaky Lamb waves.

4.3.2. Selection of primary leaky Lamb wave modes

Although the generation of second harmonics by guided waves has been studied for evaluating the incipient damage in various structures that are open to the air, the feasibility of using leaky Lamb wave modes to generate second harmonics in the plate with one side exposed to water has not been explored. Considering the multi-modal and dispersive features, the selection of primary leaky Lamb waves is important. This section introduces the theoretical derivation of the dispersion curves, which describe the number of leaky Lamb wave modes and their corresponding properties with the frequency. Based on the dispersion curves, the leaky Lamb wave modes that have low attenuation and low dispersion characteristics are identified. Then, the primary wave mode and excitation frequency are selected to meet the following three conditions. Firstly, the primary wave mode should have sufficient wave energy propagating in the submerged structure to interact with the microstructural features so that the generation of second harmonics best reflects the material nonlinearity. Secondly, the primary waves should be of the same type of wave mode as the second harmonics to ensure that the wave energy can be transferred between the primary waves and the second harmonics [46]. Thirdly, the primary waves and the second harmonics should have similar phase velocities.

Consider a plate loaded with water on its bottom surface, as shown in Figure 4.2. Traction-free boundary conditions apply to the top surface of the plate as

$$\sigma_{33}^{Plate\_0} = \sigma_{31}^{Plate\_0} = 0 \tag{4.6}$$

where $\sigma_{33}^{Plate\_0}$ and $\sigma_{31}^{Plate\_0}$ are the normal and shear stress on the top surface of the plate, respectively. The bottom surface of the plate is coupled to the water layer. Under the non-viscosity assumption that water cannot sustain shear forces, the boundary conditions at the plate-water interface can be described as

$$\begin{aligned} u_{33}^{Plate\_d} &= u_{33}^{Water\_d} \\ \sigma_{33}^{Plate\_d} &= \sigma_{33}^{Water\_d} \\ \sigma_{31}^{Plate\_d} &= 0 \end{aligned} \tag{4.7}$$

where $u_{33}^{Plate\_d}$, $\sigma_{33}^{Plate\_d}$, and $\sigma_{31}^{Plate\_d}$ represent the normal displacement, normal stress, and shear stress of the plate at the plate-water interface, respectively. $u_{33}^{Water\_d}$ and $\sigma_{33}^{Water\_d}$ are the normal displacement and normal stress of the water at the plate-water interface, respectively.

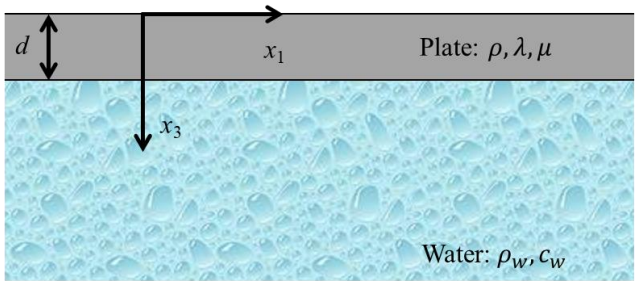

Figure 4.2. Schematic diagram of a plate loaded with water on its bottom surface

Previous studies have derived the characteristic equation of the leaky Lamb waves for the one-side water-immersed plate [57]

$$\begin{vmatrix} q^2-k^2 & q^2-k^2 & -2qk & 2qk & 0 \\ 2pk & -2pk & q^2-k^2 & q^2-k^2 & 0 \\ (q^2-k^2)e^{ipd} & (q^2-k^2)e^{-ipd} & -2qke^{iqd} & 2qke^{-iqd} & \dfrac{w^2\rho_w}{\mu} \\ 2pke^{ipd} & -2pke^{-ipd} & (q^2-k^2)e^{iqd} & (q^2-k^2)e^{-iqd} & 0 \\ pe^{ipd} & -pe^{-ipd} & -ke^{iqd} & -ke^{-iqd} & \dfrac{w^2}{c_w^2}-k^2 \end{vmatrix} = 0 \tag{4.8}$$

where $p=\sqrt{w^2/c_L^2-k^2}$, $q=\sqrt{w^2/c_S^2-k^2}$, $c_L=\sqrt{(\lambda+2\mu)/\rho}$, $c_S=\sqrt{\mu/\rho}$. $\lambda=E\nu/\left[(1+\nu)(1-2\nu)\right]$ and $\mu=E/\left[2(1+\nu)\right]$ are the first and second Lame constants of the plate, respectively. E and ν are Young's modulus and Poisson's ratio of the plate, respectively. ρ and ρ_w represent the density of the plate and the surrounding water, respectively. c_w is the speed of the bulk wave in the water. Eq.(4.8) can be solved numerically and the solutions can be presented by a series of dispersion curves.

Table 4.1. Material properties of the aluminum plate and water

Aluminum density ρ (kg/m3)	2700
Aluminum 1st Lame parameter λ (GPa)	51.64
Aluminum 2nd Lame parameter μ (GPa)	26.60
Water density ρ_w (kg/m3)	1000
Water bulk wave velocity c_w (m/s)	1500

Figure 4.3 shows the dispersion curves of a 1.6 mm thick aluminum plate with one side in contact with water. The material properties are given in Table 4.1. Within the frequency range up to 1MHz, there are only three wave modes, which are leaky S_0, leaky A_0, and quasi-Scholte waves. Other higher-order wave modes appear when the frequency increases. The quasi-Scholte wave that propagates along the plate-water interface has very low attenuation (close to zero) for the entire frequency bandwidth as shown in Figure 4.3(c). This wave mode is highly dispersive in the low-frequency range (below 250 kHz) as denoted by the blue dotted lines in Figures 4.3(a) and 4.3(b). The phase velocity of the quasi-Scholte wave increases monotonically with frequency until its value reaches the speed of the bulk wave in the surrounding water (around 1500 m/s). Further increasing the frequency, the quasi-Scholte wave becomes nondispersive. Although the quasi-Scholte wave at the frequency range over 250 kHz has low attenuation and satisfies phase velocity matching conditions, it is not considered in this study. The reason is that the quasi-Scholte wave in the nondispersive frequency range has most of its

wave energy concentrated to the waterside, and the wave motions in the plate structure are negligible [20, 51, 58]. So, it has insufficient wave motions to interact with the microstructural features of the submerged plate.

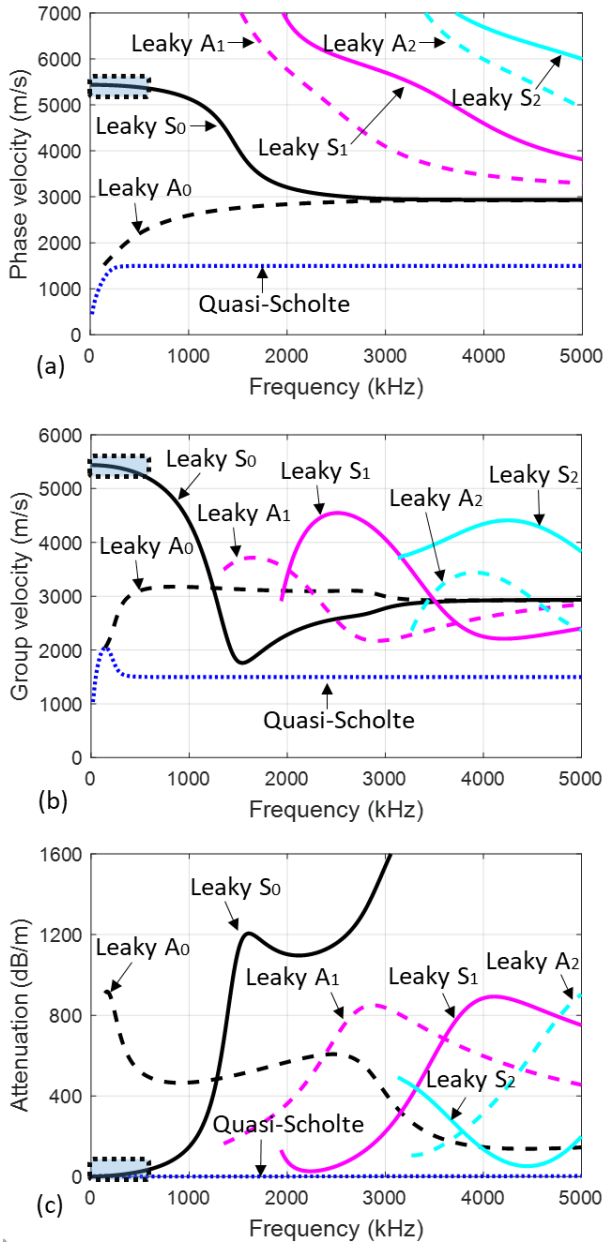

Figure 4.3. (a) Phase velocity, (b) group velocity, and (c) attenuation dispersion curves of a 1.6 mm thick aluminum plate loaded with water on its bottom surface

In addition to quasi-Scholte waves, leaky S_0 waves also have low attenuation and low dispersion characteristics within the frequency range up to 600 kHz. The phase velocity of leaky S_0 waves decreases slowly with frequency. For example, the phase velocity of the leaky S_0 mode at 100 kHz is 5435 m/s, and that at 500 kHz is 5383 m/s. The deviation is around 0.96%. A previous study defined the approximate phase velocity matching condition as the relative phase velocity deviation less than 1% [59]. Therefore, if the leaky S_0 waves below 250 kHz are selected as the primary waves, the second harmonics at twice the frequency should satisfy the approximate phase velocity matching condition with the primary waves. Another key factor is that the low-attenuation frequency band of the leaky S_0 mode is limited to the frequency range up to 600 kHz as shown by the black solid line in Figure 4.3(c). As the frequency increases beyond 600 kHz, the attenuation of the leaky S_0 wave increases exponentially. Also, the phase velocity and group velocity decrease quickly with the frequency.

Figure 4.4 presents the mode shapes of leaky S_0 waves for the aluminum plate with one side in contact with water. The mode shape diagrams show the distributions of the displacements of leaky S_0 waves through the thickness of the plate. The x-axis denotes the magnitudes that are normalized by the maximum displacement amplitudes. The y-axis denotes the thickness location x_3 that is defined in Figure 4.2. The red dashed lines represent the particle's displacements in the direction parallel to the plate surface (in-plane displacements). The blue solid lines show the displacement in the direction normal to the plate surface (out-of-plane displacements). It can be seen that the out-of-plane displacements between the plate and the water areas are continuous. In comparison, the in-plane displacements are disconnected. When the frequency is below 600 kHz, the mode shape of leaky S_0 waves is dominated by the in-plane displacements in the plate as indicated by the red dashed lines in Figure 4.4(a). The vast majority of the wave energy is conserved in the one-side water-immersed plate with minimal loss, making it ideal for using the leaky S_0 wave to scan the one-side water-immersed plate. However, the out-of-plane displacements in both the plate and water regions increase with the frequency. This indicates more energy leakage from the structure into the surrounding liquid medium. From these observations, the excitation

frequencies are chosen to be below 250 kHz in the following experimental and numerical studies.

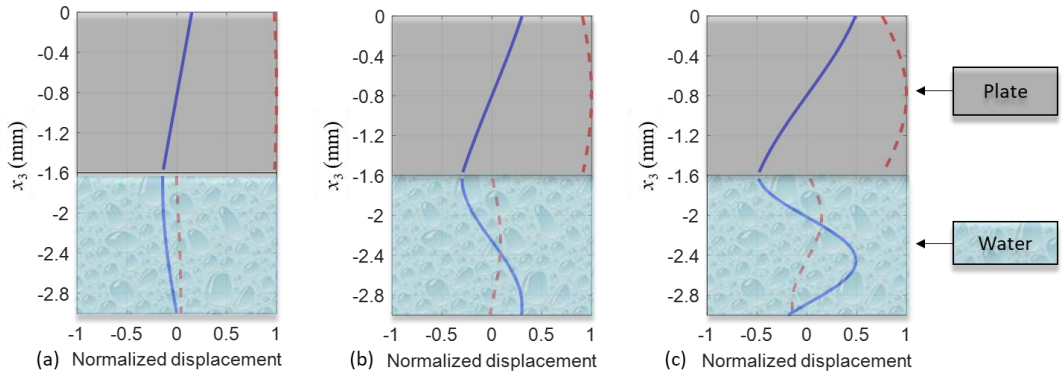

Figure 4.2. Mode shapes of leaky S_0 wave at (a) 300 kHz, (b) 600 kHz, and (c) 900 kHz for a 1.6 mm thick aluminum plate loaded with water on its bottom surface (the red dashed lines represent the in-plane displacements and the blue solid lines denote the out-of-plane displacements)

4.4. Experimental study

4.4.1. Experimental setup

This section presents an experimental study on the leaky Lamb wave propagation in a metal plate with one side in contact with liquid, which aims to simulate a variety of thin-walled structures operating in extreme conditions, such as nuclear cooling pipes, pressure vessels, rocket fuel tanks, and submarine hulls. The experiments were carried out using a metallic tank fully filled with water. The front wall of the tank was used as the test plate, which was a 1.6 mm thick aluminum plate. The internal surface of the test plate was in contact with water, while the outer surface was exposed to air.

Figure 4.5 illustrates the overall experiment setup and the top view of the water-filled tank. A computer-controlled signal generator (NI PIX-5412) was employed to generate a six-cycle Hanning window modulated sinusoidal tone burst pulse. Then, the signal was sent to a power amplifier (Ciprian HVA-800-A) and the voltage was increased to 160 Vp-p. After that, the amplified signal was sent to a

piezoceramic transducer (Ferroperm Pz27) which was bonded to the outer surface of the test plate. The circular piezoceramic transducer has a diameter of 10 mm and a thickness of 0.5 mm and can convert the electric signals to mechanic motions, exciting leaky lamb waves on the test plate. The thin and circular piezoceramic wafer deforms mainly in the radial direction which is parallel to the plate surface. As a result, the excitation should be dominated by the in-plane motions of the plate and leaky S_0 waves could be generated effectively.

The response signals were collected on the water-free surface by a non-contact scanning laser Doppler vibrometer (Polytec PSV-400-M2-20). Taking the center of the piezoceramic transducer as the origin, a Cartesian coordinate system was defined as shown in Figure 4.5. The x_1-axis denotes the in-plane direction parallel to the plate surface, and the x_3-axis is the out-of-plane direction that is normal to the plate surface. The measurement points are defined along a line parallel to x_1-axis. The signals were collected at a sampling rate of 25.6 MHz. To improve the quality of measurements, each signal was averaged by 1000 recordings and filtered by a low-pass filter with a cut-off frequency of 1MHz.

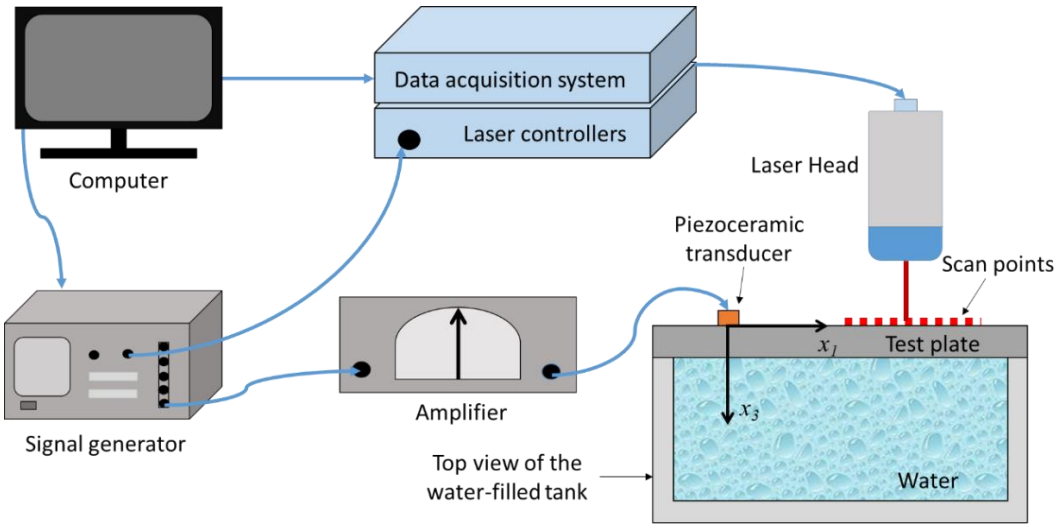

Figure 4.5. Schematic diagram of the experiment setup

4.4.2. Experimental results

Figure 4.6(a) presents an example of the experimentally measured signals. The excitation frequency was 170kHz, at which there were only leaky S_0, leaky A_0, and quasi-Scholte waves, as shown by the dispersion curves in Figure 4.3. The measurement point was 200 mm away from the excitation center. The first wave packet was identified as the leaky S_0 wave mode, which has the fastest group velocity, as shown in Figure 4.3(b). The phase velocity of the leaky S_0 wave mode at 170 kHz is 5431 m/s, and that at 340 kHz is 5413 m/s. So, the primary leaky S_0 wave is almost phase matched with its second harmonic with a deviation of 0.33%. It should be noted that the experimental data mainly captured the out-of-plane motions on the plate surface because the laser beam was perpendicular to the test plate during the test. Since the out-of-plane displacement of the leaky S_0 wave was small as shown by the blue solid lines in Figure 4.4, the actual magnitudes of the leaky S_0 wave should be strong enough so that it could be measured by the scanning laser Doppler vibrometer.

The following wave packet should be dominated by the quasi-Scholte wave mode because the leaky A_0 wave mode decays quickly due to high attenuation [51]. At this excitation frequency, the quasi-Scholte wave is highly dispersive. The phase velocity of the quasi-Scholte mode at 170 kHz is 1317 m/s, and that at 340 kHz is 1488 m/s. The deviation of the phase velocity between the primary waves and the second harmonics is around 13%. Therefore, the quasi-Scholte waves do not satisfy the approximate phase velocity matching condition [59].

To further investigate, the first wave packet was cut from the rest of the signal to exclude the quasi-Schole waves and the unwanted reflections in the data. Figure 4.6(b) presents the window-cut signal. Then, the chopped signal was transferred to the frequency domain by FFT and is shown in Figure 4.6(c). There are two peaks for the primary waves (at 170 kHz) and the second harmonics (at 340 kHz), respectively, as highlighted by the black dotted line in Figure 4.6(c). There is also a small peak at three times the excitation frequency, which is the third harmonic [29, 60]. However, the signal-to-noise ratio of the third harmonics is much lower than that of the second harmonics, and the third harmonics are not the focus of the paper, so the third harmonics are not discussed in this study. After that, β' were

calculated by Eq.(4.5) at 21 locations distributed at 5 mm apart along a line from x_1 = 200 mm to x_1 = 300 mm. The values of β' are shown in Figure 4.6(d) with the error bars representing the standard deviations of five experimental measurements. A linear correlation between β' and the propagation distance is observed from x_1 = 200 mm to x_1 = 300 mm with a high value of R square. This confirms that the second harmonics were generated due to the material nonlinearity [33, 37]. Therefore, this experimentally validates that leaky S_0 waves at low frequencies satisfy approximate phase velocity matching conditions and are feasible to generate measurable second harmonics due to the material nonlinearity in the one-side water-immersed plate.

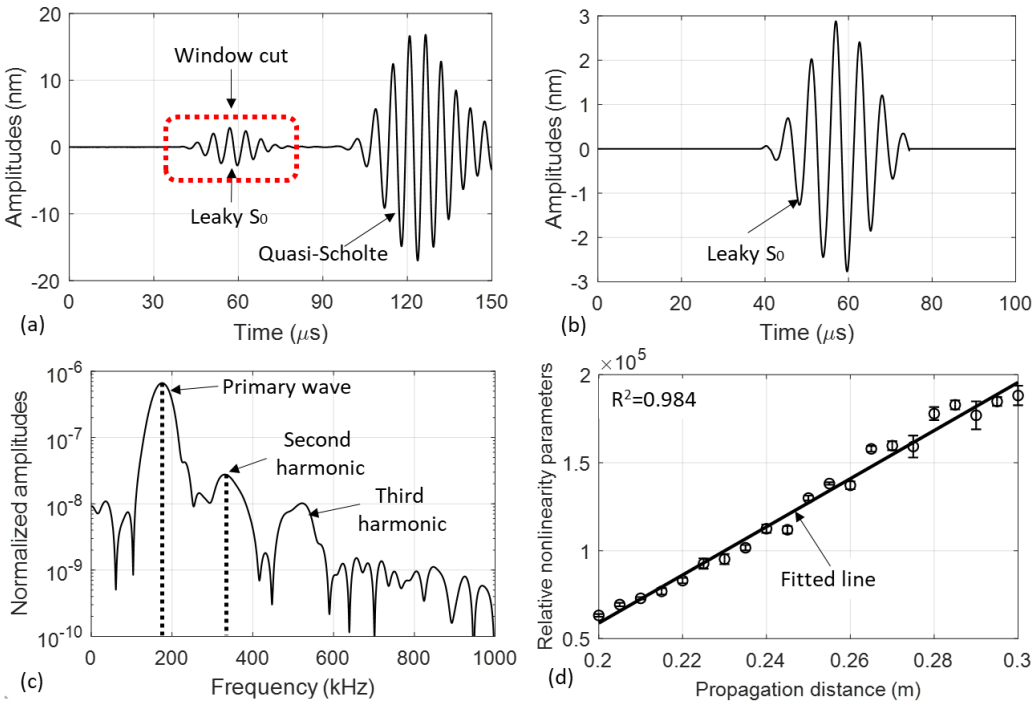

Figure 4.6. (a) The raw signal recorded by the laser vibrometer, (b) window-cut signal for further processing, (c) frequency spectrum of the extracted signal in (b), and (d) growth of relative nonlinearity parameters with propagation distance.

4.5. Finite element simulation

4.5.1. Model description

A 3D FE model was developed to simulate the leaky Lamb wave propagation in the one-side water-immersed plate. By applying the symmetry boundary conditions to the left and bottom edges of the plate, only the top right part of the plate was modeled. The plate modeled in the FE was 430 mm long, 250 mm wide, and 1.6 mm thick. The bottom surface was in contact with a water layer of the same planar area. The thickness of the water layer was 90 mm, which was chosen to avoid unwanted reflections from the bottom of the water layer. Figure 4.7 presents the schematic diagram of the FE model, which was modeled using the commercial software, ABAQUS. The bottom surface of the plate and the top surface of the water layer were tied together using the surface-based tie constraint, which connected the acoustic pressure of the water and the out-of-plane translations of the plate. Previous studies of ultrasonic guided waves in the solid-liquid coupled medium experimentally validated that the tie constraint could accurately model the solid-liquid interactions [22, 51, 58, 61]. The plate and the water layers were modeled by 3D eight-node reduced integration solid elements and 3D eight-node reduced integration acoustic elements, respectively. The largest dimension of the element size was less than 0.5 mm, ensuring that there were at least 20 FE nodes within the wavelength of the leaky S_0 wave [59, 62].

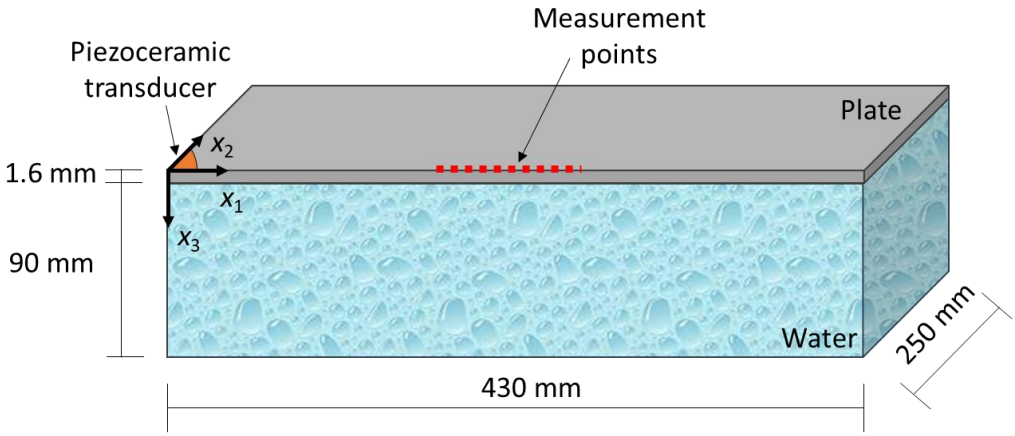

Figure 4.7. Schematic diagram of the 3D FE model.

To simulate the material nonlinearity of the one-side water-immersed plate, the Murnaghan strain energy function was introduced to define the material properties of the aluminum plate using VUMAT subroutine in ABAQUS. Murnaghan strain energy function includes the third-order Taylor series expansion of the strain potential and has been widely used in the analysis of second harmonic generation for modeling the nonlinear material behaviors [62-64]. This function can be written as

$$\begin{aligned} W(\mathbf{E}) = & \frac{1}{2}\lambda\left(\mathrm{tr}(\mathbf{E})\right)^2 + \mu\,\mathrm{tr}\left(\mathbf{E}^2\right) + \frac{1}{3}(l+2m)\left(\mathrm{tr}(\mathbf{E})\right)^3 \\ & - m\,\mathrm{tr}(\mathbf{E})\left(\left(\mathrm{tr}(\mathbf{E})\right)^2 - \mathrm{tr}\left(\mathbf{E}^2\right)\right) + n\det(\mathbf{E}) \end{aligned} \tag{4.9}$$

where l, m, and n are the Murnaghan constants which are related to the third-order elastic constants; $\mathbf{E} = \frac{1}{2}\left(\mathbf{F}^{\mathrm{T}}\mathbf{F} - \mathbf{I}\right)$ is the Lagrangian strain; $\mathbf{F}$ and $\mathbf{I}$ denote the deformation gradient and the identity tensor, respectively. Table 4.2 presents the values of Murnaghm constants of aluminum at different levels of fatigue damage, which are obtained from previous experimental results [54].

Table 4.2. Murnaghan constants of aluminum at different levels of fatigue damage [54]

	Murnaghan constants		
Fatigue life	*l* (GPa)	*m* (GPa)	*n* (GPa)
0%	-252.2	-325.0	-351.2
40%	-266.8	-332.8	-358.3
80%	-271.2	-335.8	-359.8

The leaky S_0 wave was excited by applying nodal displacements at the circumference of a circular transducer represented by the quarter-circle of 10 mm diameter located at the left-bottom corner of the plate. The excitation signal was a six-cycle Hanning window modulated sinusoidal tone burst pulse. The explicit module of ABAQUS was employed to solve the dynamic simulations. Figure 4.8

shows a snapshot of the simulation results with the excitation frequency of 170 kHz. The rainbow color represents the acoustic pressure in the water layer. It can be seen that the leaky S_0 wave propagates fastest with minimum wave energy leaking into the liquid. Following the leaky S_0 wave, the quasi-Scholte wave propagates at a speed slightly faster than the pressure wave in water. The acoustic pressure of quasi-Scholte waves is concentrated around the plate-water interface [58]. The leaky A_0 wave dominated by the out-of-plane displacements was not observed from the surface of the submerged plate. In general, the simulation results have a good agreement with the experimental data as shown in Figure 4.6(a). The numerically calculated acoustic wavefields provide additional information to interpret the experimental data. The simulation results of the 3D FE model are further validated in the following sections to gain physical insights into the second harmonic generation on the one-side water-immersed plate.

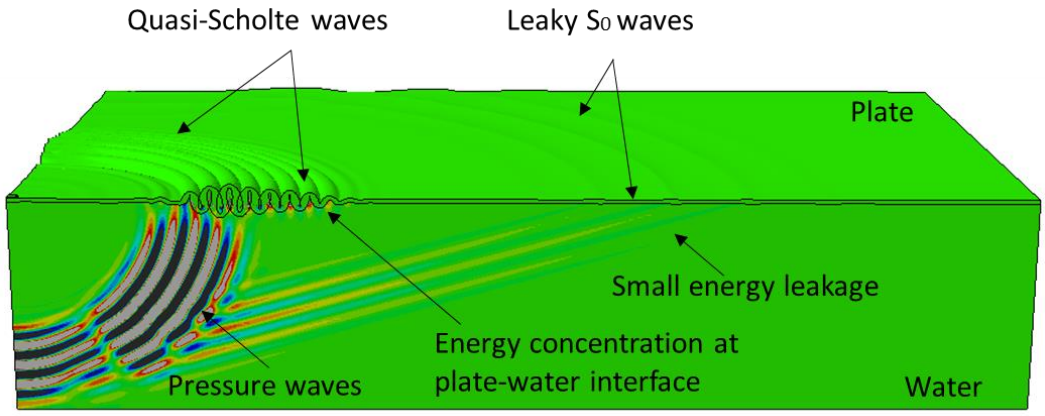

Figure 4.8. Snapshot of the simulation results at 72 μs

4.5.2. Experimental validation of the FE model

In this section, the 3D FE model is validated by comparing the simulation results with the experimental data. The simulations carried out using the 3D FE model with the VUMAT subroutine are labeled as nonlinear FE because the material nonlinearity was modeled by the Murnaghan strain energy function. Firstly, the linear features of the leaky S_0 waves that were simulated by nonlinear FE and

measured from experiments were investigated and compared. From both the experiments and the nonlinear simulations, the out-of-plane displacements were obtained at 21 measurement points along a line from 200 mm to 300 mm away from the excitation center. Figure 4.9(a) shows the signal simulated by the nonlinear FE. The measurement point was 200 mm away from the excitation center. Figure 4.9(b) compares the waveforms of the window-cut signals obtained from the experiments and the simulations from the nonlinear FE at the same measurement point. The amplitudes are normalized by the maximum peak magnitudes of the signals. In general, the nonlinear FE well predicts the waveform and the time of arrival of leaky S_0 waves.

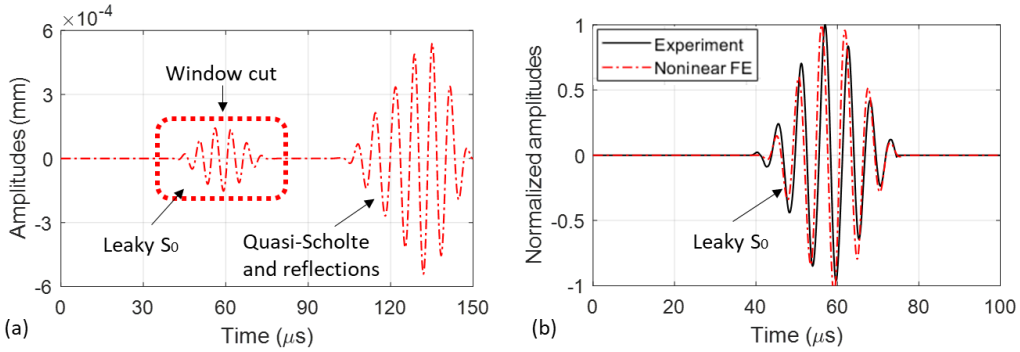

Figure 4.9. (a) Signal simulated by the nonlinear FE (b) Comparison of the window-cut signals measured from the experiment and simulated by the nonlinear FE.

To further validate the accuracy of the nonlinear FE, the group and phase velocities were calculated using the simulated signals, and the simulation results were compared with theoretical values and experiment data. The excitation frequency was swept from 150 kHz to 390 kHz in steps of 20 kHz. The signals were collected at the first 10 points for each excitation frequency to calculate the averaged phase and group velocities. The distance between the two consecutive measurement points was 5 mm and it was less than half of the wavelength of the selected leaky S_0 wave. The phase velocity C_p was calculated by $C_p(f_c) = 2\pi f_c \Delta\phi/\Delta x$, where f_c represents the central frequency of the excitation.

$\Delta\phi$ and Δx are the phase difference and the distance between the two measurement points, respectively. The group velocity C_g was calculated by $C_g(f_c) = \Delta x/\Delta t$, where Δt is the time lag between the two measurement points.

Figures 4.10(a) and 4.10(b) present the phase velocity and group velocity dispersion curves for the aluminum plate loaded with water on the single side, respectively. In both figures, there are three wave modes represented by three lines, which are calculated based on the global matrix theory by the commercial software DISPERSE [65]. The black solid lines on the top represent the leaky S_0 mode. The values calculated by the experimental data and the nonlinear FE simulations are denoted by cycles and stars, respectively. It can be seen that the simulation results have a good agreement with the theoretical derivations and experimental measurements. The maximum deviation is less than 2%.

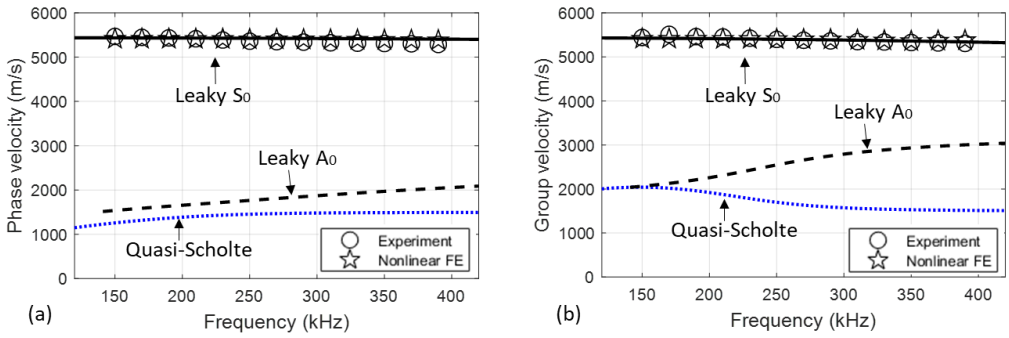

Figure 4.10. (a) Phase velocity dispersion curves and (b) group velocity dispersion curves calculated by the theoretical derivations (black solid line, black dashed line, and blue dotted line), nonlinear finite element simulations (stars), and experimental measurements (circles)

Then, the nonlinear features of the simulated and experimentally measured leaky S_0 waves were analyzed. The simulations were carried out using the 3D FE model with and without the VUMAT subroutine. The simulations, solved using only the linear elastic material properties as shown in Table 4.1, are labeled as linear FE because they do not consider the inherent material nonlinearity. The nonlinear

FE simulates the material nonlinearity of the aluminum plate by introducing the Murnaghan constants of zero fatigue damage in Table 4.2. Figure 4.11(a) compares the window-cut signals obtained from the experimental measurements and the simulated signals from both the linear and nonlinear FE models. The amplitudes are normalized by their corresponding peak magnitudes. The simulated linear and nonlinear signals do not show much difference in the time domain, and both have a good agreement with the experimental data. Figure 4.11(b) shows the corresponding data in the frequency domain. It can be seen that nonlinear FE captures the second harmonics at twice the excitation frequency, as highlighted by the black dotted lines in the figure. In general, the second harmonics simulated by the nonlinear FE have a good agreement with the experimental data (see the red dash-dotted line and black solid line in Figure 4.11(b)). However, the linear FE that uses only the second-order elastic constants could only predict the primary waves as shown by the blue dashed lines. The second harmonics are not observable in the linear FE. The comparison between the linear and nonlinear FE further confirms that the generated second harmonics are due to the material nonlinearity by considering the Murnaghan strain energy function and Murnaghan constants.

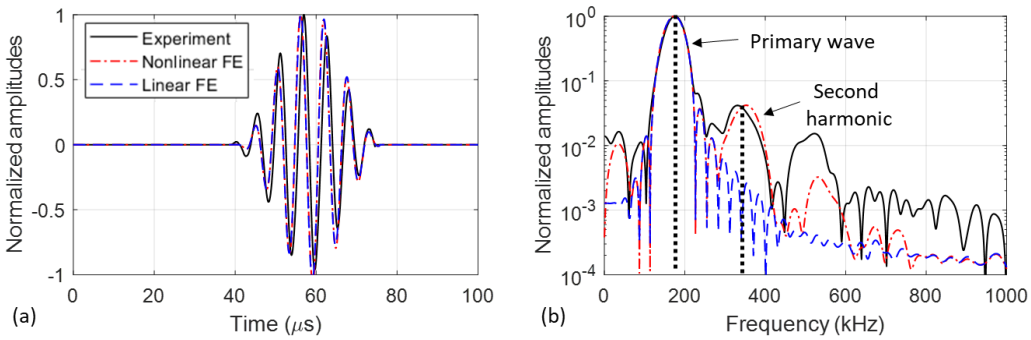

Figure 4.11. (a) Comparison of the time domain signals obtained from the experimental measurement, linear finite element simulation, and nonlinear finite element simulation; and (b) their corresponding frequency spectra.

It should be noted that the Murnaghan strain energy function, incorporating the third-order approximation of the constitutive relation, could be used to predict

the generation of only up to the second harmonics. To study the third-order harmonics, the fourth-order expansion of the constitutive relation and fourth-order elastic material constants should be included in the constitutive model [60]. This explains why the nonlinear FE is unable to capture the peak located at three times the excitation frequency. Since this study focuses on the generation of the second harmonics, the Murnaghan strain energy function is sufficient for analysis. Therefore, the simulation results are validated.

4.5.3. Second harmonic generation in the submerged plate at different levels of fatigue damage

The experimentally validated 3D FE model was employed to explore the influence of evenly distributed fatigue damage on the generation of the second harmonics. Stobbe [54] experimentally measured the values of Murnaghan constants for aluminum at different fatigue levels. In his experimental studies, a series of dog-bone samples made of aluminum were fatigued by repeated uniaxial tensile loads. One sample was loaded to 52800 load cycles and failed, which was defined as 100% fatigue damage. The rest samples were then fatigued to different cycles and were referenced to different percentages of fatigue damage. The numerical simulations in the present study employed the experimentally measured Murnaghan constants for the undamaged aluminum and the aluminum at 40% and 80% fatigue damage [54], as shown in Table 4.2. They have been used in previous studies to simulate the generation of nonlinear guided waves in aluminum plates [59] and pipes [64] in gaseous environments. For the first time, this paper presents the numerical simulations of an aluminum plate with one side loaded with water and the sensitivity of the second harmonics generated by leaky S_0 waves to fatigue damage is investigated. Three simulations were carried out using the experimentally validated 3D FE model with three different sets of Murnaghan constants (see Table 4.2), which represent the aluminum plates at 0%, 40%, and 80% fatigue damage. The other settings remained unchanged.

The simulated out-of-plane displacements were obtained at 21 points from 200 mm to 300 mm away from the excitation center to calculate β'. For direct comparison, the values are normalized by the initial value at 200 mm for the

aluminum plate at zero fatigue damage. Figure 4.12(a) presents the normalized nonlinear parameters versus the propagation distance. It can be seen that the normalized nonlinearity parameters increase linearly with the propagation distance for the three cases. In addition, the slopes of the best-fit lines increase with the fatigue damage levels.

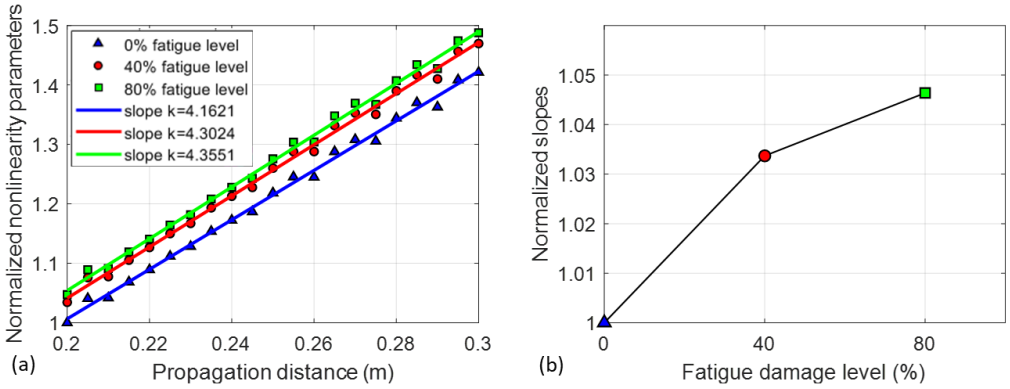

Figure 4.12 (a) The normalized nonlinearity parameters versus propagation distance and (b) normalized slopes of the best-fit lines at different levels of fatigue damage

Figure 4.12(b) compares the slopes of the best fit lines at different levels of fatigue damage. The values are normalized by the initial value at zero fatigue damage. As mentioned in Section 4.3.1, the material nonlinearity can be evaluated by the gradient of accumulation of β'. Thus, it shows that material nonlinearity increases quickly during the initial stage of fatigue damage and the increasing rate becomes much slower after 40% fatigue damage. This behavior is in agreement with the preceding studies on fatigue damage evaluation by longitudinal waves [66, 67], Rayleigh waves [68, 69], and Lamb waves [33, 44, 70]. Therefore, the numerical simulations reveal that second harmonics generated by the low-attenuation leaky S_0 waves have the potential to characterize the material nonlinearity of the plate when one side of the plate is exposed to water.

4.5.4. Comparison between the free plate and water-immersed plate

The experimentally validated 3D FE model was also employed to explore the influence of the surrounding liquid on the generation of the second harmonics. Two simulations were carried out for the undamaged aluminum plate with and without the water layer, respectively. The simulation for the plate without the water layer is labeled as the free plate, while that for the plate with one side exposed to water is labeled as the water-immersed plate. The other settings remained the same.

Guided waves that propagate in the free plate are called Lamb waves, which consist of multiple symmetric and antisymmetric Lamb wave modes. Figure 4.13(a) shows the simulated signals for the free plate. The first wave packet is identified as the fundamental symmetric Lamb (S_0) mode that propagates fastest in the selected excitation frequency. The second wave packet that arrives around 80 μs is the fundamental antisymmetric Lamb (A_0) mode. It propagates slightly faster than the quasi-Scholte wave as shown in Figure 4.9(a). Figure 4.13(b) compares the window-cut signals for the free plate and water-immersed plate, respectively. Their corresponding frequency spectra are shown in Figure 4.13(c). The amplitudes are normalized by the corresponding peak magnitudes for comparison. It can be seen that the leaky S_0 wave has a similar waveform as the S_0 wave in the time domain due to the fact that they have similar group and phase velocities [71, 72]. However, the ratios of the second harmonics to the primary waves are smaller for the leaky S_0 wave compared to that of the S_0 wave. This is because the attenuation of the leaky S_0 wave gradually increases with the frequency as discussed in Section 4.3.2. This phenomenon also has a significant influence on the growing trends of the nonlinearity parameters as shown in Figure 4.13(d). The slope of the best-fit line of the free plate is 7.0876, which is nearly double the value of the one-side water-immersed plate. Thus, the simulation results reveal that the surrounding liquid can reduce the accumulation rate of the nonlinearity parameters. In addition, the influence of water is much stronger than that caused by fatigue damage as discussed in Section 4.5.3. So, the liquid coupling effects should be considered when the nonlinear guided wave techniques are used for damage detection for the immersed plate structures.

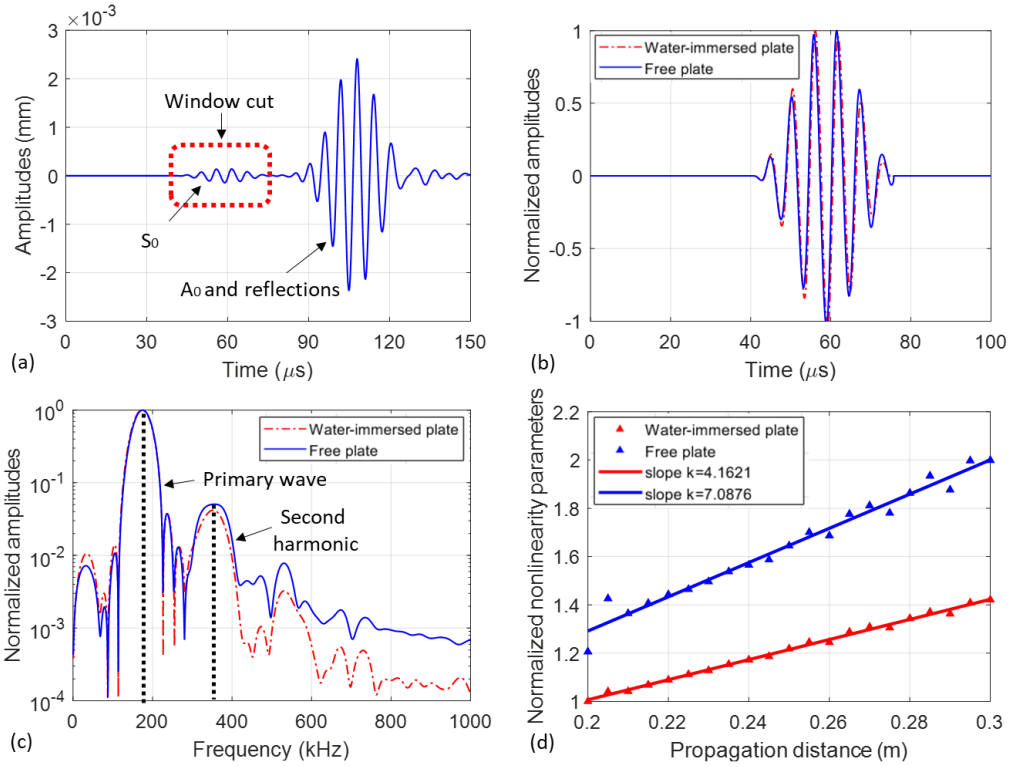

Figure 4.13 (a) Signal simulated by the free plate FE; (b) Comparison of the window-cut signals simulated by the free plate FE and water-immersed plate FE; (c) frequency spectra of the signals in (b), and (d) comparison of the normalized nonlinearity parameters versus propagation distance.

4.6. Conclusion

This paper has investigated experimentally and numerically the second harmonic generation by guided waves in plates immersed in liquid on one side, which has the potential to characterize the microstructural evolution before the appearance of macroscale damage and fraction. The findings can provide support for the further development of NDT techniques for partially submerged structures, such as nuclear cooling pipes, pressure vessels, rocket fuel tanks, storage tanks, and submarine hulls. Earlier damage detection of these partially immersed structures allows more time to schedule the maintenance actions and reduces the risks of in-service failure.

Firstly, the dispersion behavior of guided waves has been analyzed for metallic plates with one side immersed in water. It has been found that the leaky S_0 mode at low frequencies has low attenuation and low dispersion features. This

analysis leads to the selection of leaky S_0 to generate second harmonics of the same type of wave mode in the one-side water-immersed plate because the primary and second harmonic leaky S_0 waves satisfy approximate phase velocity matching and non-zero power flux conditions. Next, experimental studies have been conducted on the metal tank filled with water. A case study using experimentally measured signals at the excitation frequency of 170 kHz has been presented. Both the primary and second harmonic leaky S_0 waves can be identified in the frequency spectrums. In addition, the relative nonlinearity parameter β' has been calculated and shown to grow linearly with the propagation distance. The experimental results confirm that leaky S_0 waves can generate measurable second harmonics due to the material nonlinearity of the one-side water-immersed plate. After that, numerical simulations have been carried out using a 3D FE model and validated through experimental measurements. The experimentally validated 3D FE model has been employed in parametric studies to explore the second harmonic generation in the one-side water-immersed plate at different levels of fatigue damage. The results have shown that the second harmonic generation techniques are promising for non-destructively evaluating microstructural defects in plate structures with one side immersed in liquid.

The present study only demonstrates that the interaction between guided waves and microstructural features of partially immersed plates can generate measurable and low-attenuation second harmonics. When the microscopic defects grow into macro scale, there can be a substantial increase in amplitudes for the nonlinear guided waves due to the clapping behavior between the surfaces as the primary guided waves pass through. For the structures in gaseous environments, the clapping effect of macro cracks is classified as contact-type nonlinearity, which has been demonstrated to generate second harmonics with much larger amplitudes than the material nonlinearity [28, 37]. Future studies can investigate the effect of the size, shape, and location of macro cracks (e.g. stress corrosion cracking) on the nonlinear guided wave features for the structures immersed in liquid.

4.7. Acknowledgments

This research was funded by the Australian Research Council, grant number DP200102300 and DP210103007. The support is greatly appreciated.

4.8. References

[1] S.E. Hirdaris, W. Bai, D. Dessi, A. Ergin, X. Gu, O.A. Hermundstad, R. Huijsmans, K. Iijima, U.D. Nielsen, J. Parunov, N. Fonseca, A. Papanikolaou, K. Argyriadis, A. Incecik, Loads for use in the design of ships and offshore structures, Ocean Engineering, 78 (2014) 131-174.

[2] B. Thirunavukkarasu, T.K.R. Rajagopal, Numerical investigation of sloshing in tank with horivert baffles under resonant excitation using CFD code, Thin-Walled Structures, 161 (2021) 107517.

[3] M.M. Shabani, A. Taheri, M. Daghigh, Reliability assessment of free spanning subsea pipeline, Thin-Walled Structures, 120 (2017) 116-123.

[4] A. Adamkowski, M. Lewandowski, S. Lewandowski, Fatigue life analysis of hydropower pipelines using the analytical model of stress concentration in welded joints with angular distortions and considering the influence of water hammer damping, Thin-Walled Structures, 159 (2021) 107350.

[5] Kawagoishi, Chen, Nisitani, Fatigue strength of Inconel 718 at elevated temperatures, Fatigue & Fracture of Engineering Materials & Structures, 23 (2000) 209-216.

[6] Y. Xiang, M. Deng, C.-J. Liu, F.-Z. Xuan, Contribution of mixed dislocations to the acoustic nonlinearity in plastically deformed materials, Journal of Applied Physics, 117 (2015) 214903.

[7] C.J. Lissenden, Nonlinear ultrasonic guided waves—Principles for nondestructive evaluation, Journal of Applied Physics, 129 (2021) 021101.

[8] M. Jimenez-Martinez, Fatigue of offshore structures: A review of statistical fatigue damage assessment for stochastic loadings, International Journal of Fatigue, 132 (2020) 105327.

[9] Z. Zhang, L. Guo, Y.F. Cheng, Interaction between internal and external defects on pipelines and its effect on failure pressure, Thin-Walled Structures, 159 (2021) 107230.

[10] L. Christensen, N. Fischer, S. Kroffke, J. Lemburg, R. Ahlers, Cost-effective autonomous robots for ballast water tank inspection, Journal of ship production and design, 27 (2011) 127.

[11] B.A. Zárate, A. Pollock, S. Momeni, O. Ley, Structural health monitoring of liquid-filled tanks: a Bayesian approach for location of acoustic emission sources, Smart Materials and Structures, 24 (2014) 015017.

[12] C. Mukhopadhyay, T. Haneef, T. Jayakumar, G. Sharma, B. Rao, Structural integrity assessment of H2S storage tanks using acoustic emission and ultrasonic techniques, International Journal of Structural Integrity, (2015).

[13] M. Hassanzadeh, K. Rahmani, Hydrostatic test of storage tanks using seawater and corrosion considerations, Engineering Failure Analysis, 122 (2021) 105267.

[14] L. Peng, S. Huang, S. Wang, W. Zhao, Three-dimensional magnetic flux leakage signal analysis and imaging method for tank floor defect, The Journal of Engineering, 2018 (2018) 1865-1870.

[15] M. Grosso, C.J. Pacheco, M.P. Arenas, A.H.M. Lima, I.C.P. Margarit-Mattos, S.D. Soares, G.R. Pereira, Eddy current and inspection of coatings for storage tanks, Journal of Materials Research and Technology, 7 (2018) 356-360.

[16] H. Mohseni, C.-T. Ng, Rayleigh wave propagation and scattering characteristics at debondings in fibre-reinforced polymer-retrofitted concrete structures, Structural Health Monitoring, 18 (2019) 303-317.

[17] J.M. Hughes, M. Mohabuth, A. Khanna, J. Vidler, A. Kotousov, C.-T. Ng, Damage detection with the fundamental mode of edge waves, Structural Health Monitoring, 20 (2021) 74-83.

[18] Y. Wang, H. Wu, F. Yang, Q. Wang, An efficient method for vibration and stability analysis of rectangular plates axially moving in fluid, Applied Mathematics and Mechanics, 42 (2021) 291-308.

[19] A.E. Takiy, C. Kitano, R.T. Higuti, S.C.G. Granja, V.T. Prado, L. Elvira, O. Martínez-Graullera, Ultrasound imaging of immersed plates using high-order Lamb modes at their low attenuation frequency bands, Mechanical Systems and Signal Processing, 96 (2017) 321-332.

[20] S. Tietze, G. Lindner, Visualization of the interaction of guided acoustic waves with water by light refractive vibrometry, Ultrasonics, 99 (2019) 105955.

[21] M. Santos, J. Perdigao, Leaky Lamb waves for the detection and sizing of defects in bonded aluminium lap joints, NDT & E International, 38 (2005) 561-568.

[22] J. Chen, Z. Su, L. Cheng, Identification of corrosion damage in submerged structures using fundamental anti-symmetric Lamb waves, Smart Materials and Structures, 19 (2009) 015004.

[23] P. Rizzo, E. Pistone, P. Werntges, J. Han, X. Ni, Inspection of underwater metallic plates by means of laser ultrasound, Nondestructive Testing of Materials and Structures, Springer, 2013, pp. 675-680.

[24] S. Sharma, A. Mukherjee, Damage detection in submerged plates using ultrasonic guided waves, Sadhana, 39 (2014) 1009-1034.

[25] S. Sharma, A. Mukherjee, Ultrasonic guided waves for monitoring corrosion in submerged plates, Structural Control and Health Monitoring, 22 (2015) 19-35.

[26] Q. Xie, C. Ni, Z. Shen, Defects detection and localization in underwater plates using laser laterally generated pure non-dispersive S0 mode, Applied Sciences, 9 (2019) 459.

[27] K.-Y. Jhang, Nonlinear ultrasonic techniques for nondestructive assessment of micro damage in material: A review, International Journal of Precision Engineering and Manufacturing, 10 (2009) 123-135.

[28] S. He, C.-T. Ng, C. Yeung, Time-domain spectral finite element method for modeling second harmonic generation of guided waves induced by material, geometric and contact nonlinearities in beams, International Journal of Structural Stability and Dynamics, 20 (2020) 2042005.

[29] C.J. Lissenden, Y. Liu, G.W. Choi, X. Yao, Effect of localized microstructure evolution on higher harmonic generation of guided waves, Journal of Nondestructive Evaluation, 33 (2014) 178-186.

[30] V.K. Chillara, C.J. Lissenden, Review of nonlinear ultrasonic guided wave nondestructive evaluation: theory, numerics, and experiments, Optical Engineering, 55 (2015) 011002.

[31] C. Pruell, J.Y. Kim, J. Qu, L.J. Jacobs, A nonlinear-guided wave technique for evaluating plasticity-driven material damage in a metal plate, NDT & E International, 42 (2009) 199-203.

[32] J. Herrmann, J.-Y. Kim, L.J. Jacobs, J. Qu, J.W. Littles, M.F. Savage, Assessment of material damage in a nickel-base superalloy using nonlinear Rayleigh surface waves, Journal of Applied Physics, 99 (2006) 124913.

[33] W. Li, Y. Cho, J.D. Achenbach, Detection of thermal fatigue in composites by second harmonic Lamb waves, Smart Materials and Structures, 21 (2012) 085019.

[34] A. Ruiz, N. Ortiz, A. Medina, J.-Y. Kim, L. Jacobs, Application of ultrasonic methods for early detection of thermal damage in 2205 duplex stainless steel, NDT & E International, 54 (2013) 19-26.

[35] K.H. Matlack, H.A. Bradley, S. Thiele, J.-Y. Kim, J.J. Wall, H.J. Jung, J. Qu, L.J. Jacobs, Nonlinear ultrasonic characterization of precipitation in 17-4PH stainless steel, NDT & E International, 71 (2015) 8-15.

[36] C. Zhou, M. Hong, Z. Su, Q. Wang, L. Cheng, Evaluation of fatigue cracks using nonlinearities of acousto-ultrasonic waves acquired by an active sensor network, Smart Materials and Structures, 22 (2012) 015018.

[37] M. Hong, Z. Su, Q. Wang, L. Cheng, X. Qing, Modeling nonlinearities of ultrasonic waves for fatigue damage characterization: Theory, simulation, and experimental validation, Ultrasonics, 54 (2014) 770-778.

[38] Y. Yang, C.-T. Ng, A. Kotousov, H. Sohn, H.J. Lim, Second harmonic generation at fatigue cracks by low-frequency Lamb waves: Experimental and numerical studies, Mechanical Systems and Signal Processing, 99 (2018) 760-773.

[39] A. Aseem, C.T. Ng, Debonding detection in rebar-reinforced concrete structures using second harmonic generation of longitudinal guided wave, NDT & E International, (2021) 102496.

[40] J.C. Pineda Allen, C.T. Ng, Nonlinear guided-wave mixing for condition monitoring of bolted joints, Sensors, 21 (2021) 5093.

[41] K.-Y. Jhang, C.J. Lissenden, I. Solodov, Y. Ohara, V. Gusev, Measurement of nonlinear ultrasonic characteristics, Springer, 2020.

[42] M. Deng, Cumulative second-harmonic generation of Lamb-mode propagation in a solid plate, Journal of applied physics, 85 (1999) 3051-3058.

[43] M. Deng, Analysis of second-harmonic generation of Lamb modes using a modal analysis approach, Journal of applied physics, 94 (2003) 4152-4159.

[44] W. Zhu, Y. Xiang, C.-j. Liu, M. Deng, C. Ma, F.-z. Xuan, Fatigue damage evaluation using nonlinear Lamb Waves with Quasi phase-velocity matching at low frequency, Materials, 11 (2018) 1920.

[45] W. De Lima, M. Hamilton, Finite-amplitude waves in isotropic elastic plates, Journal of sound and vibration, 265 (2003) 819-839.

[46] V.K. Chillara, C.J. Lissenden, Interaction of guided wave modes in isotropic weakly nonlinear elastic plates: Higher harmonic generation, Journal of Applied Physics, 111 (2012) 124909.

[47] N. Matsuda, S. Biwa, Phase and group velocity matching for cumulative harmonic generation in Lamb waves, Journal of Applied Physics, 109 (2011) 094903.

[48] D. Wang, L. Wu, Y. Zhu, X. Wang, Y. Li, Vibration of a plate coupled with fluid considering the effects of stress and deformation under hydrostatic load, Thin-Walled Structures, 145 (2019) 106413.

[49] L. Yu, Z. Tian, Case study of guided wave propagation in a one-side water-immersed steel plate, Case Studies in Nondestructive Testing and Evaluation, 3 (2015) 1-8.

[50] Y.Q. Wang, X.B. Huang, J. Li, Hydroelastic dynamic analysis of axially moving plates in continuous hot-dip galvanizing process, International Journal of Mechanical Sciences, 110 (2016) 201-216.

[51] X. Hu, C.-T. Ng, A. Kotousov, Ultrasonic guided wave field modeling in a one-side water-immersed steel plate, in: Lecture Notes in Civil Engineering, 2021, pp. 1131-1140.

[52] X. Hu, C.-T. Ng, A. Kotousov, Nonlinear guided waves generated by leaky S0 waves in submerged plates, 10th International Conference on Structrual Health Monitoring of Intelligent Infrastructure (SHMII-10) Porto, Portugal, 2021.

[53] X. Hu, C.-T. Ng, A. Kotousov, Experimental investigations on second harmonics generated by leaky guided waves in immersed plates, 10th Australian Congress on Applied Mechanics, 2021.

[54] D.M. Stobbe, Acoustoelasticity in 7075-T651 aluminum and dependence of third order elastic constants on fatigue damage, in, Georgia Institute of Technology, 2005.

[55] J.M. Hughes, J. Vidler, C.-T. Ng, A. Khanna, M. Mohabuth, L.F. Rose, A. Kotousov, Comparative evaluation of in situ stress monitoring with Rayleigh waves, Structural Health Monitoring, 18 (2019) 205-215.

[56] J.M. Hughes, A. Kotousov, C.-T. Ng, Generation of higher harmonics with the fundamental edge wave mode, Applied Physics Letters, 116 (2020) 101904.

[57] P. Guo, B. Deng, X. Lan, K. Zhang, H. Li, Z. Tian, H. Xu, Water level sensing in a steel vessel using A0 and Quasi-Scholte waves, Journal of Sensors, 2017 (2017).

[58] X. Hu, C.-T. Ng, A. Kotousov, Scattering characteristics of quasi-Scholte waves at blind holes in metallic plates with one side exposed to water, NDT & E International, 117 (2021) 102379.

[59] X. Wan, P. Tse, G. Xu, T. Tao, Q. Zhang, Analytical and numerical studies of approximate phase velocity matching based nonlinear S0 mode Lamb waves for the detection of evenly distributed microstructural changes, Smart Materials and Structures, 25 (2016) 045023.

[60] V.K. Chillara, C.J. Lissenden, Constitutive model for third harmonic generation in elastic solids, International Journal of Non-Linear Mechanics, 82 (2016) 69-74.

[61] J. Chen, Z. Su, L. Cheng, The medium coupling effect on propagation of guided waves in engineering structures and human bone phantoms, Coupled systems mechanics, (2012).

[62] Y. Yang, C.-T. Ng, A. Kotousov, Second-order harmonic generation of Lamb wave in prestressed plates, Journal of Sound and Vibration, 460 (2019) 114903.

[63] V.K. Chillara, C.J. Lissenden, Nonlinear guided waves in plates: a numerical perspective, Ultrasonics, 54 (2014) 1553-1558.

[64] C. Yeung, C.T. Ng, Nonlinear guided wave mixing in pipes for detection of material nonlinearity, Journal of Sound and Vibration, 485 (2020) 115541.

[65] B. Pavlakovic, M. Lowe, Disperse user manual: a system for generating dispersion curves, Copyright B Pavlakovic, M Lowe, (2003).

[66] J.H. Cantrell, W.T. Yost, Nonlinear ultrasonic characterization of fatigue microstructures, International Journal of Fatigue, 23 (2001) 487-490.

[67] J.-Y. Kim, L.J. Jacobs, J. Qu, J.W. Littles, Experimental characterization of fatigue damage in a nickel-base superalloy using nonlinear ultrasonic waves, The Journal of the Acoustical Society of America, 120 (2006) 1266-1273.

[68] D. Barnard, L. Brasche, D. Raulerson, A. Degtyar, Monitoring fatigue damage accumulation with Rayleigh wave harmonic generation measurements, in: AIP Conference Proceedings, AIP, 2003, pp. 1393-1400.

[69] S.V. Walker, J.-Y. Kim, J. Qu, L.J. Jacobs, Fatigue damage evaluation in A36 steel using nonlinear Rayleigh surface waves, NDT & E International, 48 (2012) 10-15.

[70] C. Pruell, J.-Y. Kim, J. Qu, L.J. Jacobs, Evaluation of fatigue damage using nonlinear guided waves, Smart Materials and Structures, 18 (2009) 035003.

[71] X. Hu, C.-T. Ng, A. Kotousov, Numerical and experimental investigations on mode conversion of guided waves in partially immersed plates, Measurement, (2022) 110750.

[72] X. Hu, C.-T. Ng, A. Kotousov, Damage detection of partially immersed plates using guided waves, Recent Advances in Structural Health Monitoring Research in Australia, Nova Science Publishers Inc., 2021.

Chapter 5. Structural health monitoring of partially immersed metallic plates using nonlinear guided wave mixing

Abstract

Metallic plates are important structural components of many liquid containment structures, such as liquid storage tanks and sewer pipes. Time-dependent loads can result in fatigue and degradation of the metallic material. Nonlinear guided wave mixing has been demonstrated to be sensitive to microstructural change at the early stage of material degradation. Previous studies have been carried out using the nonlinear guided wave mixing technique on various structures in gaseous environments. However, its application to structures immersed in liquid has not been explored. This paper numerically and experimentally investigates the nonlinear guided wave mixing in an aluminum plate loaded with water on one side. Experiments are carried out with an empty metal tank and the tank filled with water, respectively. The results show that cumulative generation of harmonics at the sum frequency due to the material nonlinearity of the partially immersed plate can be achieved by mixing the fundamental leaky symmetrical Lamb (leaky S_0) waves at two different frequencies. Under the same experimental conditions, the amplitudes of the guided wave signals and the values of the relative nonlinearity parameters on the partially immersed plate are different from their counterparts on the plate without water. Finally, numerical simulations are performed with the material nonlinearity of the test plate simulated by the Murnaghan constitutive model. The numerical results reveal that both the second harmonics and the combination harmonics are sensitive to the material nonlinearity of the plate loaded with water on one side.

Keywords: Structural health monitoring; Water containment structures; Metallic plates; Leaky Lamb waves; Nonlinear guided waves; Guided wave mixing; Second harmonics

Statement of Authorship

Title of Paper	Structural health monitoring of partially immersed metallic plates using nonlinear guided wave mixing
Publication Status	☐ Published ☑ Accepted for Publication ☐ Submitted for Publication ☐ Unpublished and Unsubmitted w ork w ritten in manuscript style
Publication Details	X. Hu, T. Yin, H. Zhu, C.T. Ng, A. Kotousov, (2022). Structural health monitoring of partially immersed metallic plates using nonlinear guided wave mixing. *Construction and Building Materials* (In-print).

Principal Author

Name of Principal Author (Candidate)	Xianwen Hu		
Contribution to the Paper	Conceptualization, Developing and validating numerical models, Conducting experimental measurements, Signal processing and data analysis, Writing the original draft and editing.		
Overall percentage (%)	80%		
Certification:	This paper reports on original research I conducted during the period of my Higher Degree by Research candidature and is not subject to any obligations or contractual agreements with a third party that would constrain its inclusion in this thesis. I am the primary author of this paper.		
Signature		Date	07/03/2022

Co-Author Contributions

By signing the Statement of Authorship, each author certifies that:

i. the candidate's stated contribution to the publication is accurate (as detailed above);

ii. permission is granted for the candidate in include the publication in the thesis; and

iii. the sum of all co-author contributions is equal to 100% less the candidate's stated contribution.

Name of Co-Author	Tingyuan Yin		
Contribution to the Paper	Analytical derivations, Writing – review & editing.		
Signature		Date	07/03/2022

Name of Co-Author	Hankai Zhu		
Contribution to the Paper	Experimental measurements, Writing – review & editing.		
Signature		Date	07/03/2022

Name of Co-Author	Ching-Tai Ng		
Contribution to the Paper	Supervision, writing – review & editing		
Signature		Date	9/3/2022

Name of Co-Author	Andrei Kotousov		
Contribution to the Paper	Supervision, writing – review & editing		
Signature		Date	07/03/2022

Please cut and paste additional co-author panels here as required.

5.2. Introduction

Metallic plates are commonly used for constructing undersea tunnels [1], storage tanks [2], sewer pipes [3], and containment buildings [4]. These structures have one side immersed in liquid and are subjected to cyclic loads with varying amplitudes. Material degradation and fatigue are the primary culprits for the failure of these partially immersed metallic structures [5]. In the early damage stage, dislocations and slip bands occur in the materials and then micro cracks are formed. With the increase in loading cycles, the micro cracks continue to accumulate and grow to a critical point, which can cause catastrophic failures [6, 7]. Continuous evaluation of material properties of partially immersed metallic plates is crucial to maintain the structural integrity of high-valued infrastructures.

Guided wave testing is a non-destructive inspection technique that has attracted extensive research interest. It outperforms other non-destructive testing methods, such as eddy current testing, acoustic emission, and conventional ultrasonic testing, because guided waves can travel relatively long distances on various structures and have a high sensitivity to different kinds of damage [8]. The structural health can be monitored by both linear and nonlinear features of guided waves. Conventional guided wave testing is based on linear features. Specifically, the presence of defects changes the transmitted guided wave signals, typified as scattering, mode conversion, attenuation, and change in wave velocity. Linear guided wave testing was successfully applied to immersed structures to characterize cracks [9], pits [10], notches [11], and corrosion [12, 13]. In these studies, guided waves in immersed structures were shown to behave differently from their counterparts in structures without exposure to liquid. In addition, the sizes of the defects were around a few millimeters, which were comparable to the wavelength of the selected guided wave modes. However, linear guided waves are insensitive to smaller defects such as micro cracks and dislocations in the early damage stage. When the micro cracks evolve into macro cracks and become identifiable through the linear guided wave features, the metallic structures, in many cases, reach more than 80% of its total service life [14].

Recent studies have focused on the nonlinear features of guided waves, which provide much better sensitivity than the linear features in detecting

microstructural defects that precede the macro-scale damage [15]. The second harmonic approach is one of the most popular nonlinear guided wave methods. When the structural material is excited by guided waves with finite amplitudes, the ultrasonic guided wave energy can be transferred from the excitation frequency to twice the excitation frequency due to the interaction of the primary guided waves with the microstructural features of the material. This phenomenon provides a way to identify and characterize material degradation at its early stage. For example, the second harmonics generated by guided waves were used to evaluate the evolution of thermal aging [16, 17] and fatigue [18, 19] for metallic plates in gaseous environments. A comprehensive review of the second harmonic guided wave approach can be found in [15]. The major difficulty hindering the applications of second harmonics is that the instrumentation of the measurement system can also produce nonlinear signals at the integer multiples of the excitation frequency [20, 21]. It is difficult to distinguish the nonlinearity due to the material from the nonlinearity caused by the instruments.

To tackle this limitation of the second harmonic approach, a number of researchers proposed the nonlinear guided wave mixing technique, in which the structural material is excited by guided waves with two different frequencies. Hasanian and Lissenden [22] conducted a wave vector analysis for the mutual interaction of two guided waves with different frequencies. The mutual interaction can generate combination harmonics at the sum and difference frequencies that are far from the nonlinear waves produced by the instrumentation. Hasanian and Lissenden [23] further studied the internal resonance criteria for the non-collinear guided wave interaction, where the guided waves propagate in different directions and meet in a localized mixing zone. They concluded that the amplitudes of the generated combination harmonics are dependent on the size of the wave mixing areas. Jiao et al [24] demonstrated both experimentally and numerically that the combination harmonics of guided waves at the sum frequency are sensitive to micro cracks in metallic plates. Metya et al [25] revealed that the nonlinear guided wave mixing technique can also evaluate localized deformation of a steel plate during creep. Shan et al [26] mixed two shear horizontal waves that propagated in the same direction to generate cumulative combination harmonics at the sum frequency. The combination harmonics demonstrated a high sensitivity to degradation of the

aluminum plate during early fatigue stages. Cho et al [27] proposed a novel technique to detect localized fatigue damage in aluminum plates by the interaction of two counter-propagating shear horizontal waves. The wave mixing area can be controlled and moved to different locations on the sample by adjusting the time delays of the input signals. Thus, the whole area of the plate can be scanned. Li et al [28] employed the guided wave mixing and mixing frequency peak counting techniques to assess low-velocity impact damage in CFRP composite laminates. The value of the mixing frequency peak count could be correlated with the impact energy in the test. Guan et al [29] developed a three-dimension (3D) finite element (FE) model to demonstrate that the directions and locations of the micro cracks in plates can affect the amplitudes of the nonlinear waves generated by nonlinear guided wave mixing. All the aforementioned studies demonstrated that the guided wave mixing technique has many advantages over the second harmonic approach. One of the most important merits is that the combination harmonics generated by mixing two guided waves are less affected by the higher harmonics produced by the instrumentations, such as amplifiers and transducers. In addition, mutual interaction between guided waves propagating in different directions provides more flexibility for the selection of guided wave modes and their corresponding excitation frequencies.

The majority of the work on nonlinear guided waves has focused on the structures in gaseous environments. Before the initiation of macro-scale damage, the material nonlinearity due to the microstructural features is very weak, making the generation and measurement of nonlinear guided waves very challenging. Only a few guided wave modes within limited frequency bandwidths, satisfying the phase velocity matching and non-zero power flux conditions, have the potential to generate cumulative and measurable nonlinear guided waves and can be used to characterize the material nonlinearity [15]. Phase velocity matching refers to that the primary and the corresponding nonlinear guided waves should have the same phase velocity. Non-zero power flux means that there must be nonzero power flow from the primary waves to the nonlinear guided waves. They have been widely recognized as the criteria for selecting guided wave modes and excitation frequencies for the nonlinear guided wave methods for the structures in gaseous environments. When the structures are exposed to liquid, the fluid-solid coupling

allows the guided wave energy to leak from the structures into the surrounding liquid medium. On the immersed structures, the generation and measurement of nonlinear guided waves are more challenging because most of the guided wave modes have higher attenuation [10]. In addition, the fluid-solid coupling makes the guided waves in the immersed structures behave differently from their counterparts in the structures surrounded by air [30-33]. Therefore, a comprehensive investigation is desired for the nonlinear guided waves in the immersed structures.

This paper presents a series of experimental and numerical investigations on the nonlinear guided wave mixing in partially immersed metallic plates. In the experiments, the fundamental leaky symmetric Lamb (leaky S_0) waves are excited at two different frequencies on an aluminum plate, of which one side is exposed to water. The response signals display the combination harmonics at the sum frequency. Next, the amplitudes of the combination harmonics are investigated with varying excitation magnitudes and propagation distances. The effect of the liquid-structure coupling is also explored by comparing the guided wave signals measured from the test plate with and without water. Then, numerical simulations using a 3D FE model are implemented to further investigate the sensitivity of the combination harmonics to the material nonlinearity of the metallic plate partially immersed in water. The findings of this study can provide support for the development of structural health monitoring techniques for metallic liquid containment structures.

The remainder of the paper is organized as follows. Section 5.3 introduces the theoretical background of the mutual interaction of ultrasonic waves in materials with weak nonlinearity. Section 5.4 presents the experimental study, including the overall experimental setup, preliminary tests to select the guided wave modes and excitation frequencies, and the results of the experimental investigations. The numerical study is illustrated in Section 5.5. The 3D FE model is described and validated through experimental measurements. This section also includes a parametric study, in which the experimentally validated 3D FE model is employed to investigate the characteristics of the nonlinear guided wave mixing in materials with different levels of fatigue. Finally, conclusions are drawn in Section 5.6.

5.3. The theoretical background of the wave mixing technique

This section describes the theoretical derivations for the mutual interaction of ultrasonic waves with two different frequencies in nonlinearly elastic materials. The material nonlinearity is small and attributed to the microstructural features such as dislocations, microvoids, and micro cracks. For one-dimensional problems, the stress-strain relationship of the nonlinear elastic material can be expressed as [15]

$$\sigma = E\left(u' + \frac{\beta}{2}(u')^2\right) \tag{5.1}$$

where σ represent the stress. $u' = \partial u/\partial x$ with u and x representing the displacement and the position, respectively. E and β denote the linear elastic modulus and the second order nonlinear parameters, respectively. The quadratic term accounts for the weak nonlinearity of the material, which is ignored in the linear theory.

Considering that two waves with different frequencies (f_1 and f_2, $f_2 > f_1$) travel in the material, the equation of motions can be described as

$$\sigma' = \rho\ddot{u} \tag{5.2}$$

where ρ is the mass density; $\sigma' = \partial\sigma/\partial x$ and $\ddot{u} = \partial^2 u/\partial t^2$; t denotes the time. Substituting Eq (5.1) into Eq (5.2) gives

$$\frac{E}{\rho}\left(u'' + \beta u'u''\right) = \ddot{u} \tag{5.3}$$

where $u'' = \partial^2 u/\partial x^2$. Eq (5.3) can be solved using the perturbation approach with the assumption that the solution form of the total displacements is the sum of the primary waves and the nonlinear waves

$$u = u_P + u_N \tag{5.4}$$

where u_P and u_N represent the primary and nonlinear components of the total displacements, respectively. The primary waves are also called linear waves because they have the same frequencies as the input signals. The nonlinear waves are generated by the interaction of the primary waves with the material nonlinearity.

The amplitude of the nonlinear waves is much smaller than that of the primary waves ($|u_P| \gg |u_N|$). Then, the governing equation can be obtained by substituting Eq (5.4) into Eq (5.3) as follows

$$\frac{E}{\rho}\left(u_P'' + u_N'' + \beta\left(u_P' + u_N'\right)\left(u_P'' + u_N''\right)\right) = \ddot{u}_P + \ddot{u}_N \tag{5.5}$$

Since the amplitudes of the nonlinear waves are very small, the derivatives with respect to u_N can be neglected [15]. Then the governing equation can be further divided into two differential equations as follows.

$$\begin{aligned} \ddot{u}_P - \frac{E}{\rho}u_P'' &= 0 \\ \ddot{u}_N - \frac{E}{\rho}u_N'' &= \frac{E}{\rho}\beta u_P' u_P'' \end{aligned} \tag{5.6}$$

Finally, the solution of the primary waves is

$$u_P = A_{f_1}\cos(w_1 t - k_1 x + \phi_1) + A_{f_2}\cos(w_2 t - k_2 x + \phi_2) \tag{5.7}$$

The primary waves combine the two excitation frequencies f_1 and f_2. A_{f_1} and A_{f_2} are the amplitudes of the primary waves at f_1 and f_2, respectively. w, k, and, ϕ represent the angular frequency, wavenumber, and phase shift, respectively, with the subscripts denoting the first and second frequency components.

The solution of the nonlinear waves at the frequencies other than the excitation frequencies can be written as

$$\begin{aligned} u_N = {} & A_{2f_1}\cos(2w_1 t - 2k_1 x + \phi_1) + A_{2f_2}\cos(2w_2 t - 2k_2 x + \phi_2) \\ & + A_{f_1+f_2}\cos\left(\left(w_1 + w_2\right)t - \left(k_1 + k_2\right)x + \left(\phi_1 + \phi_2\right)\right) \\ & + A_{f_1-f_2}\cos\left(\left(w_1 - w_2\right)t - \left(k_1 - k_2\right)x + \left(\phi_1 - \phi_2\right)\right) \end{aligned} \tag{5.8}$$

where $A_{2f_1} = \beta A_{f_1}^2 k_1^2 x/8$ and $A_{2f_2} = \beta A_{f_2}^2 k_2^2 x/8$ are the amplitudes of the second harmonics at $2f_1$ and $2f_2$, respectively. $A_{f_1+f_2} = \beta A_{f_1} A_{f_2} k_1 k_2 x/4$ is the amplitude of the combination harmonics (sum harmonics) at the sum frequency ($f_1 + f_2$) and $A_{f_1-f_2} = \beta A_{f_1} A_{f_2} k_1 k_2 x/4$ is the amplitude of the combination harmonics (difference harmonics) at the difference frequency ($f_1 - f_2$). Therefore, when the structural

material is excited by waves with two different frequencies, the nonlinear parameters can be estimated as follows

$$\begin{aligned}
\beta_{2f_1} &= \frac{8}{k_1^2}\left(\frac{A_{2f_1}}{A_{f_1}^2}\right)\frac{1}{x} && \text{for the second harmonics at } 2f_1 \\
\beta_{2f_2} &= \frac{8}{k_2^2}\left(\frac{A_{2f_2}}{A_{f_2}^2}\right)\frac{1}{x} && \text{for the second harmonics at } 2f_2 \\
\beta_{f_1+f_2} &= \frac{4}{k_1 k_2}\left(\frac{A_{f_1+f_2}}{A_{f_1}A_{f_2}}\right)\frac{1}{x} && \text{for the sum harmonics at } f_1 + f_2 \\
\beta_{f_2-f_1} &= \frac{4}{k_1 k_2}\left(\frac{A_{f_2-f_1}}{A_{f_1}A_{f_2}}\right)\frac{1}{x} && \text{for the difference harmonics at } f_2 - f_1
\end{aligned} \tag{5.9}$$

It can be seen that when the propagation characteristics of the primary waves do not change (e.g. fixed wavenumber values k_1 and k_2), the material nonlinearity at any location can be correlated to the amplitudes of the primary waves and the nonlinear waves. For simplicity, the material properties can be characterized by relative nonlinearity parameters and they are defined as follows

$$\begin{aligned}
\beta'_{2f_i} &= \frac{A_{2f_i}}{A_{f_i}^2} && \text{for the second harmonics at } 2f_i \\
\beta'_{f_1+f_2} &= \frac{A_{f_1+f_2}}{A_{f_1}A_{f_2}} && \text{for the sum harmonics at } f_1 + f_2 \\
\beta'_{f_2-f_1} &= \frac{A_{f_2-f_1}}{A_{f_1}A_{f_2}} && \text{for the difference harmonics at } f_2 - f_1
\end{aligned} \tag{5.10}$$

where the relative nonlinearity parameter β' is proportional to the second order nonlinear parameter β and the propagation distance x.

The above derivations consider only the simplest case that ultrasonic waves travel in the isotropic material in one direction. However, the relative nonlinearity parameters defined by Eq. (5.10) have been widely recognized to be applicable for characterizing the material nonlinearity of various structures using different guided wave modes. In the literature, there are two popular approaches for evaluating nonlinear elastic properties. The first approach is to excite structures with the input signals of various magnitudes and measure the response signals at a single location

[34-37]. If the measured nonlinear guided waves are generated due to the material nonlinearity, the amplitudes of the second harmonics (A_{2f_i}) should increase linearly with the square of the amplitudes of the corresponding primary waves ($A_{f_i}^2$). In contrast, the amplitudes of the combination harmonics, including the sum harmonics ($A_{f_1+f_2}$) and difference harmonics ($A_{f_2-f_1}$), should have a positive linear relationship with the product of the primary waves at the two excitation frequencies ($A_{f_1} \times A_{f_2}$). The increasing rate of the nonlinear guided wave magnitudes to the corresponding primary waves can be correlated to the material nonlinearity of structures.

The second approach estimates the material nonlinearity by measuring signals at several locations with different propagation distances [26, 38-41]. Based on Eqs (5.9) and (5.10), the relative nonlinearity parameters (β') will grow linearly with the propagation distance, provided that the primary waves have sufficiently large motion magnitudes to interact with the microstructural features of the material [40, 42, 43]. The material's nonlinear elastic properties can be characterized by the accumulation gradient of β' with the propagation distances. Within the same sample and identical experimental setup, any abnormal increase of the nonlinear guided waves and the relative nonlinearity parameters indicate the growth of the material nonlinearity and degradation. In the present study, the relative nonlinearity parameters are calculated by Eq. (5.10) to characterize the nonlinear guided wave features on the partially immersed plate. The growing trends of the nonlinear guided wave features with varying excitation magnitudes and propagation distance are investigated, respectively.

5.4. Experimental study

5.4.1. Experimental setup for actuating and sensing guided waves

Experiments were conducted on a 1.6 mm thick aluminum plate, which was fixed to the front of a metal tank with bolts. To investigate the effect of the liquid coupling on the nonlinear guided wave mixing, experimental measurements were collected on the external surface of the aluminum plate when the tank was empty and when

it was filled with water, respectively. Due to the isotropic features of the metal materials, the findings of this study could be also applicable to the isotropic plates made of other metal materials such as steel and alloy. Figure 5.1 shows a photo of the experimental setup. A computer-controlled signals generator (NI PIX-5412) was employed to generate the excitation signals. The waveforms of the excitation signals and the frequency selection are discussed in detail in Section 5.4.2. Then, the voltage of the input signals was magnified by a voltage amplifier (Ciprian HVA-800-A). After that, the amplified excitation signals were sent to the piezoceramic transducer (Ferroperm Pz27, 10 mm diameter and 0.5 mm thick) that was bonded to the outer surface of the test plate. The piezoceramic transducer could convert the electric signals to mechanical motions and generate guided waves on the test plate. The response signals on the plate surface were measured by a scanning laser vibrometer (Polytec PSV-400-M2-20) and then further processed using the software MATLAB. Each measurement was collected at 25.6 MHz and averaged by 1000 acquisitions. The signal-to-noise ratios were improved by applying a low-pass filter, of which the cut-off frequency was set to 1MHz.

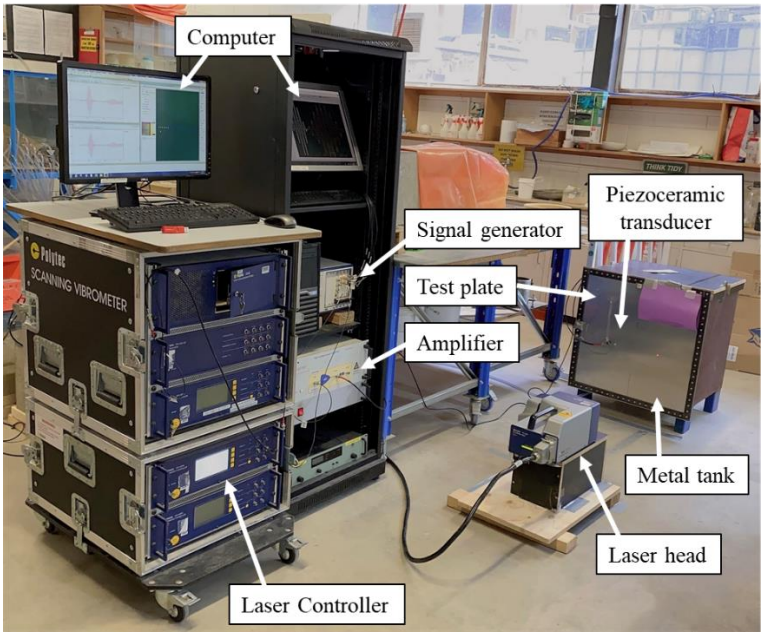

Figure 5.1. Experimental setup

5.4.2. Mode tuning and frequency selection

This section describes the selection of guided wave modes and excitation frequencies for the nonlinear guided wave mixing in partially immersed plates. To begin with, the dispersion features of guided waves were studied using DISPERSE. Based on the global matrix method, the dispersion curves were derived for the 1.6 mm thick aluminum plate surrounded by air (when the metallic tank was empty) and the same plate with one side exposed to water (when the metallic tank was filled with water), respectively [44]. The material properties of the plate and the water are shown in Table 5.1. The water layer was defined as a non-viscous semi-infinite acoustic medium. The air properties were not considered in modeling because the influence of the air on the guided wave propagation was very small. The air-coupled plate surfaces were assumed to be traction-free. The water-coupled plate surface was defined by the structural-liquid boundary conditions, which connected the normal stresses and displacements at the plate-water interface [44]. Through the out-of-plane motions, the guided waves in the liquid-coupled structures could continuously radiate wave energy into the surrounding liquid medium.

Table 5.1: Material properties for the aluminum plate and the water layer

	Density (kg/m^3)	Young's modulus (GPa)	Poisson's ratio	Longitudinal velocity (m/s)
Aluminum	2704	70.76	0.33	--
Water	1000	--	--	1500

Figure 5.2 presents the dispersion curves for the 1.6 mm thick aluminum plate without water and loaded with water on one side, respectively. The frequency range was selected to be below the cut-off frequency of higher-order guided wave modes. Therefore, only the fundamental guided wave modes could be excited by the piezoceramic transducer. When the tank is empty, the test plate is surrounded by air on both surfaces. There are only the fundamental symmetric (S_0) and antisymmetric (A_0) wave modes on the air-coupled metallic plate as shown in Figures 5.2(a)-5.2(c). Previous studies demonstrated that S_0 wave on air-coupled

plates satisfies approximate phase velocity matching and nonzero power flow conditions [19, 45]. Specifically, the phase velocity of S_0 mode decreases very slowly with frequency. When the phase velocity of S_0 mode at the excitation frequency matches that of S_0 mode at twice the excitation frequency with a relative deviation of less than 1%, the interaction of the primary S_0 wave at the excitation frequency with the material nonlinearity of a metallic plate can generate measurable second harmonic S_0 waves at twice the excitation frequency. In addition, the calculated relative nonlinearity parameters can grow linearly with the propagation distance and can be used to characterize the microstructural change of the material before the initiation of macro-scale damage [19, 45, 46].

In contrast, the phase velocity of the A_0 wave increases rapidly with frequency, making the phase velocity of the A_0 wave at the excitation frequency significantly different from that of A_0 wave at other frequencies. To date, there are very limited studies using A_0 wave to evaluate the microstructural changes of material in the early damage stage. Chillara and Lissenden [47] numerically demonstrated that the interaction of A_0 wave with the material nonlinearity of a metallic plate can only generate second harmonic S_0 waves, which propagate independently and separate from the primary A_0 wave. The generated second harmonic S_0 waves are so small that it is difficult to measure in practical applications. However, A_0 wave has been extensively employed to identify contact-type damage, such as open fatigue cracks [18], delamination [48], and the bonding effects of bolts [49]. The clapping behaviors between the surfaces as guided waves pass through can generate measurable nonlinear guided waves. Since the contact-type nonlinearity is much larger than the material nonlinearity, the evaluation of the contact-type defects does not require phase velocity matching and nonzero power flow conditions.

When the tank is filled with water, one side of the test plate is in contact with water, and the other side is exposed to air. Guided waves in the partially immersed plate include the leaky S_0 wave and the fundamental leaky antisymmetric (leaky A_0) wave as well as the quasi-Scholte wave as shown in Figures 5.2(d)-5.2(f). The leaky A_0 wave has high attenuation and is unable to propagate a long distance in the immersed plates, as shown in Figure 5.2(f). The quasi-Scholte wave has low

attenuation but the deformation in the plate is much smaller than that in the liquid [31, 50]. When the quasi-Scholte wave becomes non-dispersive at a high frequency, the wave motions in the plate structures are negligible and difficult to measure [51]. Therefore, both guided wave modes are not feasible to generate measurable and cumulative nonlinear guided waves that reflect the material nonlinearity.

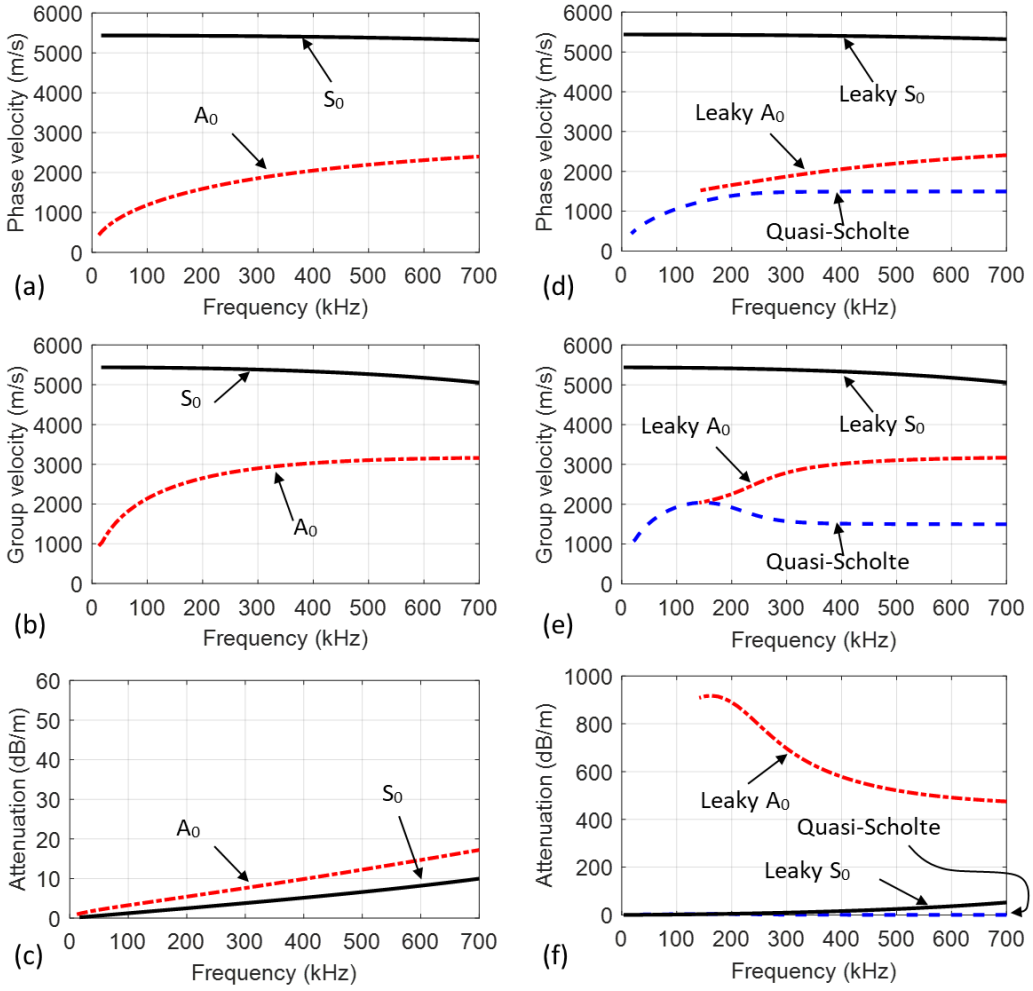

Figure 5.2. (a) Phase velocity, (b) group velocity, and (c) attenuation dispersion curves for the 1.6 mm thick aluminum plate without water; (d) phase velocity, (e) group velocity, and (f) attenuation dispersion curves for the 1.6 mm thick aluminum plate loaded with water on one side.

The leaky S_0 mode at low excitation frequencies is selected in this study for nonlinear guided wave mixing in the partially immersed plate. As shown by the

black solid lines in Figures 5.2(d)-5.2(f), the phase and group velocities of the leaky S_0 wave decrease very slowly with frequency, which is similar to those of the S_0 wave in the dry plate. In addition, the attenuation of the leaky S_0 wave is close to zero at the frequency range below 600 kHz. These features enable the leaky S_0 waves to have similar propagation characteristics across a relatively wide frequency range, which provides good flexibility for the selection of excitation frequencies for guided wave mixing.

For further investigation, mode shapes were extracted by DISPERSE for the S_0 mode and the leaky S_0 mode, respectively, as shown in Figure 5.3. The mode shape diagrams display the relative displacements of guided wave modes across the thickness of the structure. The red dashed lines and the blue solid lines represent the particle displacements in the in-plane direction (parallel to the wave propagation) and the out-of-plane direction (normal to the plate surface), respectively. The amplitudes are normalized by the maximum absolute magnitudes. Figures 5.3(a) and 5.3(b) show the mode shapes for the S_0 mode at 100 kHz and 500 kHz, respectively. Within the selected frequency range, the S_0 mode is dominated by the in-plane displacement that is uniformly distributed across the plate thickness. The out-of-plane displacement component is small at low frequency and gradually increases with frequency. For comparison, Figures 5.3(c) and 5.3(d) show the mode shapes for the leaky S_0 mode at 100 kHz and 500 kHz, respectively. Generally, the wave structure of leaky S_0 mode in the immersed plate is similar to that of S_0 mode in the plate without water. The leaky S_0 mode has predominately wave motions conserved in the plate structure, which ensures sufficient wave motions to interact with the material microstructures. The in-plane displacement between the plate and water is disconnected, while the out-of-plane displacement is continuous. Therefore, as the frequency increases, more wave energy can leak into the liquid medium through the out-of-plane wave motions. For these observations, the frequency range of interest was chosen to be below 600 kHz to ensure that the generated nonlinear guided waves have low attenuation and are measurable.

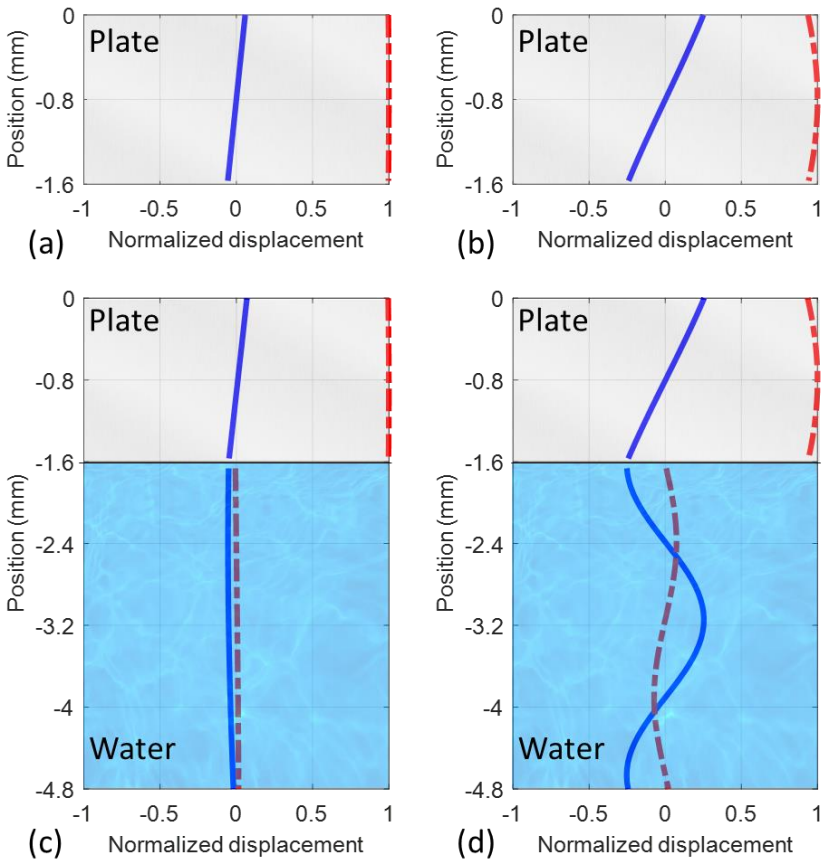

Figure 5.3. Mode shapes for S_0 mode in a 1.6 mm thick aluminum plate at (a) 100 kHz and (b) 500kHz and mode shapes for leaky S_0 mode for the plate loaded water on one side at (c) 100 kHz and (d) 500kHz. (the red dashed lines represent the in-plane displacements and the blue solid lines denote the out-of-plane displacements)

Preliminary tests were implemented with single-frequency excitation signals on the empty tank and the water-filled tank, respectively, to evaluate the excitability of the piezoceramic transducers. The preliminary tests aimed to select two excitation frequencies, at which the selected guided wave modes have comparable wave motions. The single-frequency excitation signals were 6-cycle narrow-band tone burst pulses modulated by Hanning window [15]. The excitation frequency swept from 90 kHz to 410 kHz in steps of 20 kHz. Figure 5.4(a) shows typical examples of the guided wave signals measured at 250 mm away from the excitation center. The excitation frequency was 230 kHz. The red dash-dot and black solid lines denote the signals obtained from the empty tank and water-filled tank, respectively. From the wave speed evaluation, the first wave packets between

45 μs and 80 μs were identified as the S_0 wave for the empty tank and the leaky S_0 wave for the water-filled tank, respectively. It should be noted that the scanning laser vibrometer measures the normal displacements on the plate surface [32]. Although S_0 and leaky S_0 waves are relatively small in the received signals, their actual wave motions in the plate should be strong because both wave modes have mostly in-plane motions as shown in Figure 5.3. Following the first wave packets, the second wave in the empty tank should be the A_0 wave, while the second wave in the water-filled tank is the quasi-Scholte wave. The latter travels much slower than the former, which is in good agreement with the theoretical predictions by the group velocity dispersion curves as shown in Figures 5.2(b) and 5.2(e).

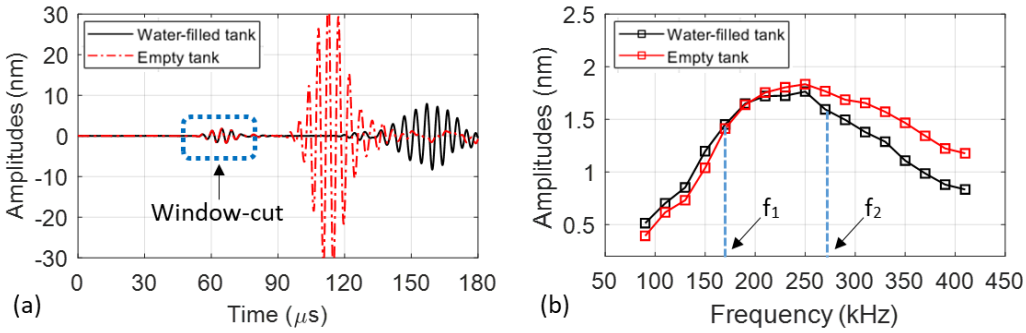

Figure 5.4. (a) Comparison of the time-domain signals experimentally collected from the empty tank and water-filled tank and (b) the peak amplitudes of the extracted signals across various frequencies.

For further signal processing, the first wave packets were extracted from the rest of the signals. Figure 5.4(b) shows the peak amplitudes of the first wave packet for different excitation frequencies. In general, the magnitudes of the signals measured from the empty tank and water-filled tank change with the excitation frequency, following a similar pattern. When the frequency increases from 90 kHz to 250 kHz, the amplitudes of the signals increase with frequency. For the frequency range over 250 kHz, the amplitudes of the signals decrease with frequency. The decreasing rates of the signals measured from the water-filled tank are much quicker than those obtained from the empty tank. From these observations, f_1 and

f_2 were selected to be 170 kHz and 270 kHz, respectively, for the following three reasons. Firstly, the difference between f_1 and f_2 was chosen to be 100 kHz, which enables good separation between the second harmonics and the combination harmonics. Secondly, the signals collected at both excitation frequencies had relatively high signal-to-noise ratios. Thirdly, the received signals show the normal displacement components on the plate surface. For the S_0 and leaky S_0 waves, the out-of-plane displacements increase with frequency as shown in Figure 5.3. Therefore, the signal amplitude at f_1 should be slightly lower than that at f_2 to ensure the actual wave motions at the two selected excitation frequencies have comparable magnitudes on the plate.

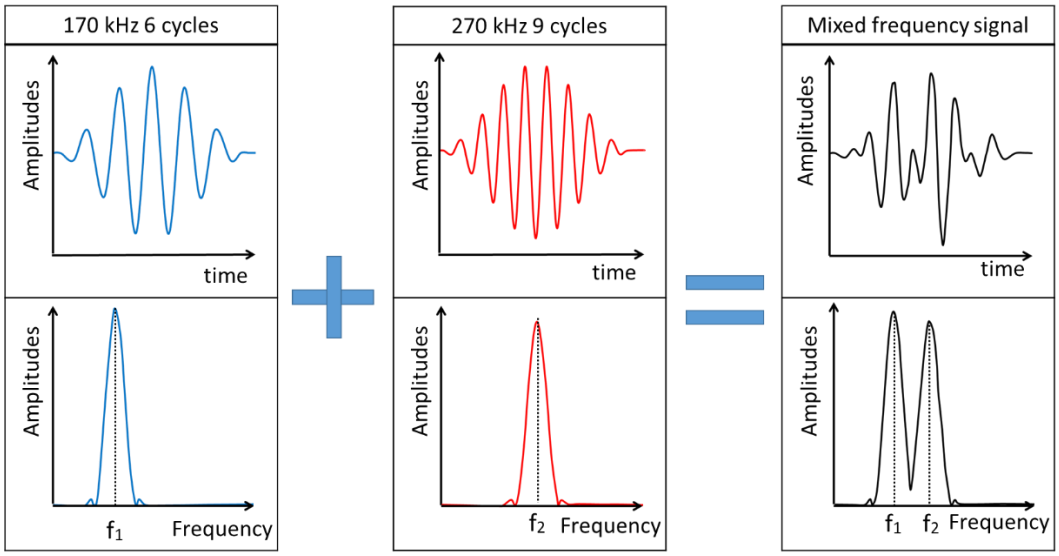

Figure 5.5. Merging two single-frequency tone burst signals to generate a mixed frequency signal.

Next, the mixed frequency excitation signals were generated by merging two single-frequency signals, which were a 6-cycle Hanning window-modulated tone burst at a central frequency of 170 kHz and a 9-cycle Hanning window-modulated tone burst at a central frequency of 270 kHz. The higher frequency signal had more cycles, which was to ensure that the two frequency components had similar duration in the time domain and comparable energy contents in the

frequency spectrums. A mix ratio of 1:1 (where 1:1 mixing means 1 part 170 kHz and 1 part 270 kHz) is promising to generate larger combination harmonics than other mix ratios [52]. Figure 5.5 shows the waveforms of the single-frequency and mixed frequency signals and their corresponding frequency spectrums.

5.4.3. Experimental results

5.4.3.1. Guided wave mixing in partially immersed metal plates

A demonstration of the guided wave mixing phenomenon was presented for the partially immersed plate. Firstly, experiments were carried out with the water-filled tank using the two single-frequency excitation signals as shown in Figure 5.5. The measurements were collected at a fixed location that was 250 mm away from the actuator center. The voltage of the input signals was increased to 160 V. Figures 5.6(a) and 5.6(b) show the time-domain signals for 170 kHz and 270 kHz, respectively. The first wave packets in the two figures are identified as the leaky S_0 waves that propagate faster than any other wave mode as shown by the group velocity dispersion curves in Figure 5.2(e). Secondly, experiments with the same settings were performed using the mixed frequency signal. The response signals measured at the same location are shown in Figure 5.6(c). It can be seen that the waveform of the first wave packet is similar to the input of the mixed frequency signal as shown in Figure 5.5. This is because leaky S_0 waves have similar phase and group velocities and low attenuation within the selected frequency range. The leaky S_0 waves at 170 kHz and 270 kHz can propagate together and the wave-mixing zone is maximized.

Following the first wave packet, there are other wave components in Figures 5.6(a)-5.6(c). Since leaky A_0 waves have high attenuation at the selected frequencies, the remaining wave components should be dominated by the low-attenuated quasi-Scholte waves. It can be seen that the waveform of the quasi-Scholte wave in Figure 5.6(c) is similar to that at 170 kHz as shown in Figure 5.6(a). This is because the deformation fraction in the immersed plate of the quasi-Scholte wave decreases rapidly with frequency [53]. As a result, when the structure is excited by the mixed frequency signal, the quasi-Scholte waves measured on the plate surface are dominated by the low-frequency components. The high-frequency

components of the quasi-Scholte wave are too weak to interact with the low-frequency components. Therefore, the quasi-Scholte wave can be filtered out for the study of nonlinear guided wave mixing.

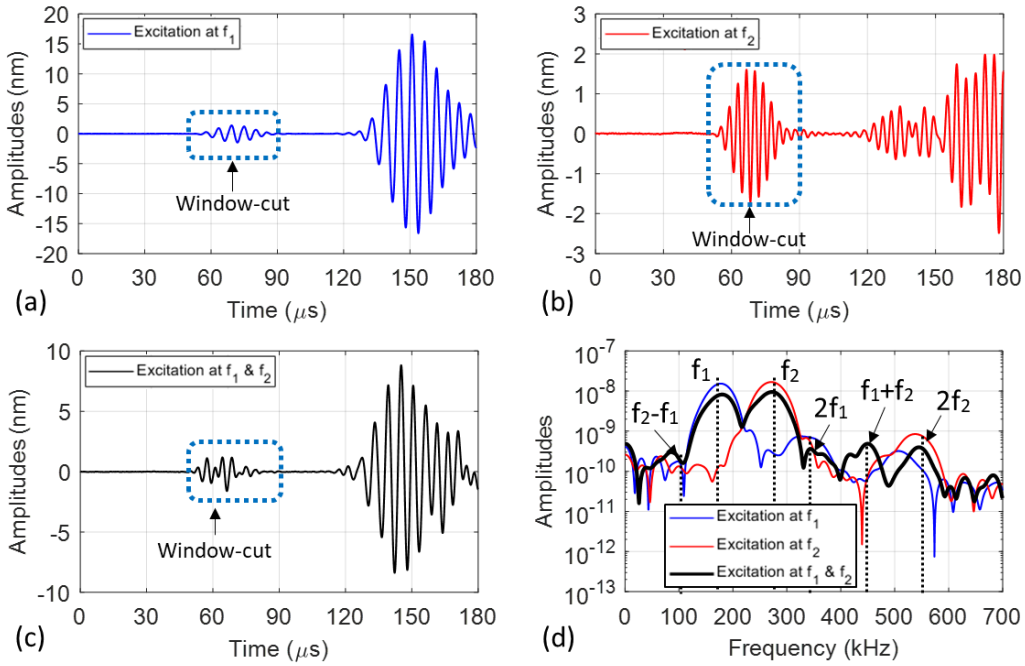

Figure 5.6. Experimental signals from the water-filled tank with the excitation (a) at f_1 = 170 kHz, (b) at f_2 = 270 kHz, (c) at mixed frequencies; and (d) the frequency spectrum of their corresponding window-cut data.

Then, the first wave packets were extracted from the rest of the signals and transferred into the frequency domain by fast Fourier transfer (FFT) as shown in Figure 5.6(d). When the one-side water-immersed plate is excited separately by the single-frequency signals, the 170 kHz and 270 kHz leaky S_0 waves can generate second harmonics, as manifested by the peaks at double the excitation frequencies ($2f_1 = 340\text{kHz}$ and $2f_2 = 540\text{kHz}$). For comparison, when the partially immersed plate is excited by the mixed frequency signal, the received signal has an additional peak at the sum frequency ($f_1 + f_2 = 440\text{kHz}$), as shown by the black solid line in Figure 5.6(d). The combination harmonics at the difference frequency ($f_1 - f_2 = 100\text{kHz}$) cannot be observed clearly for the mixed frequency excitation.

This is because the difference frequency is too close to the lower excitation frequency ($f_1 = 170\text{kHz}$) with only 70 kHz spacing. So, the difference harmonics can be overwhelmed by the side lobes [46, 54]. The same reason also applies to the second harmonics at ($2f_1 = 340\text{kHz}$) that are very close to the higher excitation frequency ($f_2 = 270\text{kHz}$). Nevertheless, the experimental results indicate that mixing leaky S_0 waves with two different frequencies can generate low-attenuated sum harmonics on the partially immersed plate.

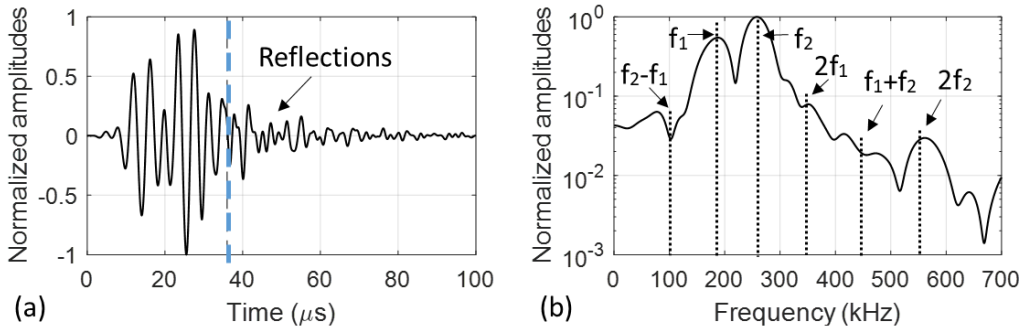

Figure 5.7. The actual excitation signals from the piezoceramic transducer (a) in the time domain, and (b) in the frequency domain.

Next, the nonlinearity due to the instrumentations was investigated. Figure 5.7(a) shows the actual signal from the piezoceramic transducer measured by the scanning laser vibrometer. Figure 5.7(b) presents the corresponding frequency spectrum. The amplitudes are normalized by the maximum absolute magnitudes. As shown in Figure 5.7(b), there are no apparent peaks at the sum frequency ($f_1 + f_2 = 440\text{kHz}$) and difference frequency ($f_1 - f_2 = 100\text{kHz}$) in the frequency spectrum of the actual signal from the piezoceramic transducer. Therefore, the sum harmonics observed in Figure 5.6(d) should be generated mainly by the interaction of the guided waves with the material nonlinearity. However, the actuation system can produce second harmonics as manifested by the peak at ($2f_2 = 540\text{kHz}$) in Figure 5.7(b).

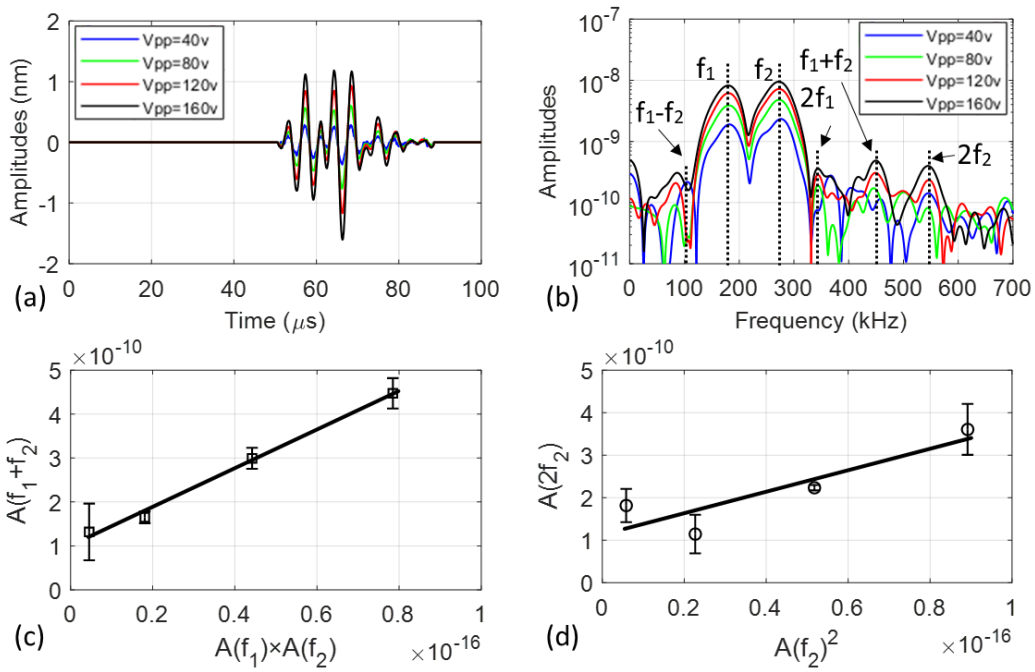

Figure 5.8. Experimental signals from the water-filled tank excited by mixed frequency signal (a) in the time domain, and (b) in the frequency domain; (c) the amplitudes of the sum harmonics versus the product of the primary wave amplitudes; and (d) the amplitudes of the second harmonics at $2f_2$ versus the square of the corresponding primary wave amplitudes at f_2.

After that, the nonlinear response of the guided wave mixing was further investigated by varying the excitation voltages. The voltage of the input signal was increased to 40V, 80V, 120V, and 160V, respectively. For each voltage, the response signals were measured five times at 250 mm away from the excitation center. Figures 5.8(a) and 5.8(b) show the experimentally measured signals in the time domain and the frequency domain, respectively. Figure 5.8(c) shows the amplitudes of the sum harmonics versus the product of the primary waves at the two excitation frequencies. Figure 5.8(d) shows the amplitudes of the second harmonics at $2f_2$ versus the square of the amplitudes of the corresponding primary waves at f_2. The black solid lines in Figures 5.8(c) and 5.8(d) represent the best-fit lines by linear regressions with the error bars denoting the standard deviations of five measurements. As discussed in Section 2, the amplitudes of the second

harmonics due to the material nonlinearity should increase linearly with the square of the amplitudes of the corresponding primary waves, while the amplitudes of the combination harmonics should grow linearly with the product of the primary waves at the two excitation frequencies. Overall, this analysis demonstrates that both the combination harmonics and the second harmonics could be generated due to the material nonlinearity of the specimen. However, the growing trends of the second harmonics in Figure 5.8(d) show relatively larger deviations from the best-fit line. This phenomenon indicates that the second harmonics are more susceptible to the nonlinearity generated by the instrumentations, which agrees well with Figure 5.7(b).

5.4.3.2. The effect of the surrounding liquid on the guided wave propagation

The section compares the phenomenon of guided wave mixing in the test plate with and without water. Guided wave signals were collected from the empty tank and the water-filled tank, respectively, under the same experimental conditions. Figure 5.9(a) presents the time-domain signals measured at 250 mm away from the excitation center. The red dash-dot and black solid lines denote the signals obtained from the empty tank and water-filled tank, respectively. The first wave packets are identified as the mixed frequency S_0 wave for the empty tank and the mixed frequency leaky S_0 wave for the water-filled tank, respectively. Both wave modes have similar amplitudes and waveforms in the time domain. However, an obvious difference can be observed in the frequency domain. Figure 5.9(b) shows the frequency spectrums of the window-cut signals extracted from Figure 5.9(a). The combination harmonics at the sum frequency can be observed in both the empty tank and the water-filled tank. The amplitudes of the primary waves at fundamental excitation frequencies (170 kHz and 270 kHz) are similar for the empty tank and water-filled tank. Over 270 kHz, the signal obtained from the empty tank has larger amplitudes than that obtained from the water-filled tank.

Further research investigated the growing trends of combination harmonics at the sum frequency with increasing excitation voltage and propagation distance, respectively. Figure 5.9(c) shows the amplitudes of the sum harmonics versus the product of the primary wave magnitudes at the fundamental frequencies. The

response signals were collected at 250 mm away from the excitation center and the voltage of the input signal was increased to 40V, 80V, 120V, and 160V. Five measurements were collected for each voltage on both the empty tank and the water-filled tank, respectively. It can be seen that the amplitudes of both the primary waves ($A_{f_1} \times A_{f_2}$) and the sum harmonics ($A_{f_1+f_2}$) on the empty tank are relatively larger than those on the water-filled tank. Also, when the primary waves ($A_{f_1} \times A_{f_2}$) increase, the sum harmonics ($A_{f_1+f_2}$) on the empty tank increase much faster than those on the water-filled tank.

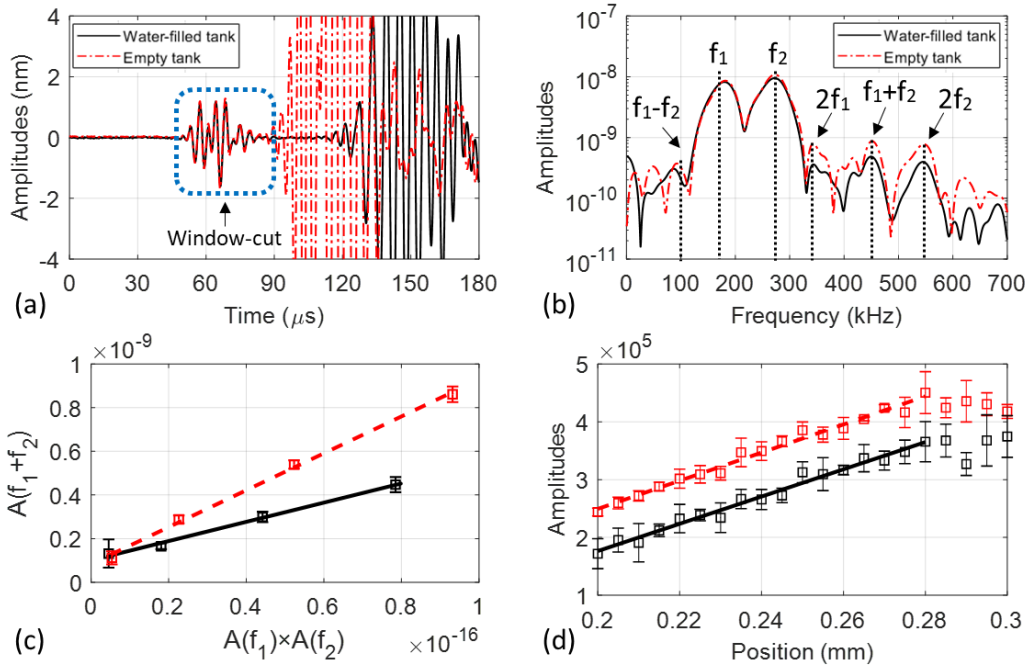

Figure 5.9. Comparison of experimental signals from the empty tank and water-filled tank excited by mixed frequency signal (a) in the time domain, and (b) in the frequency domain; (c) the amplitudes of the sum harmonics versus the product of the primary waves; and (d) the amplitudes of the nonlinearity parameters for the sum harmonics versus propagation distance.

To investigate the relationship between the combination harmonics at the sum frequency and the propagation distance, 21 measurement points were defined on the external surface of the test plate and equally spaced between 200 mm and

300 mm away from the excitation center. The voltage of the input signals was increased to 160 V. Five measurements using the same settings were performed on the empty tank and water-filled tank, respectively. Then, the relative nonlinearity parameters were calculated by Eq. (5.10) for the sum harmonics and plotted against the propagation distance as shown in Figure 5.9(d). For both the empty tank and the water-filled tank, the relative nonlinearity parameters grow linearly with the propagation distance from 200 mm to 270 mm. The cumulative propagation distances are limited to 270 mm, which may be caused by the small phase velocity difference between the primary waves and the sum harmonics. As shown in Figure 5.2, the phase velocities of S_0 wave in the dry plate and leaky S_0 wave in the partially immersed plate have similar values and decrease slowly with frequency. The phase velocities of the primary S_0 waves at 170 kHz and 270 kHz are 5430 m/s and 5422 m/s, respectively. They are very close to the phase velocity of the sum harmonic S_0 waves at 440 kHz, which is around 5397 m/s. The deviation is less than 1%. Previous studies have analytically and experimentally demonstrated that the cumulative propagation distances of second harmonic generation due to material nonlinearity decrease with the phase velocity difference between the primary S_0 waves and the second harmonic S_0 waves [19, 45]. In the present study, the cumulative propagation distances of sum harmonics determined by experimental measurements have a similar order of magnitudes to the theoretical predictions for the second harmonic generation by S_0 waves due to material nonlinearity [45]. Thus, it can be validated that the sum harmonics of the signals measured from 200 mm to 270 mm are generated due to the nonlinearity of the material.

In the linearly cumulative range, the growth rate of the relative nonlinearity parameters with the propagation distance does not show an apparent difference between the plate surrounded by air and the plate partially immersed in water. However, the absolute values of the relative nonlinearity parameters on the empty tank are much larger than those on the water-filled tank. Therefore, these results indicate that the cumulative generation of combination harmonics due to the material nonlinearity of partially immersed plates can be achieved with a mixed frequency leaky S_0 wave. Under the same experimental conditions, the amplitudes of the guided wave signals and the values of the relative nonlinearity parameters on

the partially immersed plate are different from their counterparts on the plate in gaseous environments.

5.5. Numerical study

5.5.1. Modeling material nonlinearity

Numerical simulations were carried out with ABAQUS to further investigate the sensitivity of the combination harmonics to the material nonlinearity of the partially immersed metallic plate. The numerical methods have the advantage of eliminating unwanted effects of the noises from the measurement system. The nonlinearity of the material was simulated by incorporating a VUMAT subroutine that introduced a constitutive model proposed by Murnaghan [55]. This section presents the constitutive equations. To begin with, $\mathbf{X}$ and $\mathbf{x}$ are defined as the coordinates in the reference and current configurations, respectively. The deformation gradient can be expressed as [56]

$$\mathbf{F} = \frac{\partial \mathbf{x}}{\partial \mathbf{X}} = \mathbf{I} + \mathbf{H} \tag{5.11}$$

where $\mathbf{I}$ is the identity tensor; $\mathbf{H} = \partial \mathbf{u} / \partial \mathbf{X}$ is the displacement gradient and $\mathbf{u} = \mathbf{x} - \mathbf{X}$ is the displacement vector. The Lagrangian strain tensor can be written as

$$\mathbf{E} = \frac{1}{2}\mathbf{F}^T\mathbf{F} = \frac{1}{2}\left[\mathbf{H} + \mathbf{H}^T + \mathbf{H}^T\mathbf{H}\right] \tag{5.12}$$

For a hyperelastic and homogeneous isotropic solid material, the strain energy function is [55]

$$\begin{aligned}\mathbf{W}(\mathbf{E}) = {} & \frac{1}{2}\lambda\left(\mathrm{tr}\left(\mathbf{E}\right)\right)^2 + \mu\,\mathrm{tr}\left(\mathbf{E}^2\right) + \frac{1}{3}\left(l + 2m\right)\left(\mathrm{tr}\left(\mathbf{E}\right)\right)^3 \\ & - m\,\mathrm{tr}\left(\mathbf{E}\right) \times \left(\left(\mathrm{tr}\left(\mathbf{E}\right)\right)^2 - \mathrm{tr}\left(\mathbf{E}^2\right)\right) + n\det\left(\mathbf{E}\right)\end{aligned} \tag{5.13}$$

where λ and μ are the lame constants; l, m, and n are Murnaghan constants that describe the second order material nonlinearity. Previous studies experimentally measured the Murnaghan constants from dog bone samples made

of aluminum [57]. The samples were subjected to repeated uniaxial tensile loads with different cycles. One sample was loaded to a total of 52800 cycles and failed. The rest samples were loaded to various cycles and referenced to the percent of fatigue level. Table 5.2 summarizes the material properties of aluminum with 0, 40%, and 80% fatigue levels [57].

Table 5.2. Lame constants and Murnaghan constants for aluminum [57]

Fatigue level (%)	ρ (kg m^{-3})	λ (GPa)	μ (GPa)	L (GPa)	M (GPa)	N (GPa)
0	2704	51.6	26.6	-252.2	-325.0	-351.2
40	2704	51.6	26.6	-266.8	-332.8	-358.3
80	2704	51.6	26.6	-271.2	-335.8	-359.8

The second Piola-Kirchhoff stress tensor can be obtained by

$$\mathbf{T}_{PK2} = \frac{\partial \mathbf{W}(\mathbf{E})}{\partial \mathbf{E}} \tag{5.14}$$

The Piola-Kirchhoff stresses are used to describe the reference configuration and correlated with the Cauchy stress tensor $\boldsymbol{\sigma}$ as

$$\mathbf{T}_{PK2} = \det(\mathbf{F})\mathbf{F}^{-1}\boldsymbol{\sigma}\left(\mathbf{F}^{-1}\right)^{T} \tag{5.15}$$

5.5.2. 3D FE model

ABAQUS/CAE was employed to build and mesh the 3D FE model as shown in Figure 5.10. The model consisted of a test plate that was 250 mm wide and 430 mm long and had the same thickness as the experimental specimen. The bottom surface of the test plate was exposed to water. The red quarter circle at the bottom left corner of the plate represented a quarter of the piezoceramic transducer, which was perfectly bonded to the top surface of the plate. Symmetric boundary conditions were defined for the left and bottom edges. Firstly, the numerical simulations were implemented by considering only the linear elastic material properties of the test plate and water as shown in Table 5.1. The linear finite element (FE) simulations consider the metallic plate as a linear elastic material. Then, nonlinear FE

simulations were carried out by incorporating the VUMAT subroutine that implemented the Murnaghan constitutive model. The material properties of the test plate were defined by the Murnaghan constitutive model and the material constants given in Table 5.2.

Eight-node 3D solid elements with reduced integration were used to mesh the test plate and the piezoceramic transducer. Eight-node 3D acoustic elements with reduced integration were used to model the water layer. The in-plane element size was approximately 0.5 × 0.5 mm^2 to ensure more than 20 elements exist per wavelength of the selected leaky S_0 wave at 270 kHz. The thickness direction of the plate has six layers of elements. The interaction between the test plate and water layer was simulated by applying the surface-based tie constraints on the plate-water interface, which allows the guided wave energy to transmit through the out-of-plane motions [58].

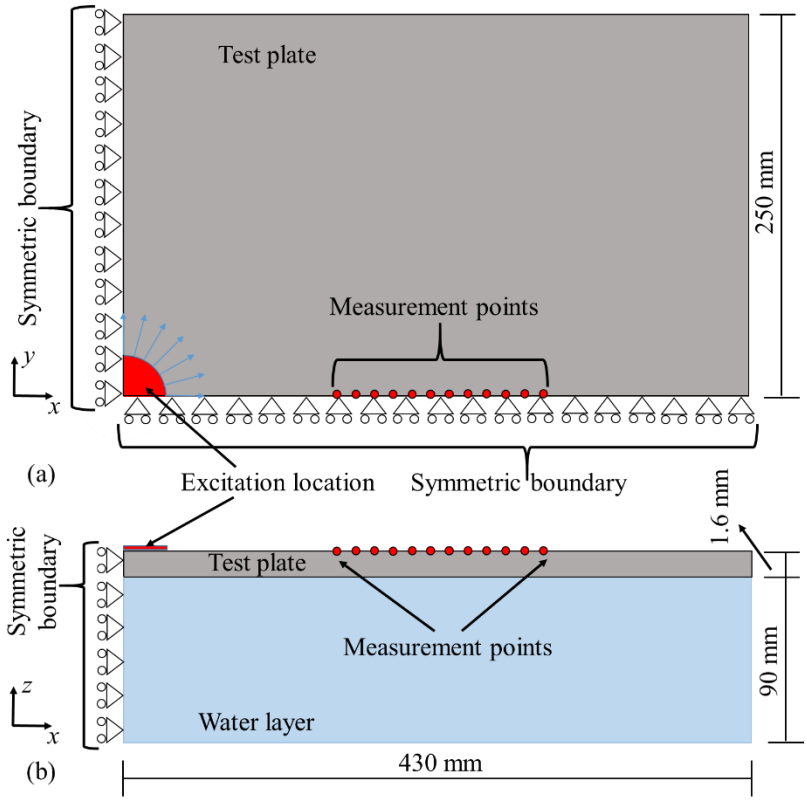

Figure 5.10. Schematic diagram of the 3D FE model (a) top view and (b) side view

Leaky S_0 waves were generated by applying nodal displacements to the circumference of the simulated piezoceramic transducer [18]. The displacements were assigned in the radial direction as shown in Figure 5.10(a). The excitation signals were the mixed frequency signals as shown in Figure 5.5. The magnitude of the displacement was 3 μm. The simulated guided wave signals were calculated by the central-difference integration through ABAQUS/Explicit. In all simulations, the increment time step was automatically controlled by ABAQUS. The maximum time increment step is less than the ratio of the minimum element size to the dilatational wave speed [43]. The accuracy of the nonlinear constitutive model was validated by comparing the results with the outcomes of the linear FE and experimental measurements.

5.5.3. Experimental validation

Figure 5.11(a) compares the experimental measurements and simulation results in the time domain. The time-domain signals, simulated by the nonlinear FE model incorporating the Murnaghan constants for the intact aluminum (zero fatigue in Table 2), are consistent with those simulated by the linear FE model. Both have a good agreement with the experimental signals. Next, the signals were windowed between 45 μs and 80 μs and transferred into the frequency domain as shown in Figure 5.11(b). The linear and nonlinear FE models well predict the primary guided wave components of the experimental signals at the fundamental excitation frequencies, as highlighted by the dotted lines at 170 kHz and 270 kHz in Figure 5.11(b). The linear FE signals have no nonlinear guided wave components at frequencies other than the excitation frequencies. But the nonlinear FE well predicts the location of the peaks for the combination harmonics at the sum frequency ($f_1 + f_2$) and the second harmonics at $2f_2$. The amplitudes of the simulated nonlinear guided waves are comparable to the experimentally measured data. Although there is a discrepancy between the experimental signals and simulated signals at other frequency components, the nonlinear FE simulation well predicts the generation of the combination harmonics due to the material nonlinearity.

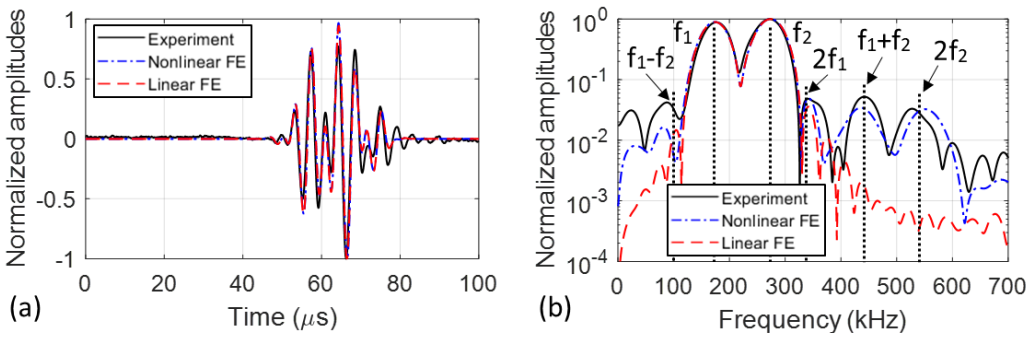

Figure 5.11: Experimental validations by comparing the experimental and simulated signals (a) in the time domain and (b) in the frequency domain

5.5.4. Parametric study

The 3D FE model validated by experiments was employed to further investigate the sensitivity of the nonlinear guided waves mixing to the material nonlinearity of the partially immersed metallic plate. Nonlinear FE simulations were implemented using the same 3D FE models, in which the material properties of the test plate were defined as aluminum at the three different fatigue levels as shown in Table 5.2, respectively. The out-of-plane displacements were collected at 11 measurement points that were equally distributed on the top surface of the test plate from 200 mm to 250 mm away from the excitation center. Then, the nonlinearity parameters were calculated using Eq. (5.10) for the combination harmonics at the sum frequency ($f_1 + f_2$) and the second harmonics at $2f_2$, respectively. To better observe the influence of material nonlinearity evolution, the relative nonlinearity parameters were normalized by their corresponding minimum value at zero fatigue level. Figures 5.12(a) and 5.12(b) show the normalized nonlinearity parameters for the combination harmonics and the second harmonics, respectively. Within the selected measurement range, the normalized nonlinearity parameters grow linearly with propagation distance. The growth rate (slope values of the best-fitted line) increases as the material suffers more fatigue damage.

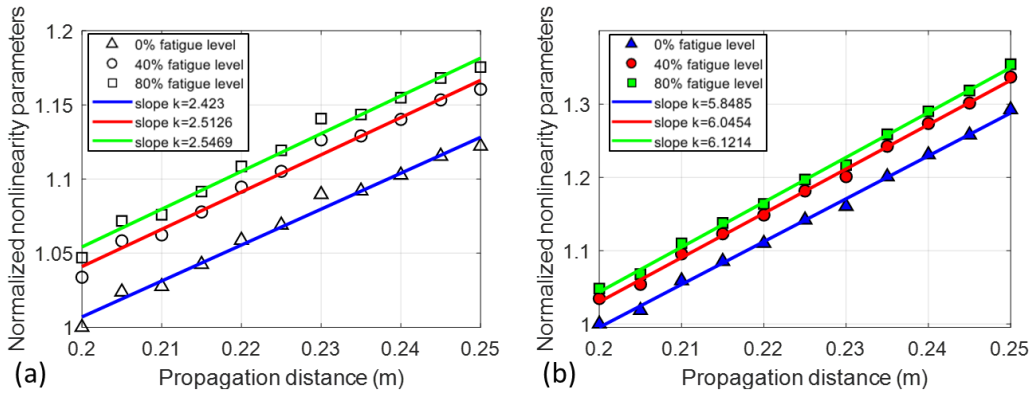

Figure 5.12 Normalized nonlinearity parameters for (a) the combination harmonics and (b) the second harmonics

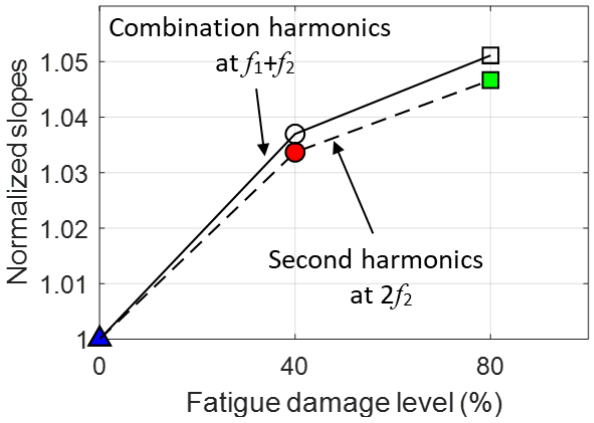

Figure 5.13 Normalized slopes of the best-fit lines versus the fatigue damage levels

Figure 5.13 shows the normalized slopes of the best-fit lines versus the fatigue damage levels for the second harmonics and the combination harmonics. The normalized slopes are calculated as the percentage of the slope values to their corresponding slope at zero fatigue level. The increase in slope indicates the progression of the material nonlinearity [19, 40]. It can be seen that both the combination harmonics and the second harmonics increase significantly, as the material suffers from progressive fatigue damage from 0 to 40%. Generally, the normalized slopes of the combination harmonics increase quicker than the second harmonics, which indicates that the combination harmonics have a better sensitivity to early fatigue damage.

5.6. Conclusion

This paper presents experimental and numerical investigations on the nonlinear guided waves mixing in the partially immersed plates. The main contributions are summarized as follows:

(1). According to the dispersion curves, leaky S_0 waves at low excitation frequencies have low attenuation and low dispersion effects, which provide good flexibility for the selection of excitation frequencies for guided wave mixing.

(2). Experiments have been conducted on an aluminum plate loaded with water on one side using the single-frequency excitation and mixed frequency excitation, respectively. Leaky S_0 waves with two different frequencies can generate combination harmonics at the sum of the excitation frequencies that cannot be achieved by single-frequency excitations (see Figure 5.6).

(3). The combination harmonics at sum frequency ($A_{f_1+f_2}$) grow linearly with the product of the primary guided waves at the fundamental excitation frequencies ($A_{f_1} \times A_{f_2}$) and are less affected by the nonlinearity due to instrumentations (see Figures 5.7 and 5.8).

(4). Under the same experimental conditions, the liquid-structure coupling of the partially immersed plate makes the amplitudes of the guided wave signals and the relative nonlinearity parameters different from those of the test plate without liquid coupling (see Figure 5.9).

(5). Numerical studies have been carried out with the material nonlinearity of the test plate simulated by the Murnaghan constitutive model. The numerical results reveal that both the second harmonics and the combination harmonics are sensitive to the material nonlinearity of the partially immersed plate (see Figures 5.12 and 5.13).

In conclusion, the current study has demonstrated that nonlinear guided wave mixing has the potential to evaluate the material nonlinearity of metallic plates with one side exposed to water. This new possibility can be significant considering the high rewards for earlier detection of the damage to maintain the structural integrity of high-valued infrastructures. To maximize the wave mixing zone, the selected

guided waves propagate together in the same direction. Future studies are required to explore the feasibility of non-collinear guided wave mixing, where the selected guided waves propagate in different directions and meet in a localized mixing zone. The non-collinear guided wave mixing has the potential to identify the area of localized material degradation but the generation and measurement of the nonlinear waves are more challenging because the nonlinear wave amplitudes can be affected by the reduced wave mixing zone. In addition, more experimental studies need to be carried out to investigate the correlation between the nonlinear guided wave signals and the degree of damage.

5.7. Acknowledgment

This work was funded by the Australia Research Council (ARC) under grant numbers DP200102300 and DP210103307. The supports are greatly appreciated.

5.8. Reference

[1] R. Liu, S. Li, G. Zhang, W. Jin, Depth detection of void defect in sandwich-structured immersed tunnel using elastic wave and decision tree, Construction and Building Materials, 305 (2021) 124756.

[2] R. Ignatowicz, E. Hotala, Failure of cylindrical steel storage tank due to foundation settlements, Engineering Failure Analysis, 115 (2020) 104628.

[3] N. Balekelayi, S. Tesfamariam, Statistical inference of sewer pipe deterioration using Bayesian geoadditive regression model, Journal of Infrastructure Systems, 25 (2019) 04019021.

[4] A. Heifetz, D. Shribak, X. Huang, B. Wang, J. Saniie, J. Young, S. Bakhtiari, R.B. Vilim, Transmission of images with ultrasonic elastic shear waves on a metallic pipe using amplitude shift keying protocol, IEEE Transactions on Ultrasonics, Ferroelectrics, and Frequency Control, 67 (2020) 1192-1200.

[5] M. Abbas, M. Shafiee, An overview of maintenance management strategies for corroded steel structures in extreme marine environments, Marine Structures, 71 (2020) 102718.

[6] M. Hong, Z. Su, Q. Wang, L. Cheng, X. Qing, Modeling nonlinearities of ultrasonic waves for fatigue damage characterization: Theory, simulation, and experimental validation, Ultrasonics, 54 (2014) 770-778.

[7] M. Jimenez-Martinez, Fatigue of offshore structures: A review of statistical fatigue damage assessment for stochastic loadings, International Journal of Fatigue, 132 (2020) 105327.

[8] R.C. Sriramadasu, S. Banerjee, Y. Lu, Sensitivity of longitudinal guided wave modes to pitting corrosion of rebars embedded in reinforced concrete, Construction and Building Materials, 239 (2020) 117855.

[9] Y. Zhang, Y. Sidibé, G. Maze, F. Leon, F. Druaux, D. Lefebvre, Detection of damages in underwater metal plate using acoustic inverse scattering and image processing methods, Applied Acoustics, 103 (2016) 110-121.

[10] A.E. Takiy, C. Kitano, R.T. Higuti, S.C.G. Granja, V.T. Prado, L. Elvira, O. Martínez-Graullera, Ultrasound imaging of immersed plates using high-order Lamb modes at their low attenuation frequency bands, Mechanical Systems and Signal Processing, 96 (2017) 321-332.

[11] S. Sharma, A. Mukherjee, Damage detection in submerged plates using ultrasonic guided waves, Sadhana, 39 (2014) 1009-1034.

[12] S. Sharma, A. Mukherjee, Ultrasonic guided waves for monitoring corrosion in submerged plates, Structural Control and Health Monitoring, 22 (2015) 19-35.

[13] X. Hu, C.-T. Ng, A. Kotousov, Scattering characteristics of quasi-Scholte waves at blind holes in metallic plates with one side exposed to water, NDT & E International, 117 (2021) 102379.

[14] V.K. Chillara, C.J. Lissenden, Review of nonlinear ultrasonic guided wave nondestructive evaluation: theory, numerics, and experiments, Optical Engineering, 55 (2015) 011002.

[15] C.J. Lissenden, Nonlinear ultrasonic guided waves—Principles for nondestructive evaluation, Journal of Applied Physics, 129 (2021) 021101.

[16] A. Ruiz, N. Ortiz, A. Medina, J.-Y. Kim, L. Jacobs, Application of ultrasonic methods for early detection of thermal damage in 2205 duplex stainless steel, NDT & E International, 54 (2013) 19-26.

[17] K.H. Matlack, H.A. Bradley, S. Thiele, J.-Y. Kim, J.J. Wall, H.J. Jung, J. Qu, L.J. Jacobs, Nonlinear ultrasonic characterization of precipitation in 17-4PH stainless steel, NDT & E International, 71 (2015) 8-15.

[18] Y. Yang, C.-T. Ng, A. Kotousov, H. Sohn, H.J. Lim, Second harmonic generation at fatigue cracks by low-frequency Lamb waves: Experimental and numerical studies, Mechanical Systems and Signal Processing, 99 (2018) 760-773.

[19] W. Zhu, Y. Xiang, C.-j. Liu, M. Deng, C. Ma, F.-z. Xuan, Fatigue damage evaluation using nonlinear Lamb Waves with Quasi phase-velocity matching at low frequency, Materials, 11 (2018) 1920.

[20] K. Dziedziech, L. Pieczonka, P. Kijanka, W.J. Staszewski, Enhanced nonlinear crack-wave interactions for structural damage detection based on guided ultrasonic waves, Structural Control and Health Monitoring, 23 (2016) 1108-1120.

[21] M. Deng, G. Gao, Y. Xiang, M. Li, Assessment of accumulated damage in circular tubes using nonlinear circumferential guided wave approach: a feasibility study, Ultrasonics, 75 (2017) 209-215.

[22] M. Hasanian, C.J. Lissenden, Second order harmonic guided wave mutual interactions in plate: Vector analysis, numerical simulation, and experimental results, Journal of Applied Physics, 122 (2017) 084901.

[23] M. Hasanian, C.J. Lissenden, Second order ultrasonic guided wave mutual interactions in plate: Arbitrary angles, internal resonance, and finite interaction region, Journal of Applied Physics, 124 (2018) 164904.

[24] J. Jiao, X. Meng, C. He, B. Wu, Nonlinear Lamb wave-mixing technique for micro-crack detection in plates, NDT & E International, 85 (2017) 63-71.

[25] A.K. Metya, S. Tarafder, K. Balasubramaniam, Nonlinear Lamb wave mixing for assessing localized deformation during creep, NDT & E International, 98 (2018) 89-94.

[26] S. Shan, M. Hasanian, H. Cho, C.J. Lissenden, L. Cheng, New nonlinear ultrasonic method for material characterization: Codirectional shear horizontal guided wave mixing in plate, Ultrasonics, 96 (2019) 64-74.

[27] H. Cho, M. Hasanian, S. Shan, C.J. Lissenden, Nonlinear guided wave technique for localized damage detection in plates with surface-bonded sensors to receive Lamb waves generated by shear-horizontal wave mixing, NDT & E International, 102 (2019) 35-46.

[28] W. Li, Y. Xu, N. Hu, M. Deng, Impact damage detection in composites using a guided wave mixing technique, Measurement Science and Technology, 31 (2019) 014001.

[29] L. Guan, M. Zou, X. Wan, Y. Li, Nonlinear Lamb wave micro-crack direction identification in plates with mixed-frequency technique, Applied Sciences, 10 (2020) 2135.

[30] E. Pistone, K. Li, P. Rizzo, Noncontact monitoring of immersed plates by means of laser-induced ultrasounds, Structural Health Monitoring, 12 (2013) 549-565.

[31] S. Tietze, G. Lindner, Visualization of the interaction of guided acoustic waves with water by light refractive vibrometry, Ultrasonics, 99 (2019) 105955.

[32] L. Yu, Z. Tian, Case study of guided wave propagation in a one-side water-immersed steel plate, Case Studies in Nondestructive Testing and Evaluation, 3 (2015) 1-8.

[33] D. Inoue, T. Hayashi, Transient analysis of leaky Lamb waves with a semi-analytical finite element method, Ultrasonics, 62 (2015) 80-88.

[34] X. Niu, L. Zhu, Z. Yu, B. Xing, Effect of temperature on nonlinearity of ultrasonic waves in metallic solids, 2019 Far East NDT New Technology & Application Forum (FENDT), 2019, pp. 197-201.

[35] S. Choi, P. Lee, K.-Y. Jhang, A pulse inversion-based nonlinear ultrasonic technique using a single-cycle longitudinal wave for evaluating localized material degradation in plates, International Journal of Precision Engineering and Manufacturing, 20 (2019) 549-558.

[36] C. Bermes, J.-Y. Kim, J. Qu, L.J. Jacobs, Nonlinear Lamb waves for the detection of material nonlinearity, Mechanical Systems and Signal Processing, 22 (2008) 638-646.

[37] G. Shui, J.-Y. Kim, J. Qu, Y.-S. Wang, L.J. Jacobs, A new technique for measuring the acoustic nonlinearity of materials using Rayleigh waves, NDT & E International, 41 (2008) 326-329.

[38] J.M. Hughes, A. Kotousov, C.-T. Ng, Generation of higher harmonics with the fundamental edge wave mode, Applied Physics Letters, 116 (2020) 101904.

[39] J. Park, J. Choi, J. Lee, A Feasibility study for a nonlinear guided Wave mixing technique, Applied Sciences, 11 (2021) 6569.

[40] W. Li, M. Deng, N. Hu, Y. Xiang, Theoretical analysis and experimental observation of frequency mixing response of ultrasonic Lamb waves, Journal of applied physics, 124 (2018) 044901.

[41] X. Hu, C.-T. Ng, A. Kotousov, Early damage detection of metallic plates with one side exposed to water using the second harmonic generation of ultrasonic guided waves, Thin-Walled Structures, 176 (2022) 109284.

[42] Y. Yang, C.-T. Ng, A. Kotousov, Second-order harmonic generation of Lamb wave in prestressed plates, Journal of Sound and Vibration, 460 (2019) 114903.

[43] C. Yeung, C.T. Ng, Nonlinear guided wave mixing in pipes for detection of material nonlinearity, Journal of Sound and Vibration, 485 (2020) 115541.

[44] B. Pavlakovic, M. Lowe, Disperse user manual: a system for generating dispersion curves, Copyright B Pavlakovic, M Lowe, (2003).

[45] X. Wan, P. Tse, G. Xu, T. Tao, Q. Zhang, Analytical and numerical studies of approximate phase velocity matching based nonlinear S0 mode Lamb waves for the detection of evenly distributed microstructural changes, Smart Materials and Structures, 25 (2016) 045023.

[46] H. Zhu, C.T. Ng, A. Kotousov, Low-frequency Lamb wave mixing for fatigue damage evaluation using phase-reversal approach, Ultrasonics, 124 (2022) 106768.

[47] V.K. Chillara, C.J. Lissenden, Nonlinear guided waves in plates: a numerical perspective, Ultrasonics, 54 (2014) 1553-1558.

[48] R. Soleimanpour, C.-T. Ng, Locating delaminations in laminated composite beams using nonlinear guided waves, Engineering Structures, 131 (2017) 207-219.

[49] J.C. Pineda Allen, C.T. Ng, Nonlinear Guided-wave mixing for condition monitoring of bolted joints, Sensors, 21 (2021) 5093.

[50] X. Hu, C.-T. Ng, A. Kotousov, Ultrasonic guided wave field modeling in a one-side water-immersed steel plate, Lecture Notes in Civil Engineering, 2021, pp. 1131-1140.

[51] X. Hu, C.-T. Ng, A. Kotousov, Numerical and experimental investigations on mode conversion of guided waves in partially immersed plates, Measurement, (2022) 110750.

[52] J.M. Hughes, A. Kotousov, C.-T. Ng, Wave mixing with the fundamental mode of edge waves for evaluation of material nonlinearities, Journal of Sound and Vibration, 527 (2022) 116855.

[53] X. Hu, C.-T. Ng, A. Kotousov, Damage detection of partially immersed plates using guided waves, Recent Advances in Structural Health Monitoring Research in Australia, Nova Science Publishers Inc., 2021.

[54] Z. Sun, A. Sun, B.-F. Ju, Deconvolution imaging of weak reflective pipe defects using guided-wave signals captured by a scanning receiver, Review of Scientific Instruments, 88 (2017) 024904.

[55] F. Murnaghan, Finite deformation of an elastic solid, in: Amer. Math. Soc, 1952, pp. 577-579.

[56] M. Mohabuth, A. Kotousov, C.-T. Ng, Effect of uniaxial stress on the propagation of higher-order Lamb wave modes, International Journal of Non-Linear Mechanics, 86 (2016) 104-111.

[57] D.M. Stobbe, Acoustoelasticity in 7075-T651 aluminum and dependence of third order elastic constants on fatigue damage, Georgia Institute of Technology, 2005.

[58] Abaqus, Abaqus 6.13 Analysis User's Guide, Dassault Systems Simulia Corp, Providence, RI, (2013).

Chapter 6. Conclusions and remarks

6.1. Summary of contributions

This thesis has presented a comprehensive study on the ultrasonic guided waves in thin-walled structures immersed in liquid on one side. The multimodal and dispersive features of guided waves have been analyzed and the influence of the surrounding liquid medium on the guided wave propagation characteristics has been demonstrated both numerically and experimentally. The quasi-Scholte wave and the fundamental leaky symmetric Lamb (leaky S_0) wave have been intensively studied for characterizing corrosion pits and microstructural evolution, respectively. Both linear and nonlinear guided wave features have been discussed. The findings complement the current knowledge about guided waves in submerged structures and provide support for safety inspections of high-valued and critical infrastructures, such as liquid storage tanks, vessels and pipelines, and submarine hulls.

Chapter 2 (Paper 1) has investigated the interaction of guided waves with corrosion pits in a steel plate loaded with water on one side. Among many other guided wave modes, the quasi-Scholte mode has been selected to characterize the dimensions of circular blind holes that are the simplest representations of progressive corrosion pits. The results have indicated that the quasi-Scholte mode has a high sensitivity to the physical conditions of the plate-water interface and is promising for evaluating corrosion damage in submerged structures.

In the literature, the quasi-Scholte wave was rarely used for damage detection. This chapter has highlighted that applying the quasi-Scholte wave for detecting damage in submerged structures is limited to the low frequency range, at which the quasi-Scholte wave is dispersive. A case study has been presented for using the quasi-Scholte wave at 100 kHz to characterize the blind holes in a 2 mm thick steel plate with one side immersed in water. The advantages of the quasi-Scholte wave at low frequencies have been demonstrated, which include easy excitation, low attenuation, strong signal-to-noise ratios, and shorter wavelength compared to other guided wave modes (higher sensitivity to smaller defects). However, the quasi-Scholte mode becomes nondispersive at a high frequency and

has most of its wave motions conserved in the liquid medium. The scattered waves caused by the damage can be hardly measured on the plate surface.

Chapter 3 (Paper 2) has further investigated and compared the behaviors of guided waves in a dry plate surrounded by air and the plate with one side immersed in water. The foregoing studies demonstrated that mode conversion occurs when guided waves propagate from the dry plate to the immersed plate. However, the variation with the excitation frequency of the mode conversion phenomenon has not been discussed before. In this chapter, the fundamental anti-symmetric Lamb wave (A_0) is excited on the dry plate section and travels to the water-immersed plate section, where the generated A_0 wave is mode converted to the quasi-Scholte wave. The frequency dependence of the mode conversion from A_0 wave to QS wave has been studied numerically and experimentally. It has been discovered that the guided wave energy can shift in the frequency domain when the phase velocity of the incident A_0 wave is larger than the sound speed of the surrounding liquid medium. Due to the dispersive features of guided waves, the change in frequency components can make the guided wave propagation properties different. Therefore, the findings of this study are important for practical applications (e.g. using guided waves for damage detection of partially immersed structures and assessing liquid properties and levels).

Chapters 2 and 3 have also indicated that the defects (e.g. corrosion pits) on partially immersed plates can be evaluated by sending A_0 wave on the dry section of the plate and measuring the quasi-Scholte wave on the immersed section. This method is very promising for long-range inspection because the quasi-Scholte wave has very low attenuation and does not radiate energy in the liquid. However, future study is required to develop an effective damage detection algorithm for the partially immersed structures to consider the change of wave behaviors due to the mode conversion phenomenon and the presence of liquid.

The targeted defects in the first two papers (Chapters 2 and 3) are thickness thinning in local areas and have a size of around a few millimeters. These macroscopic defects can change the propagation speeds and amplitudes of the transmitted guided wave signals, of which the wavelength is comparable to the dimension of the defects. Recent studies on guided wave applications have focused

on nonlinear guided wave features which provide the potential to identify and track the evolution of damage in the microscale that precedes macroscopic defects. Although nonlinear guided wave features have better sensitivity to microstructural defects, their generation and measurements are very challenging because the microscopic defects in the material are quite small. In the literature, several conditions were proposed for the structures surrounded by air to ensure that the nonlinear guided waves generated due to the material nonlinearity are cumulative and measurable. However, these conditions have not been validated for the structures submerged in liquid.

Chapter 4 (Paper 3) has explored the feasibility of the second harmonics generation by guided waves in metallic plates with one side exposed to water. The dispersive behaviors of multiple guided wave modes have been analyzed and three criteria have been proposed in regard to selecting appropriate guided wave modes and excitation frequencies. Firstly, the selected guided wave modes at the excitation frequency (primary waves) should have low attenuation and have most wave motions conserved in the submerged structures. Secondly, there should be nonzero power flux between the primary waves and the corresponding second harmonics. Thirdly, the phase velocity deviation between the primary waves and second harmonics should be less than 1%. These criteria can be also applied to different structures exposed to various liquids. Then, a case study has been presented using experimental signals with an excitation frequency of 170 kHz. The results have indicated that cumulative generation of second harmonics can be achieved by leaky S_0 wave. Next, a three-dimensional (3D) finite element (FE) model has been developed to simulate the nonlinear guided wave generation. The material nonlinearity of the immersed plate has been simulated by a VUMAT subroutine that incorporates Murnaghan's strain energy function. The numerical simulations have been validated through experimental measurements. After that, a series of parametric studies have been carried out and the results have shown that the second harmonics are sensitive to the early-stage damage in plates with one side immersed in water. However, the shortcoming of the second harmonic approach is that the instrumentations for sensing and actuating signals can also produce higher harmonics at the integer multiples of the excitation signals. It is very difficult to

extract the second harmonics due to the material nonlinearity from the instrument nonlinearity.

To cope with this limitation, Chapter 5 (Paper 4) has numerically and experimentally investigated the nonlinear guided wave mixing in an aluminum plate loaded with water on one side. Leaky S_0 waves are excited at two different frequencies on the wall of a metal tank filled with water. The results have shown that the nonlinear interaction between leaky S_0 waves at two different frequencies can produce cumulative combination harmonics at the sum frequency. Compared to the second harmonics studied in Chapter 4, the combination harmonics are less affected by the higher harmonics produced by the instrumentations, such as amplifiers and transducers. In addition, mixing guided waves with different frequencies provides more flexibility for the selection of guided wave modes and excitation frequencies. Finally, Chapter 5 has also presented parametric studies using the experimentally validated nonlinear FE model. The combination harmonics have shown a better sensitivity to the early stage of fatigue damage than the second harmonics.

6.2. Future work and recommendations

The current research only considers the fundamental guided wave modes at low excitation frequencies for the metallic plates partially immersed in water (non-viscous liquid). However, the current research has built a foundation for the development of guided wave-based techniques for safety inspection of submerged plates or thin-walled structures, based on the excellent ability of guided waves to travel at fast speed over long distances and the high sensitivity to the evolution of microscopic defects. Below are the possible research directions for future studies.

1. <u>The propagation characteristics of guided waves in plates immersed in viscous liquids (e.g. honey, oil, and gas).</u> The guided wave energy can leak into viscous liquids through both shear and longitudinal wave motions. This is different from the structures immersed in non-viscous liquids. Shear waves do not exist in non-viscous liquids because shear forces cannot be

sustained. Therefore guided waves in the plates immersed in viscous liquids can be significantly different from that in the non-viscous liquids.

2. The propagation characteristics of guided waves in submerged structures with different geometries (e.g. curved plates and T-section joints) and various materials (e.g. plastics and composites). Guided waves behave differently on different structures and materials. This future work is very important because real-world structures are more complex.
3. The feasibility of using guided waves to characterize multiple corrosion pits with irregular shapes. The damage in real-world structures can vary significantly in size, shape, and locations. Therefore, the effect of damage with increasing numbers and dimensions should be considered.
4. The acoustoelastic effect of submerged plates due to the hydrostatic pressure. Submerged structures containing liquids are usually subjected to hydrostatic pressure with varying aplitudes that can potentially induce and incrase microstructural defects. The acoustoelastic effect can change the propagation properties of guided waves and the generation of nonlinear guided wave features.
5. The interaction between guided waves and stress corrosion cracking. Stress corrosion cracking is one of the major concerns for the immersed metallic plate structures that are subjected to time-dependent loads with varying amplitudes. The present study only demonstrated that the micro cracks in the early stage of damage can generate measurable and low-attenuation second harmonics. The effect of the size, shape, and location of stress corrosion cracking in macroscale on the guided wave propagation can be future work.
6. The development of damage detection tools using guided waves and machine learning approaches. Current algorithms cannot be applied to structures with one side partly immersed in water as mentioned in Chapter 3 (Paper 2). A data-derived approach such as machine learning can help consider the change of wave behaviors due to the mode conversion phenomenon and the variation of liquid levels.